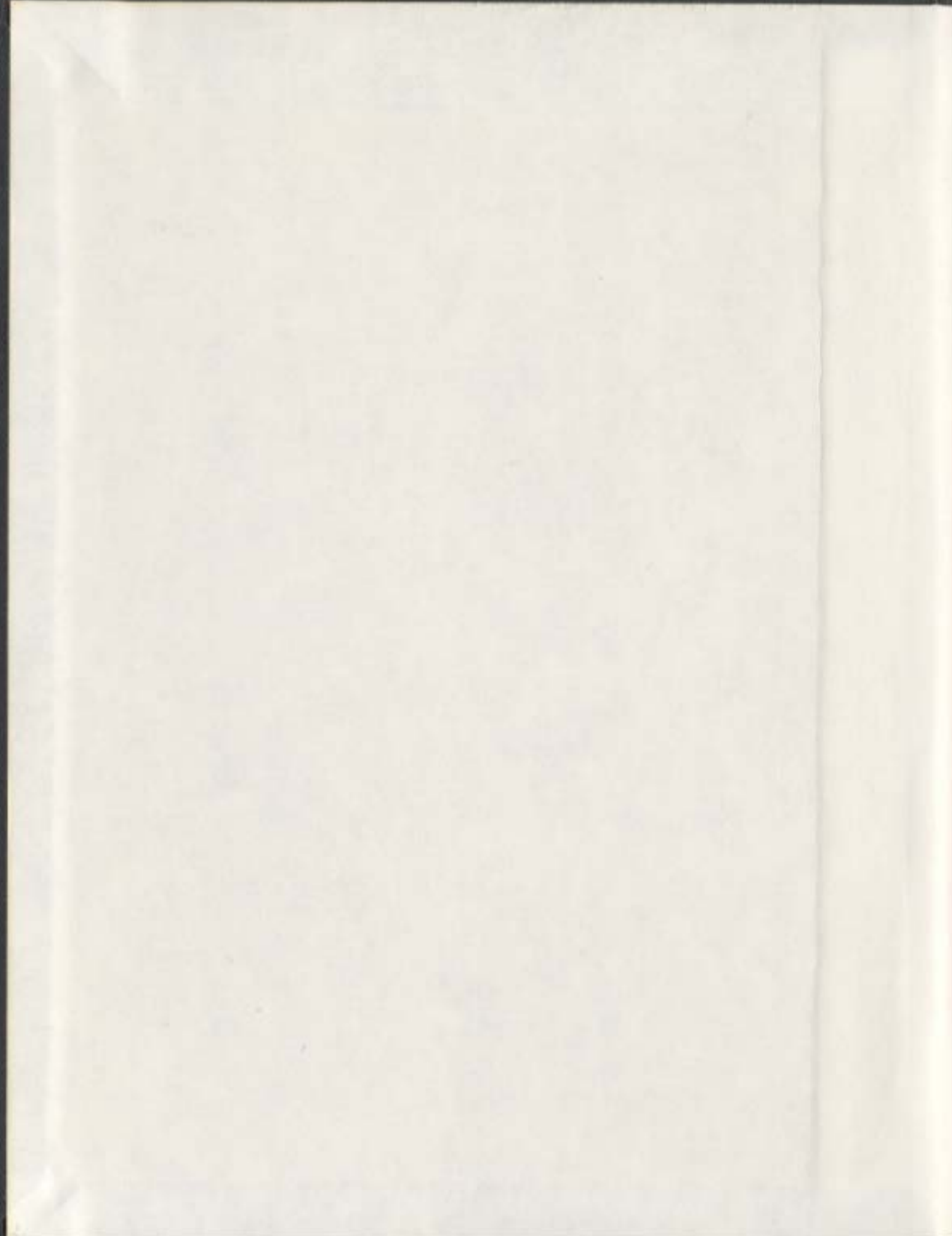


FINGERING INSTABILITIES IN NEWTONIAN AND
NON-NEWTONIAN FLUIDS

KRISTI E. KENNEDY



Fingering Instabilities in Newtonian and non-Newtonian Fluids

by

© Kristi E. Kennedy
B.Sc.H. (Memorial University, St. John's, Canada) 1999

A thesis submitted to the
School of Graduate Studies
in partial fulfillment of the
requirements for the degree of
Doctor of Philosophy.

Department of Physics and Physical Oceanography
Memorial University of Newfoundland

March 12, 2007

ST. JOHN'S

NEWFOUNDLAND



Library and
Archives Canada

Bibliothèque et
Archives Canada

Published Heritage
Branch

Direction du
Patrimoine de l'édition

395 Wellington Street
Ottawa ON K1A 0N4
Canada

395, rue Wellington
Ottawa ON K1A 0N4
Canada

Your file *Votre référence*
ISBN: 978-0-494-31320-6
Our file *Notre référence*
ISBN: 978-0-494-31320-6

NOTICE:

The author has granted a non-exclusive license allowing Library and Archives Canada to reproduce, publish, archive, preserve, conserve, communicate to the public by telecommunication or on the Internet, loan, distribute and sell theses worldwide, for commercial or non-commercial purposes, in microform, paper, electronic and/or any other formats.

The author retains copyright ownership and moral rights in this thesis. Neither the thesis nor substantial extracts from it may be printed or otherwise reproduced without the author's permission.

AVIS:

L'auteur a accordé une licence non exclusive permettant à la Bibliothèque et Archives Canada de reproduire, publier, archiver, sauvegarder, conserver, transmettre au public par télécommunication ou par l'Internet, prêter, distribuer et vendre des thèses partout dans le monde, à des fins commerciales ou autres, sur support microforme, papier, électronique et/ou autres formats.

L'auteur conserve la propriété du droit d'auteur et des droits moraux qui protègent cette thèse. Ni la thèse ni des extraits substantiels de celle-ci ne doivent être imprimés ou autrement reproduits sans son autorisation.

In compliance with the Canadian Privacy Act some supporting forms may have been removed from this thesis.

Conformément à la loi canadienne sur la protection de la vie privée, quelques formulaires secondaires ont été enlevés de cette thèse.

While these forms may be included in the document page count, their removal does not represent any loss of content from the thesis.

Bien que ces formulaires aient inclus dans la pagination, il n'y aura aucun contenu manquant.


Canada

Abstract

Fingering has been studied in different fluid systems. Viscous fingering, which is driven by a difference in viscosity between fluids, has been studied by both experiments and numerical simulations. We used a single fluid with a temperature-dependent viscosity and studied the instability for a range of inlet pressures and viscosity ratios. The spreading and fingering of a fluid drop subjected to a centrifugal force, known as spin coating, has also been studied for a range of drop volumes and rotation speeds, both for a Newtonian and a non-Newtonian fluid.

Experiments on viscous fingering with a single fluid, glycerine, show that an instability occurs at the boundary separating hot and cold fluid. The results indicate that the instability is similar to that which occurs between two miscible fluids. Fingering only occurs for high enough values of the inlet pressure and viscosity ratio. The wavelength of the fingering pattern is found to be proportional to the cell width for the two smallest cell widths used. The fingering patterns seen in the simulations are very similar to the experimental patterns, although there are some quantitative differences. In particular, the wavelength of the instability is seen to depend only weakly on the cell width.

The spreading of silicone oil, a Newtonian fluid, during spin coating follows the time dependence predicted theoretically, although with a shift in the scaled time variable. Once the radius of the spreading silicone oil drop becomes large enough, fingers

form around the perimeter of the drop for all experimental conditions studied. The number of fingers and the growth rate of the fingers are in agreement with theoretical predictions. Fingers are also observed to form for high enough drop volumes and rotation speeds during the spinning of a non-Newtonian fluid drop, Carbopol, which possesses a yield stress. In this case the fingering is a localized effect, occurring once the stress on the drop exceeds the yield stress, rather than the result of an instability as in the Newtonian case.

Acknowledgements

I would like to thank my supervisor, Dr. John de Bruyn, for his valuable help and encouragement over the years. I acknowledge useful discussions with G. M. Homsy, J. Wylie, Y. Yortsos, N. P. Chafe, and A. Walsh. As well, I would like to thank E. Thornhill for helpful discussions and assistance with designing the numerical grid described in Chapters 3 and 4. I acknowledge the work and contributions P. Habdas, N. Semsarillar, K. Burfitt, and H. Tabuteau to the work presented in Chapters 5 and 6. I would like to thank W. Holly and R. Guest for assistance with various items during the course of this research and our past and present machinists, Bill Keiley and Gordon Whelan, for their assistance in creating and maintaining the various experimental apparatus used during my research. The numerical simulations described in this thesis were done using the computer resources of the Atlantic Computational Excellence Network at Memorial University. The research was supported by the National Sciences and Engineering Research Council of Canada and, in part, by an Atlantic Accord Career Development Award.

Dedication

I dedicate this thesis to my family: my husband who has provided immense support and encouragement, my parents and my sister who have always believed in me, and my nephew James who, no matter what, always makes me smile.

Contents

Abstract	ii
Acknowledgements	iv
Dedication	v
List of Figures	xx
1 Introduction	1
1.1 Overview	1
1.2 Viscous Fingering	3
1.2.1 Linear Stability Analysis	7
1.3 Newtonian and non-Newtonian Fluids	12
1.4 Spin coating	14
1.4.1 Theory	17
1.4.2 Previous work on spin coating of yield stress fluids	23
1.5 Outline	24
2 Co-authorship Statement	32
2.1 Chapters 3: Viscous fingering with a single fluid; authors: K. E. Hol- loway and J. R. de Bruyn	32

2.2	Chapter 4: Numerical simulations of a viscous fingering instability in a fluid with a temperature-dependent viscosity; authors: K. E. Holloway and J. R. de Bruyn	33
2.3	Chapter 5: Spreading and fingering during spin coating; authors: K. E. Holloway, P. Habdas, N. Semsarillar, K. Burfitt, and J. R. de Bruyn	34
2.4	Chapter 6: Fingering in a yield-stress fluid during spin coating; authors: K. E. Holloway, H. Tabuteau, and J. R. de Bruyn	34
3	Viscous fingering with a single fluid	36
3.1	Abstract	36
3.2	Introduction	36
3.3	Experiment	41
3.4	Results	43
3.5	Simulations	51
3.6	Discussion	55
3.7	Conclusion	58
4	Numerical simulations of a viscous fingering instability in a fluid with a temperature-dependent viscosity	63
4.1	Abstract	63
4.2	Introduction	63
4.3	Method	66
4.3.1	Problem Set-up	66
4.3.2	Numerical Method	66
4.3.3	Boundary Conditions and Material Parameters	68
4.3.4	Grid and Time Step Independence	69
4.3.5	Validation	70

4.4	Results	73
4.5	Discussion	87
4.6	Conclusion	90
5	Spreading and fingering in spin coating	94
5.1	Abstract	94
5.2	Introduction	95
5.3	Experiment	98
5.4	Results	99
5.5	Discussion	112
5.6	Conclusion	116
6	Spreading and fingering in a yield-stress fluid during spin coating	120
6.1	Abstract	120
6.2	Introduction	121
6.3	Experimental Method and Materials	123
6.4	Results	125
	6.4.1 Rheology	125
	6.4.2 Spreading and fingering	125
6.5	Discussion	133
6.6	Conclusion	137
7	Summary	142
7.1	Viscous fingering	142
7.2	Spin coating	144
	7.2.1 Newtonian fluid — silicone oil	144
	7.2.2 Non-Newtonian fluid — Carbopol	144

7.3	Future Work	145
A	Thermoviscous Fingering	149
A.0.1	Introduction	149
A.0.2	Experiments	151
A.0.3	Results and discussion	153
B	Fluent Equations	161

List of Figures

1.1	A schematic illustration of Rayleigh-Bénard convection.	2
1.2	A schematic illustration of the Saffman-Taylor fingering instability. The patterned area indicates the injected, less viscous fluid which is moving to the right. A finger of the less viscous fluid is shown penetrating into the more viscous fluid.	4
1.3	A simplified sketch of horizontal flow with two immiscible fluids through a Hele-Shaw cell. The interface is initially straight and is indicated by the solid line. The dashed line represents perturbations applied to the interface.	8
1.4	A stress τ applied to the top plate results in a velocity gradient within the fluid. The fluid near the top plate moves with velocity v_o while the fluid near the bottom plate has 0 velocity. The strain rate is defined as the velocity gradient dv/dz	12
1.5	Schematic flow curves for different types of fluids. (a) Newtonian; (b) shear thickening; (c) shear thinning; (d) yield stress	13
1.6	A schematic illustration of a contact angle. The contact angle θ is the angle the edge of the fluid drop makes with the substrate. For a completely wetting fluid, $\theta = 0$	15

1.7	A cylindrical volume of fluid with initial radius r_o and height H_o on a substrate. The substrate spins with an angular velocity ω	17
1.8	A schematic diagram of flow down an inclined plane. The coordinate system used in the linear stability analysis of Troian et al. [48] is shown.	20
1.9	A sketch of the solution to Eq. (1.33).	22
1.10	Two adjacent microgel particles. Within the dashed circle is the interior of the microgel in which there are many crosslinks between polymer strands. Dangling ends of polymer molecules on the exterior of the microgel particles interact with surrounding particles.	24
3.1	The experimental apparatus used in the fingering experiments. Glycerine is confined between the upper and lower surfaces of the cell and within the cylinder below the cell (the shaded areas in the figure). The glycerine in the cell is maintained at a temperature T_c while the glycerine in the cylinder is dyed black and maintained at a higher temperature T_h . The piston is used to force the hot glycerine into the cell. The flow is visualized by a video camera mounted above the apparatus.	42
3.2	A sequence of images from a run of the experiment with $b = 1$ mm, $P = 74.8$ kPa, $T_c = 284.48$ K, and $T_h = 343.15$ K. The images were recorded at times (a) 0.33 s, (b) 0.75 s, (c) 0.92 s, and (d) 1.17 s after the start of the experiment. The field of view is 8.8 cm.	45
3.3	Images from runs of the experiment with different cell widths b . For all three runs $T_h = 343.15$ K. (a) $b = 0.5$ mm, $P = 189.6$ kPa, $T_c = 275.77$ K, (b) $b = 1$ mm, $P = 67.2$ kPa, $T_c = 277.94$ K and (c) $b = 2$ mm, $P = 76.4$ kPa, $T_c = 280.07$ K. Note the increase in finger width with increasing b	46

3.4 (a) Wavelength of the finger pattern as a function of cell temperature T_c . All runs plotted had $T_h = 343.15$ K but P varied from run to run. Wavelengths are determined by averaging over all fingers in the pattern; a typical standard deviation is shown for one point. Open squares: $b = 0.5$ mm, solid circles: $b = 1$ mm, open triangles: $b = 2$ mm. The dotted lines show the mean wavelength for each cell width, while the standard deviation is indicated by the error bars at the left of the graph. (b) Same as (a), but plotted as a function of driving pressure P . The inset shows the mean wavelength scaled by the cell width as a function of b 47

3.5 The intensity of the dominant peak in the Fourier spectrum of the boundary between injected and displaced fluid as a function of time for an experimental run with $T_c = 280.81$ K, $T_h = 343.15$ C, $P = 62.7$ kPa, and $b = 1$ mm. At early times, the intensity increases exponentially. The dashed line is a fit to the data at early times; its slope gives the exponential growth rate of the fingers. 49

3.6 The measured stability diagram for $b = 1$ mm. The abscissa is the *initial* viscosity ratio m . The solid circles indicate conditions for which fingers were observed, while the open triangles show points for which fingering was not observed. The dashed line is a guide to the eye indicating the approximate location of the boundary above which the fingering instability occurs. 50

3.7	A time sequence of images from a simulation of the displacement of cold glycerine by injected hot glycerine. The gray scale represents temperature, with white being hot and black, cold. These images show the temperature at the midplane of the cell for $T_c = 278.15$ K, $T_h = 343.15$ K, $b = 1$ mm, and inlet velocity $v_i = 2$ m/s. The images are at times (a) 0.02 s, (b) 0.06 s, (c) 0.1 s, (d) 0.18 s.	52
3.8	(a) The stability diagram determined from simulations with $b = 1$ mm. The symbols are as in Fig. 3.6. Here the ordinate is the injection velocity of the hot glycerine, which was the quantity controlled in the simulations. The dashed line is a guide to the eye. (b) The same data plotted in terms of the initial pressure at the inlet to the cell.	54
4.1	A sketch of the problem to be solved. The geometry consists of two circular, parallel walls at a temperature T_c separated by a small gap b . The cell initially contains fluid at temperature T_c . Fluid with $T_h > T_c$ is injected through a small hole in the center of the bottom wall. . . .	67
4.2	A segment of the midplane of the numerical grid used in the simulations. The grid consists of 364520 wedge shaped cells with 10 levels in the vertical direction.	67
4.3	Temperature along a radial line in the midplane of the cell at a time of 0.01 s for several different numerical grids. The time step was 0.0001 s, $T_c = 275$ K, $v_i = 2$ mm, and $b = 1$ mm.	71
4.4	(a) Number of fingers at a time of 0.01 s as a function of the number of cells in the numerical grid. The time step here is 0.0001 s. (b) Number of fingers at a time of 0.15 s as a function of time step for a grid with 364520 cells. For all runs shown here, $T_c = 275K$ and $v_i = 2$ m/s. . .	72

4.5	(a) Results from a simulation of glycerine injected into water with $b = 1$ mm and $v_i = 2$ m/s at a time of 0.2 s. (b) Water injected into glycerine for the same conditions as (a). Light and dark represent glycerine and water respectively.	74
4.6	Contours of radial velocity on the midplane of the cell from a simulation with $b = 1$ mm, $v_i = 1$ m/s, $T_c = 284$ K, and $T_h = 343.15$ K at (a) 0.02 s and (b) 0.14 s. The field of view is 0.0439 m.	75
4.7	A simulation image showing the temperature in the midplane of the cell corresponding to Fig. 4.6(b). Light represents T_h and dark, T_c . . .	76
4.8	An image from an experimental run with $b = 1$ mm, $T_c = 280.81$ K, and inlet pressure $P = 62700$ Pa at a time of 1.1 s after the start of the run. The hot glycerine is dyed black to distinguish it from the cold glycerine initially in the cell.	77
4.9	A grayscale simulation image showing the tangential velocity in the cell midplane overlaid with contours of radial velocity. The light and dark areas (indicating positive and negative tangential velocity, respectively) show that flow is focused towards the finger tips. The conditions were the same as in Fig. 4.7.	79
4.10	(a) An image from a simulation with $b = 1$ mm, $v_i = 2$ m/s, and $T_c = 275$ K at a time of 0.016 s. Black represents the injected hot glycerine and the surrounding gray represents the colder glycerine. (b) The Fourier power spectrum of $r(\theta)$ determined from the boundary in (a). (c) Amplitude as a function of time of the peak at $n = 8$. A fit to the data at early times is indicated by the solid line.	81

4.11 (a) The wavelength λ of the fingers as a function of inlet velocity obtained from the simulations. Open squares: $b = 0.5$ mm; solid circles: $b = 1$ mm; open triangles: $b = 2$ mm. (b) Wavelength as a function of T_c	82
4.12 The wavelength averaged over T_c and v_i plotted as a function of cell width b for both simulations (solid circles) and experiment (open circles). The inset shows the ratio λ/b for both cases.	83
4.13 The scaled growth rate σt_κ as a function of scaled inlet velocity $v_i t_\kappa / b$ obtained from the simulations. Squares: $b = 0.5$ mm, circles: $b = 1$ mm, triangles: $b = 2$ mm.	85
4.14 A stability diagram showing the range of existence of the fingering instability determined from the simulations for $b = 1$ mm. The solid circles represent simulations for which fingering was observed and the open triangles cases where there was no fingering. The dashed line is the approximate stability boundary above which the flow is unstable and below which it is stable.	86
4.15 Velocity vectors shown for a portion of a vertical plane of the numerical grid. The field of view is 3 mm and the inlet hole is at the bottom left in each case. (a) $b = 0.5$ mm, $v_i = 1$ m/s, $T_c = 278.15$ K, $t = 0.018$ s; (b) $b = 1$ mm, $v_i = 1.5$ m/s, $T_c = 275$ K, $t = 0.02$ s; and (c) $b = 2$ mm, $v_i = 3.5$ m/s, $T_c = 280$ K, $t = 0.035$ s. The velocity vectors show increased three-dimensional flow as b is increased.	89

5.1	Shadowgraph images showing the spreading and fingering of a droplet of volume $V = 50\mu\text{l}$. The outer edge of the dark annular region corresponds to the edge of the drop. The angular speed ω of the turntable is 36.8 rad/s. Time $t = 0$ corresponds to the start of the rotation. At $t = 1.45$ s (a) the drop is circular. At $t = 11.45$ s (b) perturbations have started to grow around the perimeter of the drop. In image (c) ($t = 21.45$ s) and (d) ($t = 31.45$ s) fingers have developed and grown.	101
5.2	Spreading of drops of volume $V = 100 \mu\text{l}$. (a) shows r/r_0 as a function of time for several drops of the same volume with angular velocities ω ranging from 26.3 rad/s to 57.8 rad/s, indicated by the different symbols. The higher slopes correspond to higher values of ω . (b) shows the same data with logarithmic axes.	102
5.3	r/r_0 plotted as a function of scaled time, t/t_0 , where t_0 is defined in the text. 23 different data sets are shown, covering a range of volumes and angular speeds. The dashed line is the prediction of Eq. 5.2, and the dotted line is a 1/4-power law plotted for comparison.	104
5.4	The slope of the apparently linear region of the spreading data $r(t)/r_0$ vs. t shown in Fig. 5.2 plotted as a function of volume (a) and angular speed (b). In (a), the open circles are for $\omega = 26.3$ rad/s, the solid circles for $\omega = 42.0$ rad/s, and the dashed line is a power law with exponent 0.73. In (b) the open squares are for $V = 50 \mu\text{l}$, the solid squares for $V = 100 \mu\text{l}$, and the dashed line is a power law with an exponent 2.47.	105

5.5	<p>(a) The Fourier power spectrum of the perimeter of a drop with $V = 50\mu\text{l}$ a time $t = 21.45$ s after the start of spinning at $\omega = 36.8$ s⁻¹. n is the azimuthal wave-number. (b) The Fourier power of the fastest growing mode at $n = 7$ for the same run as in (a). The onset time of the fingering instability t_c is indicated by the arrow, and the dashed line is a fit to an exponential growth law at early times after the onset.</p>	107
5.6	<p>The exponential growth rate σ as a function of mode number n for the run of Fig. 5.5.</p>	108
5.7	<p>The growth rate σ of the fingers plotted against ω in (a) and against volume V in (b). In (a) the open squares are for $V = 50 \mu\text{l}$, the solid squares for $V = 100 \mu\text{l}$, and the dashed line is a power law fit to the data for $V = 100 \mu\text{l}$. In (b), the open circles are for $\omega = 26.3$ rad/s, the solid circles for $\omega = 42.0$ rad/s, and the dashed line is a straight line fit to the higher ω data.</p>	109
5.8	<p>The scaled growth rate plotted as a function of ω in (a) and against V in (b). The dashed line is the mean value in each case. The experimental parameters and symbols are the same as in the previous figure.</p>	110
5.9	<p>The critical radius r_c as a function of ω (a) and as a function of V (b). In (a), the open squares are for $V = 50\mu\text{l}$ and solid squares for $V = 100\mu\text{l}$. In (b), the open circles are for $\omega = 26.3$ rad/s and solid circles for $\omega = 42.0$ rad/s. The two dashed lines in (a) show the average values of the data and in (b) the dashed line is a fit to all of the data.</p>	111

5.10	The number of fingers n as a function of V for two values of the rotation speed. The open circles are for $\omega = 26.3$ rad/s and the solid circles for $\omega = 42.0$ rad/s. The dashed lines are the predictions of the theoretical expression, Eq. 5.4, using the fits to the experimental data for the critical radius r_c shown in Fig. 5.9. There are no free parameters. The inset shows the ratio of the predicted number of fingers, calculated using the individual measured values of r_c , to the measured value of n .	113
5.11	n as a function of ω for $V = 50 \mu\text{l}$ (open squares) and $V = 100 \mu\text{l}$ (solid squares). The dashed lines are again the predictions of Eq. 5.4, using the fits to the data for r_c shown in Fig. 5.9. The inset shows the ratio of the predicted number of fingers, calculated using the individual measured values of r_c , to the measured value of n .	114
6.1	Mean measured flow curves for $c = 0.2\%$ (circles) and $c = 0.4\%$ (squares). The lines are fits to the data using the Herschel-Bulkley model, Eq. (6.1).	126
6.2	The elastic modulus G' (circles) and viscous modulus G'' (squares) as a function of frequency for 0.2% carbopol (solid symbols) and 0.4% carbopol (open symbols).	127
6.3	Images from a run with $c = 0.4\%$ showing the development of a finger as a function of time. For this run, $V = 0.5$ ml and $\omega = 47.3$ rad/s. Images were recorded at (a) 0.17 s, (b) 22.1 s, (c) 59.76 s, and (d) 77.34 s. The Carbopol drop appears dark, with light areas within the drop indicating variations in the drop's thickness. A ridge of fluid, indicated by a light region, can be seen close to the perimeter. The field of view is approximately 5.3 cm.	129

6.4	Images from a run with $c = 0.4\%$ showing the formation and growth of several fingers. Here $V = 1$ ml and $\omega = 63$ rad/s. Images were recorded at (a) 0.57 s, (b) 2.90 s, (c) 4.57 s, and (d) 11.23 s. The field of view is 8.2 cm.	130
6.5	The radial strain γ_r plotted as a function of time for a Carbopol drop with $c = 0.4\%$ which was not observed to finger. Here $V = 0.5$ ml and $\omega = 21$ rad/s.	131
6.6	(a) The radial strain γ_r as a function of time for $V = 0.5$ ml. The different symbols represent runs with different ω . From top to bottom, $\omega = 63, 52.5, 57.8,$ and 42 rad/s. (b) γ_r as a function of time for $\omega = 52.5$ rad/s. The different symbols represent runs with different V . From top to bottom, $V = 0.75, 0.6, 0.4, 0.3,$ and 0.2 ml.	132
6.7	The maximum distance of the edge of the carbopol drop from the center of the fitted circle as a function of time for a run with $c = 0.4\%$, $V = 0.4$ ml, and $\omega = 52.5$ rad/s. The time at which the radial strain reaches 0.17 is indicated by the arrow.	134
6.8	(a) Experimentally determined stability of $c = 0.4\%$. Open circles: fingers, closed circles: no fingers. The dashed line is the predicted stability boundary given by Eq. (6.2), multiplied by a factor of 2. (b) ω versus $\sqrt{\tau_o/\rho r_o}$ for $c = 0.2\%$ (squares) and 0.4% (circles). The open symbols correspond to parameters for which a finger(s) was seen while the solid symbols correspond to parameters for which a finger(s) was not seen. The dashed line shows the prediction of Eq. (6.2) with $h_o = 0.18$ mm.	135

A.1	A schematic illustration of the apparatus used to study thermoviscous fingering.	153
A.2	A sequence of images from a run with $b = 0.5$ cm, T_c set at -20°C , and $T_h = 90^\circ\text{C}$. A finger is seen in the lower left hand corner and by (c) most of the glycerine is flowing through this finger.	156
A.3	A sequence of images from a run with the same conditions as the run in Fig. A.2. In (a) a finger is seen to develop at the glycerine-air interface. In (b) and (c) dye lines show three fingers.	157
A.4	Dye lines show small ripple-like protrusions. The black rectangle is used to define the position of the ripples. Here $b = 0.5$ cm, $T_c = -30^\circ\text{C}$ and $T_h = 90^\circ$	158
A.5	Dye lines show two fingers; one on the right hand side and the other on the lower left hand side. Here $b = 0.5$ cm, T_c is set at -20°C and $T_h = 90^\circ\text{C}$	159

Chapter 1

Introduction

1.1 Overview

Fluid instabilities are commonly seen in everyday life. From the flow of a blob of paint down to a wall to Kelvin-Helmholtz patterns [1] seen in clouds, fluid instabilities are everywhere and can lead to many different types of beautiful patterns. The focus of this thesis is on fingering instabilities — instabilities which result in fingers of a fluid forming and penetrating into another fluid. This type of instability will be discussed in more detail later.

A system, fluid or otherwise, can be characterised as linearly stable or unstable based on its response to small perturbations or disturbances [2]. A system is considered unstable if the applied perturbations grow in time; if the perturbations die out, the system is stable. A system can be stable to small perturbations but unstable to larger perturbations, in which case it is linearly stable but nonlinearly unstable. Perturbations can be deliberately introduced into the system or may simply be due to imperfections in the system.

Rayleigh-Bénard convection [3] is a well known example of a pattern forming

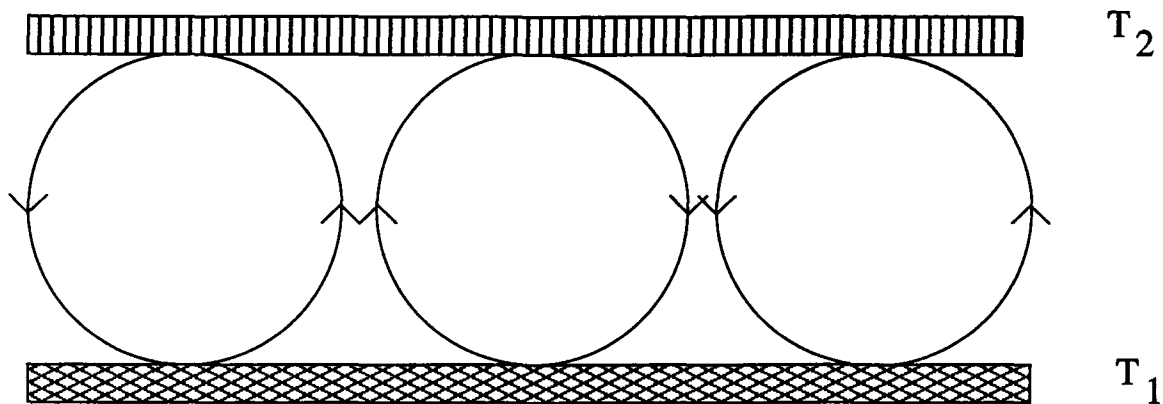


Figure 1.1: A schematic illustration of Rayleigh-Bénard convection.

instability and provides a nice illustration of a system which becomes unstable when the control parameter is large enough. The basic set-up is sketched in Fig. 1.1. A horizontal layer of fluid is confined between two parallel plates with an imposed temperature difference in the vertical direction. The bottom plate is maintained at a temperature T_1 , while the upper plate is maintained at a temperature T_2 , where $T_1 > T_2$. The base state of the system is one in which the flow of heat is solely by conduction, with no fluid motion. The fluid near the bottom plate is less dense than fluid near the upper plate due to the higher temperature near the bottom plate. There is an unstable density configuration: the lower fluid wants to move upwards while the upper fluid wants to move downwards. When $\Delta T = T_1 - T_2$ is large enough for this buoyancy effect to overcome the opposing effects of viscosity and the cooling of the hot fluid as it flows upward (and vice versa), the fluid starts to flow, forming a pattern of convection rolls as shown in Fig. 1.1. The convection rolls have a characteristic length in the horizontal direction, referred to as the wavelength, which depends on the distance between the two plates.

Another example of pattern formation is fingering, which occurs when the boundary between two regions of fluid becomes unstable. There are many examples of these

instabilities. In this thesis, two fingering instabilities observed in different systems will be discussed: viscous fingering [4], which results from a viscosity difference between fluids, and a fingering instability observed during the spreading of a fluid drop due to a centrifugal force [5, 6], a process known as spin coating. Fingering instabilities also occur at the contact line of fluid flowing down an inclined plane [7] and when fluid spreads due to surface tension effects [8, 9]. Another well-known fingering instability is the so-called Printer's instability [10], which occurs at the front of a thin layer of fluid contained in the gap between two acentric rotating cylinders. When one of the cylinders is rotated at a high enough rate, fingers of the fluid form at the fluid-air interface. Fingering patterns are also seen during electrochemical deposition [11]. The flow of lava upwards through fissures in the Earth's crust is subject to an instability known as thermoviscous fingering [12, 13, 14, 15, 16]. Fingering instabilities are interesting to study from a fundamental point of view but are also important from an industrial and geological perspective. For instance, viscous fingering is known to occur during the extraction of oil [17]. The process of spincoating is used to produce thin uniform films in many industries including, for example, the electronics industry. In both of these cases, fingering limits the effectiveness of the process. Understanding the physical processes which cause fingering in these applications may lead to a means of controlling or suppressing it.

1.2 Viscous Fingering

The Saffman-Taylor fingering instability occurs when a less viscous fluid displaces a more viscous fluid [4]. As shown in Fig. 1.2, under appropriate conditions, fingers of the less viscous fluid penetrate into the more viscous fluid. This instability occurs during the extraction of oil from the ground, a porous medium, when water or other

low-viscosity fluids are injected into the reservoir to displace the oil [17]. Fingers of the injected fluid can form and limit the amount of oil which can be extracted. Typically, laboratory experiments focus on studying this instability in a Hele-Shaw cell — a cell consisting of two parallel plates separated by a small gap of width b , where b is much smaller than the cell's other dimensions [18]. This is due to the analogy between flow in a Hele-Shaw cell and flow in porous media, as will be discussed later.

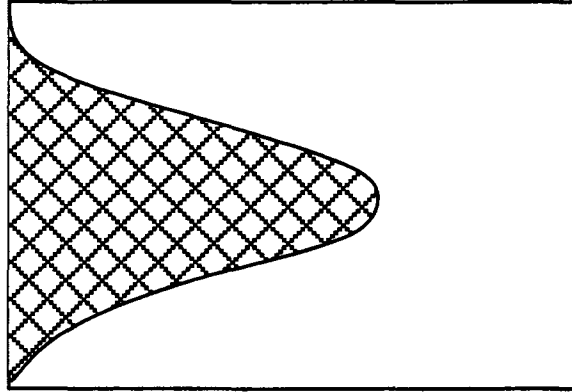


Figure 1.2: A schematic illustration of the Saffman-Taylor fingering instability. The patterned area indicates the injected, less viscous fluid which is moving to the right. A finger of the less viscous fluid is shown penetrating into the more viscous fluid.

Viscous fingering has been studied using both immiscible [4, 18, 19, 20, 21, 22] and miscible fluids [19, 23, 24, 25, 26, 27, 28]. The system studied in Chapters 3 and 4 of this thesis, in contrast, uses a single fluid with a temperature-dependent viscosity. Similarities exist between this system and, in particular, fingering between two miscible fluids but there are also important differences, as will be discussed further in Chapter 3.

In the case of two immiscible fluids, there is a sharp interface separating the fluids, with the viscosity dependent on the fluids in question and constant on each side of the interface. The capillary number $Ca = \mu v / \sigma$ is the important dimensionless parameter, measuring the importance of viscous forces relative to surface tension.

Here μ is the viscosity, v is a characteristic velocity, and σ is the surface tension. Linear stability analysis of this system [2, 4], discussed in Section 1.2.1, shows that when the viscosity ratio $M = \mu_1/\mu_2 > 1$ the interface between the fluids is unstable and fingers develop. Here the subscripts 1 and 2 represent the displaced and displacing fluids, respectively. Surface tension acts to keep the interface between the two fluids straight in order to minimize the energy of the interface. However, the development of a bump on the interface, due to imperfections in the surroundings, provides a lower-resistance pathway for flow. The effect of surface tension on the stability of the interface will be further discussed in Section 1.2.1.

In the case of miscible fluids, viscosity is a function of concentration c , $\mu = \mu(c)$ and the boundary between the fluids, initially sharp, broadens with time as the two fluids mix. In this case, there is no surface tension and molecular diffusion acts as the stabilizing influence. The important dimensionless parameter here is the Peclet number $Pe = lv/D$, which measures the importance of convective flow relative to diffusion. Here l is a characteristic length, v is a characteristic velocity, and D is the diffusion coefficient. Linear stability analysis for miscible fluids [25], discussed briefly in Section 1.2.1, shows that fingering only occurs when $M > 1$.

Reviews of previous work on viscous fingering are given by Homay [19] and Kessler et al. [20]. Saffman and Taylor [4] first studied the linear stability of the interface between two immiscible fluids. Park and Homay [29] developed a theory for the immiscible displacement of a more viscous fluid by a less viscous fluid in a Hele-Shaw cell. The linear stability analysis of the boundary between two miscible fluids has also been studied [25, 28, 30]. Yang and Yortsos [31] theoretically studied miscible displacements. As well, miscible viscous fingering has been numerically studied [26, 27, 28, 32, 33, 34, 35]. Chen and Meiburg [36] performed simulations of miscible displacements in capillary tubes.

Much experimental work has focussed on investigating viscous fingering between immiscible fluids (see Ref. [18] for a review). More relevant to the present work, however, is the experimental work which has been performed on fingering between miscible fluids. Paterson studied fingering between two miscible fluids in a radial Hele-Shaw cell [24]. He injected water into glycerine through the center of a plate of the cell for a range of cell widths and injection rates. He found that the wavelength λ of the resulting instability followed the relationship $\lambda = 4b$. This result agreed with his theoretical predictions based on the minimization of the viscous dissipation of energy [24]. In general, this argument is not accepted, however, as there is no reason to expect that this system will tend to minimize dissipation of energy [37]. Snyder and Tait [38] investigated miscible viscous fingering in a rectangular geometry. For the range of cell widths and viscosity ratios they used, they found $\lambda \approx 2b$. They repeated Paterson's analysis for the rectangular geometry and also found $\lambda \approx 4b$ [38]. Lajeunesse et al. [39, 40, 41] studied miscible viscous fingering in a vertical Hele-Shaw cell in which the upper fluid was less dense, so the system was gravitationally stable. The experiments were performed for a range of viscosities, densities, and flow rates using silicone oils as the experimental fluids. The experiments were all done at high Peclet numbers. They found that fingering only occurred once critical values of the viscosity ratio ($M_c \approx 1.5$) and inlet velocity $U_c(M)$ were exceeded. They found $\lambda = (5 \pm 1)b$. The displacement of a less viscous fluid by a more viscous fluid in a capillary tube has also been studied experimentally [36, 42]. As well, miscible viscous fingering in several different porous media has been experimentally studied using an acoustic technique [43].

Fernandez et al. [44, 45] studied the related Rayleigh-Taylor instability in which the instability is driven by a density difference instead of a viscosity difference. Their experiments were performed in a vertical Hele-Shaw cell using mixtures of water and

glycerine of varying concentrations as the experimental fluids. The more dense fluid lay above a less dense fluid in the cell. The relevant parameter for their experiments was the Rayleigh number $Ra = vb/D$ where v is a characteristic velocity, b is the width of the cell, and D is the molecular dispersion coefficient. For high Ra values ($Ra \geq 100$), they found that $\lambda = (5 \pm 1)b$, while for lower Ra values, $\lambda \propto 1/Ra$. It is interesting to note that Maxworthy [22] also observed a wavelength proportional to the cell width ($\lambda \approx 5b$) in experiments in which air was injected into various silicone oils in a radial Hele-Shaw cell for large Ca .

In Chapters 3 and 4 viscous fingering using only a single fluid in which the viscosity difference between the fluids comes from a difference in temperature will be discussed.

1.2.1 Linear Stability Analysis

This section contains a review of the linear stability analysis of the interface between two immiscible fluids contained in Ref. [2].

For flow in a Hele-Shaw cell, $b \ll l$ where b is the width of the cell and l is a characteristic length in the horizontal direction, so thin-film theory applies. The z -direction is taken to be the vertical direction. In this case, the Navier-Stokes equation reduces to [1]

$$\nabla P = \mu \frac{\partial^2 \vec{u}}{\partial z^2} \quad (1.1)$$

where μ is the viscosity, P is the pressure, and \vec{u} is the velocity. Integrating over z twice and applying the condition that $\vec{u} = 0$ at $z = \pm b/2$ gives

$$\vec{u} = \frac{1}{2\mu} \left(z^2 - \frac{1}{4}b^2 \right) \nabla P. \quad (1.2)$$

Averaging \vec{u} over the width of the cell gives

$$\langle \vec{u} \rangle = -\frac{b^2}{12\mu} \nabla P. \quad (1.3)$$

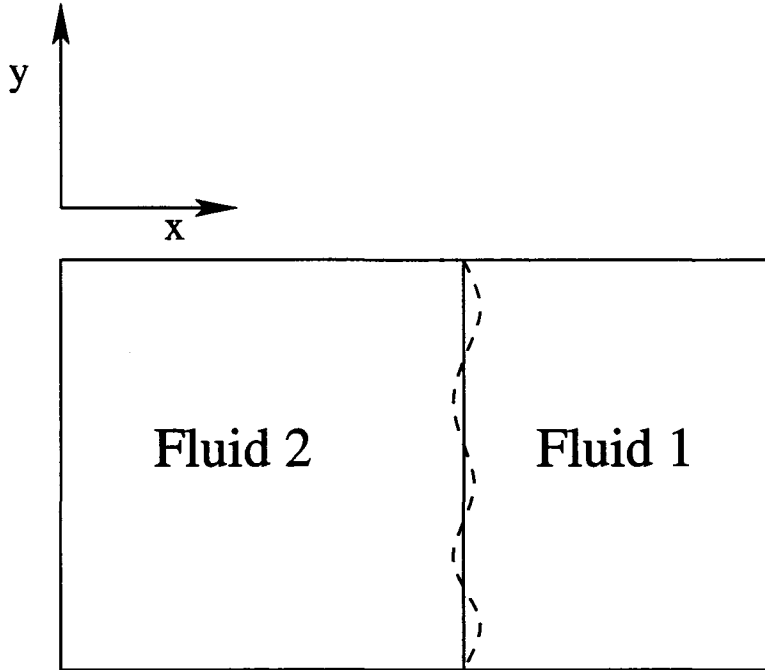


Figure 1.3: A simplified sketch of horizontal flow with two immiscible fluids through a Hele-Shaw cell. The interface is initially straight and is indicated by the solid line. The dashed line represents perturbations applied to the interface.

Consider the case of two immiscible fluids in a horizontal Hele-Shaw cell with fluid 2 displacing fluid 1, driven by a pressure p . The two fluids are separated by an initially straight interface. In the absence of fingering, the interface moves with velocity U in the x -direction such that the position of the interface is given by $x_o = Ut$. A simplified sketch of this situation is shown in Fig. 1.3. The subscripts 1 and 2 refer to the fluid for which $x > Ut$ and $x < Ut$ initially, respectively.

In this situation, Eq. (1.3) can be rewritten as

$$\begin{aligned}\frac{\partial P_2}{\partial x} &= -\frac{12\mu_2 U}{b^2} & \text{if } x < Ut \\ \frac{\partial P_1}{\partial x} &= -\frac{12\mu_1 U}{b^2} & \text{if } x > Ut\end{aligned}\quad (1.4)$$

to describe the initial flow of the fluids. As an aside, note that Eq. (1.3) is equivalent to Darcy's law [18, 19], an empirically derived formula for flow in porous media,

$$U = -\frac{\kappa}{\mu}\nabla P \quad (1.5)$$

if the permeability of the medium κ is replaced with $b^2/12$. This shows an analogy between flow in a Hele-Shaw cell and flow in a porous medium. From Eq. (1.4), the pressure in the two fluids can be expressed as

$$\begin{aligned}P_2 &= -\frac{12\mu_2 U}{b^2}(x - x_o) + P_o \\ P_1 &= -\frac{12\mu_1 U}{b^2}(x - x_o) + P_o\end{aligned}\quad (1.6)$$

where $x_o = Ut$, the initial position of the interface, and P_o is the pressure at the interface at time $t = 0$.

Consider small perturbations applied to the initially straight interface at $x_o = Ut$ such that the position of the interface X is given by

$$X = Ut + \xi_Q e^{iQy}, \quad (1.7)$$

where ξ_Q is the amplitude of the perturbation and Q is the wavenumber of the perturbations ($\lambda = 2\pi/Q$). The normal components of velocity must be continuous across the interface, $\langle \vec{u}_2 \rangle_x = \langle \vec{u}_1 \rangle_x = \partial X / \partial t$. From Eq. (1.7), $\partial X / \partial t = U + \partial \xi_Q / \partial t e^{iQy}$.

From this and Eq. (1.3),

$$-\frac{b^2}{12\mu_2} \frac{\partial P_2}{\partial x} = -\frac{b^2}{12\mu_1} \frac{\partial P_1}{\partial x} = U + \frac{\partial \xi_Q}{\partial t} e^{iQy}. \quad (1.8)$$

The perturbation on the position of the interface is described by Eq. (1.7). The pressure must also experience a perturbation given by

$$\begin{aligned} P_2 &= -\frac{12\mu_2 U}{b^2} (x - x_o) + P_o + A_2 e^{Q(x-x_o)} e^{iQy} \\ P_1 &= -\frac{12\mu_1 U}{b^2} (x - x_o) + P_o + A_1 e^{-Q(x-x_o)} e^{iQy}. \end{aligned} \quad (1.9)$$

Eq. (1.9) follows from the condition that at large distances from the interface the perturbation approaches 0 and the fact that the that the pressure in both fluids obeys Laplace's equation

$$\frac{\partial^2 P}{\partial x^2} + \frac{\partial^2 P}{\partial y^2} = 0. \quad (1.10)$$

Because of Eq. (1.10), any perturbation on P_1 or P_2 that has a term like e^{iQy} must also have a term like e^{Qx} [2]. Due to surface tension σ at the interface, the condition on the pressure at the interface is

$$P_2 - P_1 = -\sigma \frac{\partial^2 X}{\partial y^2}. \quad (1.11)$$

Using Eq. (1.7) gives

$$P_2 - P_1 = \sigma Q^2 \xi_Q e^{iQy}. \quad (1.12)$$

Using a series expansion for the exponential terms in P_1 and P_2 , and keeping only first order terms in the series, Eq. (1.12) can be written as

$$-\frac{12U}{b^2} (\mu_2 - \mu_1) \xi_Q e^{iQy} + (A_2 - A_1) = \sigma Q^2 \xi_Q e^{iQy}. \quad (1.13)$$

Using Eq. (1.9), Eq. (1.8) can be written, again to first order, as

$$-\frac{b^2 Q}{12\mu_2} A_2 = -\frac{b^2 Q}{12\mu_1} A_1 = \frac{\partial \xi_Q}{\partial t} e^{iQy}. \quad (1.14)$$

Using this equation to express A_1 in terms of A_2 or vice versa and substituting into Eq. (1.13) gives

$$\frac{1}{\xi_Q} \frac{\partial \xi_Q}{\partial t} = \frac{1}{\mu_2 - \mu_1} \left[-U(\mu_2 - \mu_1)Q - \frac{\sigma b^2 Q^3}{12} \right]. \quad (1.15)$$

If $\partial \xi_Q / \partial t > 0$, the interface is unstable and the perturbations grow; if $\partial \xi_Q / \partial t < 0$, the interface is stable and any perturbation dies away. Eq. (1.15) tells us that when $\mu_1 < \mu_2$, that is, when a more viscous fluid displaces a less viscous one, $\partial \xi_Q / \partial t < 0$ and the interface is stable. When $\mu_1 > \mu_2$, the perturbation will grow if Q is larger than a critical value of Q , calculated from Eq. (1.15) by setting $\partial \xi_Q / \partial t = 0$, given by

$$Q_c^2 = \frac{12U(\mu_1 - \mu_2)}{\sigma b^2}. \quad (1.16)$$

The interface is unstable for $Q < Q_c$. Therefore, we see that the effect of surface tension is to stabilize the interface at high wavenumbers.

The stability analysis for the case of miscible fluids is complicated by the fact that the base state is time-dependent due to the effects of dispersion and the fact that the viscosity depends on concentration. Ref. [19] contains a review of the work done on the stability of miscible displacements. Chouke [46] made the first attempt to analysis the stability of the flow for miscible fluids. He found that dispersion acted to stabilize the flow at high wavenumbers, giving a cutoff wavenumber $Q_c = Pe(\mu_1 - \mu_2)/4(\mu_1 + \mu_2)$, where here 1 and 2 refer to zero concentration and maximum concentration, respectively. His results, however, were for short times only. Tan

and Homsy [25] performed a more complete linear stability analysis and found that fingering occurred for $M > 1$. They also found a cutoff wavenumber. Lajeunesse et al. [39, 40, 41] performed a linear stability analysis for the case of a vertical Hele-Shaw cell in which the fluids were arranged in a density stable configuration. They found that the critical viscosity ratio necessary for fingering to occur was given by $M_c = 3/2$.

1.3 Newtonian and non-Newtonian Fluids

Some of the work discussed in the remainder of this chapter and in Chapter 6 will involve non-Newtonian fluids, so a discussion of the properties of Newtonian and non-Newtonian fluids is relevant here. Newtonian fluids are characterized by a constant viscosity μ and obey the relationship $\tau = \mu\dot{\gamma}$. τ is the shear stress acting on the fluid, that is, the force acting tangential to a surface within the fluid divided by the area on which the force acts. $\dot{\gamma}$ is the strain rate, dv/dz , as defined in Fig. 1.4. The flow curve — a plot of shear stress versus strain rate — for a Newtonian fluid shown in Fig. 1.5 (a) shows a linear relationship between shear stress and strain rate with the viscosity μ being the slope of the line.

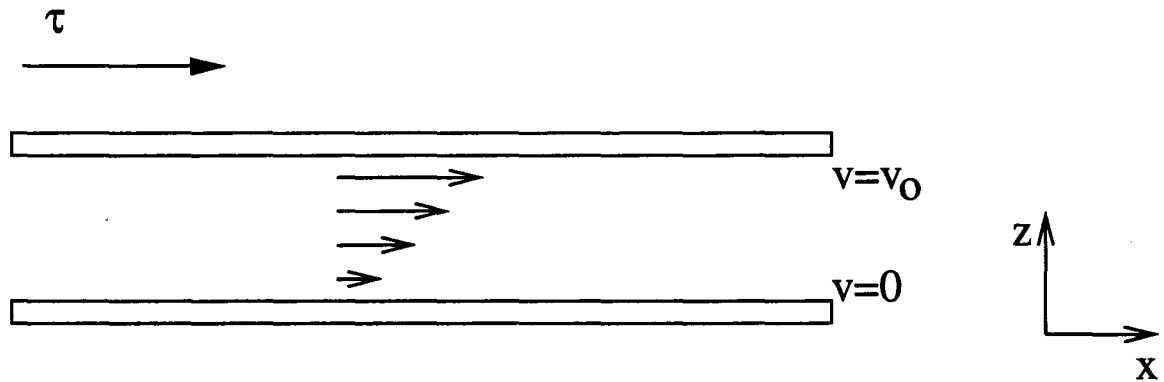


Figure 1.4: A stress τ applied to the top plate results in a velocity gradient within the fluid. The fluid near the top plate moves with velocity v_0 while the fluid near the bottom plate has 0 velocity. The strain rate is defined as the velocity gradient dv/dz .

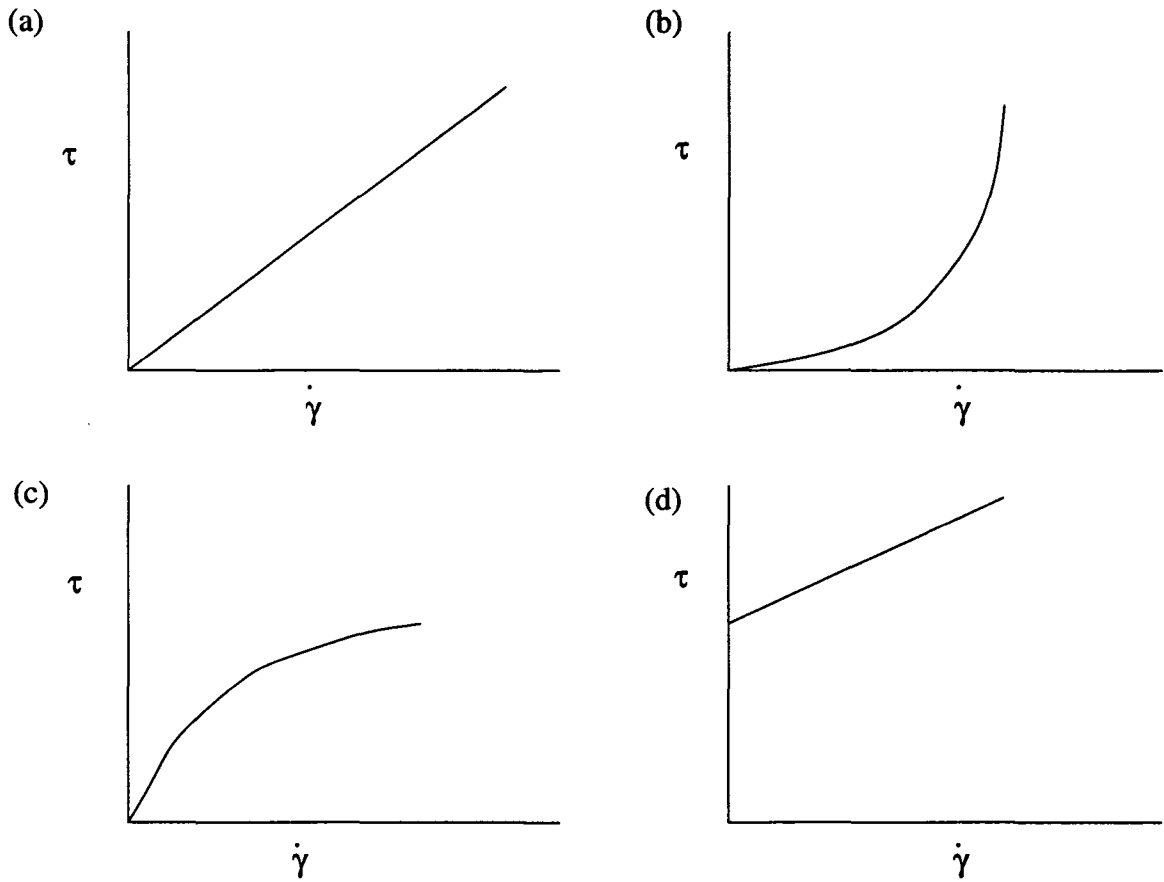


Figure 1.5: Schematic flow curves for different types of fluids. (a) Newtonian; (b) shear thickening; (c) shear thinning; (d) yield stress

Many fluids have a viscosity that is not constant, but depends on strain rate. Such fluids are known as non-Newtonian fluids. Paint and toothpaste are everyday examples. For some fluids, the viscosity increases with strain rate; these are termed shear thickening fluids. An example is a concentrated slurry of corn starch in water which has a flow curve like that shown in Fig. 1.5 (b). On the other hand, if the viscosity decreases with strain rate, the fluid is shear thinning and behaves as in Fig. 1.5 (c). Polymer solutions are examples shear thinning fluids. Ketchup and mud are examples of non-Newtonian fluids which behave like a solid at low stress and a fluid at high stress. These fluids are said to have a yield stress, that is, the fluid does not

flow until the shear stress on the fluid exceeds a certain value. Two models commonly used to describe yield stress fluids are the Bingham plastic model and the Herschel-Bulkley model. Fig. 1.5 (d) shows the flow curve for a Bingham plastic model. The equations describing this behaviour are

$$\dot{\gamma} = 0 \quad \text{if } \tau \leq \tau_o \quad (1.17)$$

$$\tau = \tau_o + \xi \dot{\gamma} \quad \text{if } \tau \geq \tau_o, \quad (1.18)$$

where τ_o is the yield stress and ξ is the Bingham viscosity. The Herschel-Bulkley model is similar but has a nonlinear dependence on strain rate for $\tau > \tau_o$:

$$\dot{\gamma} = 0 \quad \text{if } \tau \leq \tau_o \quad (1.19)$$

$$\tau = \tau_o + \kappa \dot{\gamma}^n \quad \text{if } \tau \geq \tau_o, \quad (1.20)$$

where κ is the consistency of the fluid and n is a power law exponent.

1.4 Spin coating

Chapters 5 and 6 of this thesis discuss the formation of fingers during the spin coating process. Spin coating is used to deposit thin, uniform films on substrates and has many industrial applications, including, for example, the coating of data storage disks [47]. During spin coating, fluid is deposited on a substrate which is then given an angular velocity, causing the fluid to spread outward under the action of the centrifugal force. As the fluid spreads outwards, a capillary ridge may develop around the perimeter of the fluid drop. This ridge can become unstable, leading to the formation of perturbations in the radial direction [48]. Because they experience a

larger centrifugal force, the bumps grow faster than the neighbouring fluid and the result is fingers. In Chapter 5, we discuss the results of a systematic study of this fingering instability for a Newtonian fluid for a large range of fluid volumes and angular velocities. We focus more on the growth rates of the fingers than in previous work [5, 6]. Chapter 6 discusses spreading and fingering of a non-Newtonian fluid drop during spin coating, an area less well studied [67].

A similar instability is seen in flows driven by gravity [48, 49, 50, 51, 52]. When a sheet of fluid flows down an inclined plane under the influence of gravity, fingers are observed to form at the liquid-solid contact line. The phenomenology of the instability is similar to what occurs during spin coating. Flow down an inclined plane has been studied using both Newtonian [50, 51] and non-Newtonian fluids [52]. Marangoni forces, that is, forces due to temperature-induced surface tension gradients can also drive fingering instabilities [8, 9].

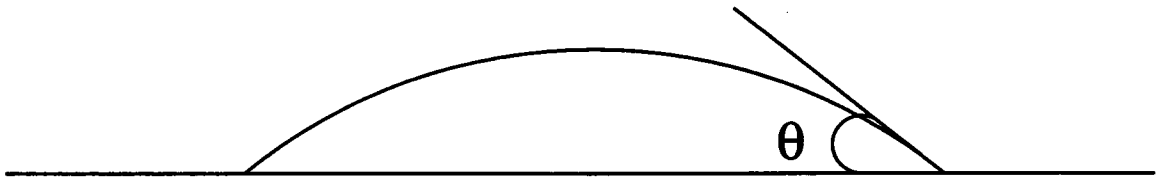


Figure 1.6: A schematic illustration of a contact angle. The contact angle θ is the angle the edge of the fluid drop makes with the substrate. For a completely wetting fluid, $\theta = 0$.

Melo et al. studied spincoating for a range of rotation speeds, fluid volumes, and fluid parameters using silicone oils as the experimental fluids [5]. They investigated the spreading of the drop prior to fingering, the evolution of height at the drop center, the critical radius (that is, the radius at which the instability occurs), and the number of fingers which formed around the perimeter of the fluid drop. Fraysse and Homsy studied spincoating for both Newtonian fluids (silicone oils with different viscosities and a polybutene/kerosene mixture) and an elastic fluid (polyisobutylene

in a polybutene/kerosene solvent) [6]. Their results with the Newtonian and non-Newtonian fluids were qualitatively the same. They used a range of rotation speeds and a limited range of drop volumes. They also examined the spreading of the fluid drops, the critical radius, and the number of fingers that formed at the instability, as well as the growth rate of the fingers. Spaid and Homsy studied spincoating for both Newtonian and viscoelastic fluids [53]. In agreement with their previous theoretical work [54, 55], they found that the effect of the elasticity of the fluid was to stabilize the contact line. Veretennikov et al. investigated spincoating using Newtonian fluids: glycerine, a partially wetting fluid, and Dow Corning 200 Fluid, a completely wetting fluid (see the caption of Fig. 1.6 for a description of contact angle and a completely wetting fluid) [56]. They used a larger drop volume (≈ 0.6 ml) than used in previous work and proposed a different mechanism leading to fingering for partially wetting macroscopic drops than that known to lead to fingering in microscopic drops. Wang and Chou investigated spincoating using large volumes of silicone oils and much higher rotation rates than in previous studies [57]. They studied the effect on the flow and instability of the method used to deposit the fluid volumes on the plate, using a released drop mechanism and also a fluid injection method. They observed no effect for low rotational Bond number (i.e., low rotation speeds) while for high rotation speeds, the method affected the critical radius and the number of fingers, with the fluid injection method resulting in lower numbers for both. Togashi et al. investigated spincoating using two Newtonian fluids, water and a water/glycerine mixture [58]. They used a larger spinning substrate than the above experiments (650×830 mm) and continuously supplied fluid during the spinning process. They studied the effect of changing the rate of fluid injection, the fluid viscosity, and the angular velocity on the onset radius and the number of fingers of the instability.

1.4.1 Theory

Spreading

The spreading of fluid on a substrate subject to a centrifugal force has been studied theoretically by several authors [5, 6, 59, 60, 61]. The following derivation of the time dependence of the radius of the fluid drop is based on the work of Emslie et al. [59] and Fraysse and Homsy [6].

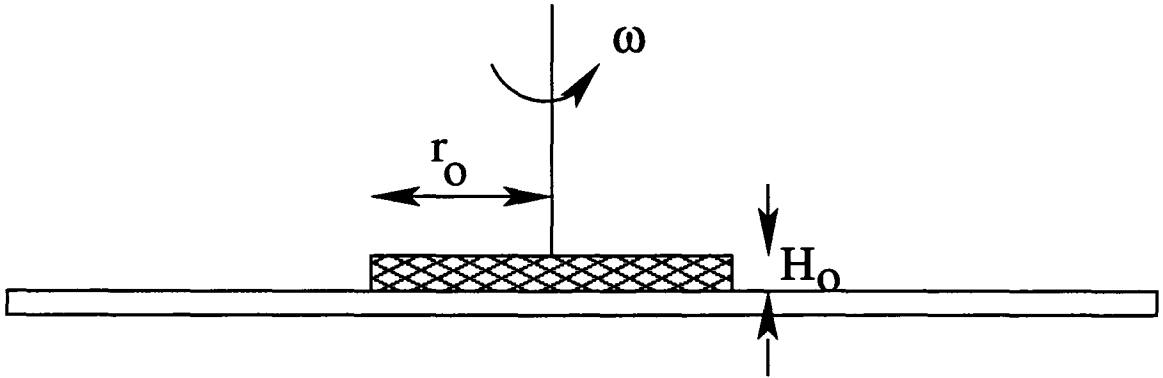


Figure 1.7: A cylindrical volume of fluid with initial radius r_o and height H_o on a substrate. The substrate spins with an angular velocity ω .

Consider a cylindrical volume of fluid with initial volume $V = \pi r_o^2 H_o$ located at the center of a rotating substrate and spreading under the action of a centrifugal force as shown in Fig. 1.7. r_o and H_o are the initial radius and height of the fluid volume, respectively. Cylindrical coordinates will be used in the analysis. We will make the approximation that the drop maintains its cylindrical shape as it spreads. The height of the drop as it spreads is denoted by H . The centrifugal force per unit volume on a small fluid element is given by $\rho\omega^2 r$ where ρ is the fluid density, ω is the angular speed, and r is the radial coordinate of the fluid element. Away from the contact line surface tension is unimportant and the centrifugal force per unit volume is balanced by the viscous force acting on the fluid element, $-\eta\partial^2 v/\partial z^2$ where v is

the fluid velocity and z is the vertical coordinate, so

$$-\eta \frac{\partial^2 v}{\partial z^2} = \rho \omega^2 r. \quad (1.21)$$

This equation is subject to the boundary conditions that $v = 0$ when $z = 0$ and $\partial v / \partial z = 0$ when $z = H$. Integrating Eq. (1.21) over z twice with these boundary conditions gives

$$v = \frac{1}{\eta} \left(-\frac{1}{2} \rho \omega^2 r z^2 + \rho \omega^2 r H z \right). \quad (1.22)$$

The equation of continuity is

$$\frac{\partial H}{\partial t} = -\frac{1}{r} \frac{\partial (r q_r)}{\partial r} \quad (1.23)$$

where q_r is the radial flow per unit length of circumference, $q_r = \int_0^H v dz$. Substituting Eq. (1.22) for v and integrating gives

$$q_r = \frac{\rho \omega^2 r H^3}{3\eta}. \quad (1.24)$$

Putting the above expression for q_r into the equation of continuity (Eq. (1.23)) gives

$$\frac{\partial H}{\partial t} = -\frac{\rho \omega^2}{3\eta} \frac{1}{r} \frac{\partial}{\partial r} (r^2 H^3). \quad (1.25)$$

If we define $K = \rho \omega^2 / 3\eta$ and perform the differentiation on the right-hand side of Eq. (1.25), we get

$$-2KH^3 = \frac{\partial H}{\partial t} + 3K r H^2 \frac{\partial H}{\partial r}. \quad (1.26)$$

However, we can also use the chain rule to write

$$\frac{dH}{dt} = \frac{\partial H}{\partial t} + \frac{\partial H}{\partial r} \frac{dr}{dt}. \quad (1.27)$$

Comparing Eqs. (1.26) and (1.27), we can obtain an ordinary differential equation for H :

$$\frac{dH}{dt} = -2KH^3 \quad (1.28)$$

Integrating this equation gives the solution for H as a function of time

$$H = \frac{H_o}{(1 + 4KH_o^2 t)^{1/2}}. \quad (1.29)$$

Conservation of volume allows us to say that $\pi r^2 H = V$. Substituting Eq. (1.29) into this expression gives

$$r^2 = \frac{V}{\pi} \frac{(1 + 4KH_o^2 t)^{1/2}}{H_o}. \quad (1.30)$$

If we now introduce the scaling $r^* = r/r_o$, $h^* = H/H_o$, and $t^* = t/t_o \approx \eta/H_o^2 \rho \omega^2$ [6], Eq. (1.30) can be written as

$$r^* = \left(1 + \frac{4}{3}t^*\right)^{1/4}. \quad (1.31)$$

The radius of the fluid drop, then, is expected to be proportional to $t^{1/4}$ for $t^* \gg 1$.

Linear Stability

Troian et al. first investigated the linear stability of the flow of fluid down an inclined plane [48]. As will be discussed later, the results of this stability analysis are also applicable to the flow of fluid spreading due to a centrifugal force. Other groups have since worked on the stability problem for spinning drops [55, 62, 63, 64, 65]. The

following is a review of the work of Troian et al. [48].

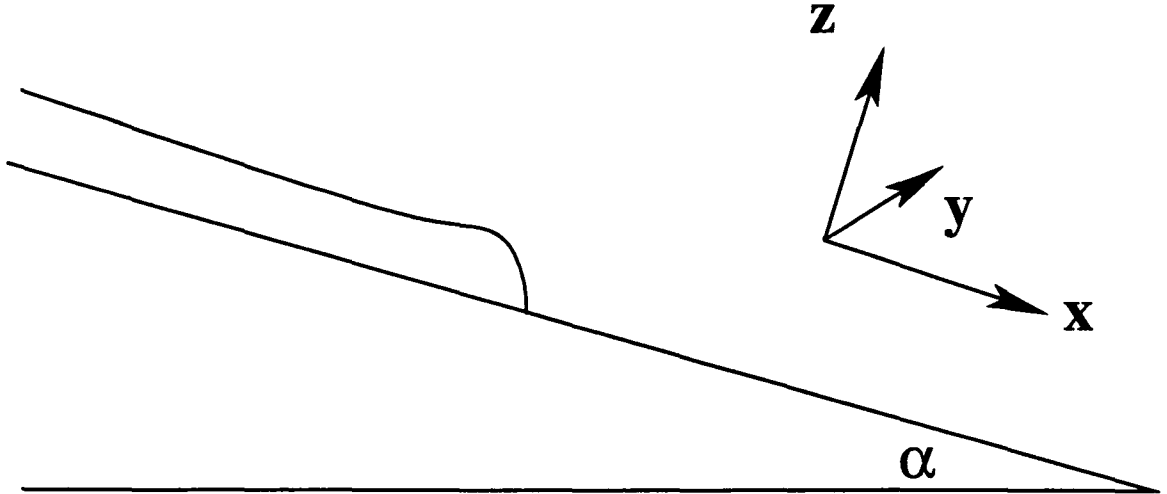


Figure 1.8: A schematic diagram of flow down an inclined plane. The coordinate system used in the linear stability analysis of Troian et al. [48] is shown.

Figure 1.8 is a diagram showing the contact line at the front of a sheet of fluid flowing down an inclined plane. The coordinate system used in the analysis is shown, with x being the downslope direction, y the cross-stream direction, and z the normal to the plane. Troian et al. [48] make use of the lubrication approximation, or thin film approximation, in their linear stability analysis. In this approximation, the thickness of the film H is taken to be much smaller than the characteristic length in the flow direction L , giving $H/L \ll 1$ and simplifying the equations of motion [66]. In a region away from the contact line, equating the viscous force to the gravitational force, gives the height H of the fluid as

$$H = (\eta/\rho g \sin \alpha)^{1/2} x^{1/2} t^{-1/2}, \quad (1.32)$$

where η is the viscosity, ρ is the density, g is the acceleration due to gravity, α is the angle the incline makes with the horizontal as shown in Fig. 1.8, and t is the time. This profile stops at $x = x_n$ with a height at this point of $H = H_n$.

The solution for H near the contact line is more complicated and must include the effects of surface tension. They match the solution near the contact line with a thin film at $x = x_n$ to alleviate the singularity which would otherwise occur there due to the no-slip $v = 0$ boundary condition at the substrate. This thin precursor film has a thickness aH_n . Using the scalings $\xi = x/l$ and $h(\xi, t) = H(x, y, t)/H_n(t)$, Troian et al. derived a partial differential equation for height. They found

$$h_o^2(1 - h_{o\xi\xi\xi}) = \frac{1 - a^3}{1 - a} - (1 + a)\frac{a}{h}. \quad (1.33)$$

A moving coordinate system where the origin coincides with the contact line is used here. $l = H(3Ca)^{-1/3}$ is the capillary length over which surface tension and gravity are the same order of magnitude. Ca is the capillary number given by $\eta U_o/\sigma$ where U_o is the velocity of the contact line and σ is the surface tension. This is a quasi-steady solution where $h(\xi, t) = h_o(\xi)$. Troian et al. solved this equation numerically and showed that near the contact line there is a region of maximum height corresponding to a ridge or a build-up of fluid, as shown in Fig. 1.9. Away from this region, $h_o \rightarrow 1$.

Troian et al. then studied the stability of this solution to small perturbations [48]. They introduced perturbations of the contact line from its position at $\xi = 0$ to $\xi = \xi_B(\zeta, t)$ where ζ is the scaled y coordinate, y/l . The position of the perturbed interface can be written as $\xi(\zeta, t) = -A(\zeta)B(t)$. If $\partial B/\partial t > 0$, the initial perturbations grow, indicating that the contact line is unstable. Solving the problem numerically, they find that the contact line is unstable for dimensionless wavenumbers $q \leq 0.9$ with the most unstable mode being at $q \approx 0.45$. Here q is defined by $q = Ql$ where Q is the dimensional wavenumber. This gives the wavelength of the most unstable mode as $\lambda = 2\pi/Q \approx 14l$.

These results also apply to the contact line when fluid flows due to a centrifugal

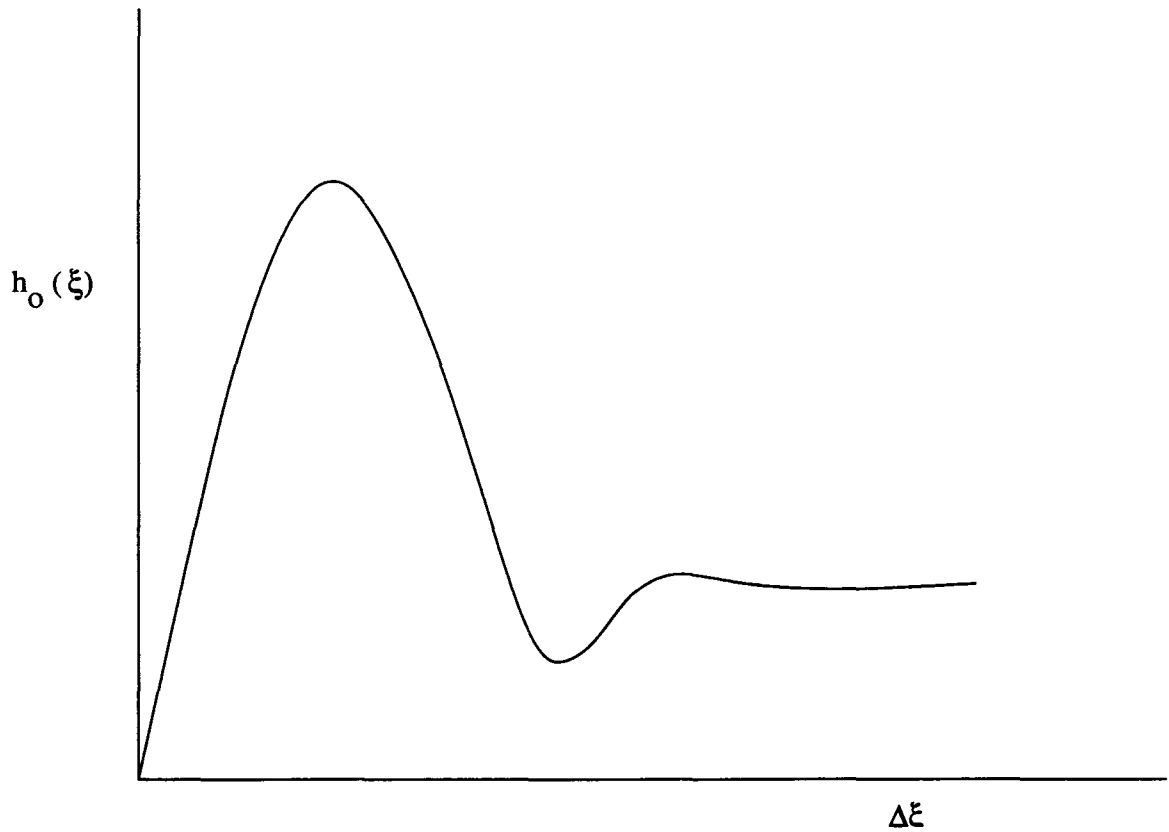


Figure 1.9: A sketch of the solution to Eq. (1.33).

force. In this case, instead of a balance between viscous and gravity forces, there is a balance between viscous and centrifugal forces that results in an equation for H away from the contact line. In both cases, surface tension becomes important near the contact line. Instead of flow in the x direction, as in the case of flow down an incline, flow in the radial direction is studied, with $x_n(t)$ above replaced by the radius $r(t)$ of the fluid drop. Experimental studies [5, 6, 53] have found results that agree well with the above predictions.

1.4.2 Previous work on spin coating of yield stress fluids

Tabuteau et al. [67] studied spincoating using commercial hair gel and Carbopol, a polymer gel which will be described in more detail below. Both of these are yield stress fluids. Although they observed a fingering instability in their experiments, their research focused mainly on the spreading of the fluids prior to fingering. They investigated the effect of different substrate surfaces, angular accelerations, yield stress, and initial radius.

Jenekhe and Schuldt numerically investigated spincoating using the Bingham and Herschel-Bulkley models for a yield-stress fluid [68]. They found that initially uniform films decreased in height due to spinning and that the resultant films were nonuniform in thickness with a maximum in height at the center. Qualitative experiments with a silver-filled polyvinyl acetate in ethyl acetate showed height profiles similar to the numerical predictions. Burgess and Wilson [69] studied the spincoating of a yield stress fluid numerically using a biviscosity model. They also found that the resultant films were non-uniform in height. Tsamopoulos et al. [70] numerically investigated the spincoating of a viscoplastic fluid. They used a model in which the viscosity of the material varied continuously with strain rate with no discontinuities. They studied the effect of the Bingham number, Reynolds number, capillary number, and the gravitational Bond number on the flow. They found that, overall, a viscoplastic fluid needs to be spun for longer than a Newtonian fluid to achieve a uniform film.

Carbopol

The spincoating experiments discussed in Chapter 6 were performed using Carbopol, a commonly used model yield stress fluid. This section provides a more detailed description of Carbopol than appears in Chapter 6.

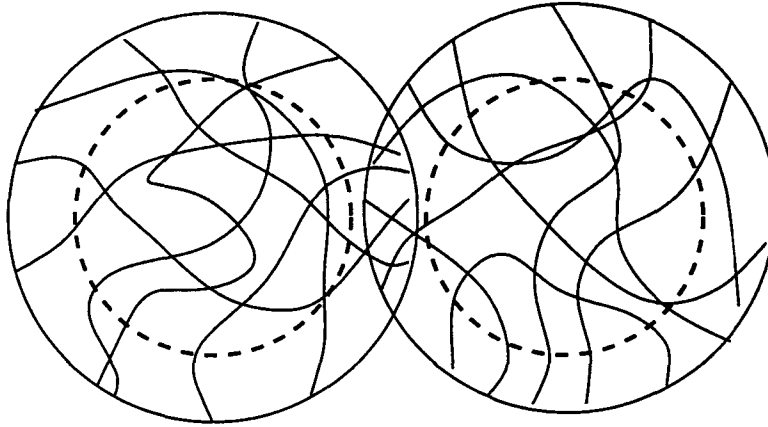


Figure 1.10: Two adjacent microgel particles. Within the dashed circle is the interior of the microgel in which there are many crosslinks between polymer strands. Dangling ends of polymer molecules on the exterior of the microgel particles interact with surrounding particles.

Carbopol is a polymer consisting of CHO_2 monomers [71, 72]. In its dry, powdered state the polymer molecules are coiled, but with the addition of water, the molecules partly straighten. The solution is initially very acidic. A base, in our case NaOH, is added to raise the pH, which causes the material to thicken. A pH of 6.5-7 maximizes the viscosity [71]. On a microscopic level, the polymer molecules form microgel particles. Polymer chains extending out of the microgel particles interact with neighbouring particles [73]. Macroscopically, Carbopol is a clear gel whose thickness depends on the Carbopol concentration. Rheological measurements show that Carbopol has a yield stress and is well described by a Hershel-Bulkley model (Eq. (1.19)) [73].

1.5 Outline

This thesis presents the results of experimental and numerical work on a variety of fingering instabilities. In Chapter 3, details of viscous fingering experiments done

using a single fluid, glycerine, are presented and some numerical results on the same system are briefly discussed. We find that a fingering instability only occurs for high enough inlet pressures and high enough values of the viscosity ratio. We show that, for small cell widths, the dimensionless wavelength of the instability λ/b is a constant. This dependence is not observed in the numerical simulations where only a slight increase in λ with b is seen. This chapter has been published in the Canadian Journal of Physics as Ref. [74] and is reproduced here with permission. Chapter 4 presents the numerical simulations in more detail. In addition to calculations of the wavelength, we present numerical results for the growth rate of the fingers and compare these with experimentally observed growth rates. This chapter has been published as Ref. [75] and is reproduced here with permission. Chapter 5 describes results of spin coating experiments using a Newtonian fluid, silicone oil. We present results on the spreading of the fluid drop, the number of fingers which form and the growth rate of the instability. We show that the spreading of the fluid drop (radius versus time) prior to fingering agrees with theory [59] and that our results for the number of fingers and the growth rate agree with the predictions of lubrication theory [6, 8]. This chapter has been submitted for publication in Physical Review E [76]. In Chapter 6, the results of spincoating experiments with a non-Newtonian fluid, Carbopol, are presented. This chapter will be submitted for publication. Lastly, a summary of the work detailed in the research papers is presented in Chapter 7.

Bibliography

- [1] D. J. Acheson, *Elementary Fluid Dynamics* (Clarendon Press, Oxford, 1995).
- [2] T. E. Faber, *Fluid Dynamics for Physicists* (Cambridge University Press, Cambridge, 1995).
- [3] G. Nicolis, *Introduction to Nonlinear Science* (Cambridge University Press, Cambridge, 1995).
- [4] P.G. Saffman and G. Taylor, *Proc. R. Soc. London A* **245**, 312 (1958).
- [5] F. Melo, J. F. Joanny, and S. Fauve, *Phys. Rev. Lett.* **63**, 1958 (1989).
- [6] N. Fraysse and G. M. Homsy, *Phys. Fluids*, **6**, 1491 (1994).
- [7] H. E. Huppert. *Nature (U.K.)*, **300**, 427 (1982).
- [8] S. M. Troian, X. L. Wu, and S. A. Safran, *Phys. Rev. Lett.* **27**, 1496 (1989).
- [9] S. M. Troian, E. Herbolzheimer, and S. A. Safran, *Phys. Rev. Lett.* **65**, 333 (1990).
- [10] P. Habdas, M. J. Case, and J. R. de Bruyn, *Phys. Rev. E* **63**, 066305 (2001).
- [11] J. R. de Bruyn, *Phys. Rev. Lett.* **74**, 4843 (1995).
- [12] J. A. Whitehead and K. R. Helfrich, *J. Geophys. Res.* **96B**, 4145 (1991).

- [13] K. R. Helfrich, *J. Fluid Mech.* **305**, 219 (1995).
- [14] J. J. Wylie and J. R. Lister, *J. Fluid Mech.* **305**, 239 (1995).
- [15] S. J. S. Morris, *J. Fluid Mech.* **308**, 111 (1996).
- [16] J. J. Wylie, K. R. Helfrich, B. Dade, J. R. Lister, and J. F. Salzig, *Bull. Volcanol.* **60**, 432 (1999).
- [17] L. W. Lake, *Enhanced Oil Recovery* (Prentice-Hall, Englewood Cliffs, 1989).
- [18] K. V. McCloud and J. V. Maher, *Phys. Rep.* **260**, 139 (1995).
- [19] G. M. Homsy, *Annu. Rev. Fluid Mech.* **19**, 271 (1987).
- [20] D. A. Kessler, J. Koplik, and H. Levine, *Adv. Physics* **37**, 255 (1988).
- [21] C.-W. Park, S. Gorell, and G. M. Homsy, *J. Fluid Mech.* **141**, 275 (1984).
- [22] T. Maxworthy, *Phys. Rev. A* **39**, 5863 (1989).
- [23] R. A. Wooding, *J. Fluid Mech.* **39**, 477 (1969).
- [24] L. Paterson, *Phys. Fluids* **28**, 26 (1985).
- [25] C. T. Tan and G. M. Homsy, *Phys. Fluids* **29**, 3549 (1986).
- [26] C. T. Tan and G. M. Homsy, *Phys. Fluids* **31**, 1330 (1988).
- [27] W. B. Zimmerman and G. M. Homsy, *Phys. Fluids A* **4**, 1901 (1992).
- [28] O. Manickam and G. M. Homsy, *J. Fluid Mech.* **288**, 75 (1995).
- [29] C-W. Park and G. W. Homsy, *J. Fluid Mech.* **139**, 291 (1984).
- [30] Y. C. Yortsos and M. Zeybeck, *Phys. Fluids* **31**, 3511 (1988).

- [31] Z. Yang and Y. C. Yortsos, *Phys. Fluids* **9**, 286 (1997).
- [32] C. T. Tan and G. M. Homsy, *Phys. Fluids* **4**, 1099 (1992).
- [33] W. B. Zimmerman and G. M. Homsy, *Phys. Fluids* **4**, 2348 (1992).
- [34] O. Manickam and G. M. Homsy, *Phys. Fluids* **6**, 95 (1994).
- [35] N. Rakotomalala, D. Salin, and P. Watzky, *J. Fluid Mech.* **338**, 277 (1997).
- [36] C.-Y. Chen and E. Meiburg, *J. Fluid. Mech.* **326**, 57 (1996).
- [37] G. M. Homsy, private communication.
- [38] D. Snyder and S. Tait, *J. Fluid Mech.* **369**, 1 (1998).
- [39] E. Lajeunesse, J. Martin, N. Rakotomalala, and D. Salin, *Phys. Rev. Lett.* **79**, 5254 (1997).
- [40] E. Lajeunesse, J. Martin, N. Rakotomalala, D. Salin, and Y. C. Yortsos, *J. Fluid Mech.* **398**, 299 (1999).
- [41] E. Lajeunesse, J. Martin, N. Rakotomalala, D. Salin, and Y. C. Yortsos, *Phys. Fluids* **13**, 799 (2001).
- [42] P. Petitjeans and T. Maxworthy, *J. Fluid. Mech.* **326**, 37 (1996).
- [43] J.-C. Bacri, N. Rakotomalala, D. Salin, and R. Wouméni, *Phys. Fluids* **A4**, 1611 (1992).
- [44] J. Fernandez, P. Kurowski, P. Petitjeans, and E. Meiburg, *J. Fluid Mech.* **451**, 239 (2002).

- [45] J. Fernandez, P. Kurowski, L. Limat, and P. Petitjeans, *Phys. Fluids* **13**, 3120 (2001).
- [46] R. L. Chouke, P. van Meurs, C. van der Poel, *Trans. AIME* **216**, 188 (1959).
- [47] TDK, <http://www.tdk.com/procommon/press/article.asp?site=prorecid=115>.
- [48] S. M. Troian, E. Herbolzheimer, S. A. Safran and J. F. Joanny, *Europhys. Lett.* **10**, 25 (1989).
- [49] L. W. Schwartz, *Phys. Fluids A*, **1**, 443 (1989).
- [50] J. R. de Bruyn, *Phys. Rev. A*, **46**, 4500 (1992).
- [51] J. M. Jerrett and J. R. de Bruyn, *Phys. Fluids A*, **4**, 234 (1992).
- [52] J. R. de Bruyn, P. Habdas, and S. Kim, *Phys. Rev. E*, **66**, 031504 (2002).
- [53] M. A. Spaid and G. M. Homsy, *Phys. Fluids*, **4**, 823 (1997).
- [54] M. A. Spaid and G. M. Homsy, *Phys. Fluids*, **8**, 460 (1996).
- [55] M. A. Spaid and G. M. Homsy, *J. Non-Newtonian Fluid Mech.* **55**, 249 (1994).
- [56] I. Veretennikov, A. Agarwal, A. Indeikina, and H.-C. Chang, *J. Colloid Interface Sci.* **215**, 425 (1999).
- [57] M.-W. Wang and F.-C. Chou, *J. Electrochem. Soc.* **148**, 283 (2001).
- [58] S. Togashi, T. Ohta, and H. Azuma, *J. Chem. Eng. Jpn.* **34**, 1402 (2001).
- [59] A. G. Emslie, F. T. Bonner and L. G. Peck, *J. App. Phys.* **29**, 858 (1957).
- [60] S. K. Wilson, R. Hunt, and B. R. Duffy, *J. Fluid Mech.* **413**, 65 (2000).

- [61] Y. D. Shikhmurzaev, *Phys. Fluids*. **9**, 266 (1997).
- [62] I. S. McKinley, S. K. Wilson, and B. R. Duffy, *Phys. Fluids*, **11**, 30 (1999).
- [63] I. S. McKinley and S. K. Wilson, *Phys. Fluids*, **13**, 872 (2001).
- [64] I. S. McKinley and S. K. Wilson, *Phys. Fluids*, **14**, 133 (2002).
- [65] L. W. Schwartz and R. V. Roy, *Phys. Fluids*, **16**, 569 (2004).
- [66] S. B. G. O'Brien and L. W. Schwartz, *Encyclopedia of Surface and Colloid Science*, 5283 (2002).
- [67] H. Tabuteau, J. C. Baudez, and P. Coussot, to be published.
- [68] S. A. Jenekhe and S. B. Schuldt, *Chem. Eng. Commun.* **33**, 135 (1985).
- [69] S. L. Burgess and S. D. R. Wilson, *Phys. Fluids*, **8**, 2291 (1996).
- [70] J. A. Tsamopoulos, M. F. Chen, and A. Borkar, *Rheol. Acta.* **35**, 597 (1996).
- [71] Neutralizing Carbopol and Pemulen Polymers in Aqueous and Hydroalcoholic Systems, Tech. Rep. TDS-237, Noveon (2002).
- [72] Probing the Microstructure of Yield-Stress Fluids using Multiple Particle Tracking, F. K. Oppong, Master's thesis, Memorial University of Newfoundland, 2005.
- [73] G. P. Roberts and H. A. Barnes, *Rheol. Acta.* **40**, 499 (2001).
- [74] K. E. Holloway and J. R. de Bruyn, *Can. J. Phys.* **83**, 551 (2005).
- [75] K. E. Holloway and J. R. de Bruyn, *Can. J. Phys.* **84**, 273 (2006).
- [76] K. E. Holloway, P. Habdas, N. Semsarillar, K. Burfitt, and J. R. de Bruyn, submitted to *Phys. Rev. E*.

[77] Fluent Inc. FLUENT Version 6.1.22 [computer program]. Fluent Inc., Lebanon, N.H. 2004.

Chapter 2

Co-authorship Statement

This co-authorship statement will address my contributions to the papers in Chapters 3-6.

2.1 Chapters 3: Viscous fingering with a single fluid; authors: K. E. Holloway and J. R. de Bruyn

Both my supervisor, Dr. John de Bruyn, and myself were responsible for the identification of the research topic. The conceptual idea for the experimental apparatus described in “Viscous fingering with a single fluid” was due to Dr. de Bruyn. I prepared the detailed design and drew the plans which the machine shop used to manufacture the apparatus, with input from Dr. de Bruyn. I performed all the experiments described in the paper.

The simulations described in “Viscous fingering with a single fluid” and “Numerical simulations of a viscous fingering instability in a fluid with a temperature-

dependent viscosity” were done using the commercial software, Fluent. While it was Dr. de Bruyn’s idea to use Fluent for simulations initially, the motivation behind extending them as far as we did was largely mine. I created the model used in the simulations. Eric Thornhill, a researcher at the National Research Council, provided many helpful discussions as I was learning to use Fluent and assistance with designing the numerical grid used in the simulations. I performed all the simulations described in the paper and subsequently analysed and interpreted the experimental and numerical data; Dr. de Bruyn assisted with devising the methods used to do the analysis and with interpreting the results of the data analysis.

I wrote the first draft of the manuscript. Dr. de Bruyn provided comments and suggestions for revision, which we incorporated into the final manuscripts.

2.2 Chapter 4: Numerical simulations of a viscous fingering instability in a fluid with a temperature-dependent viscosity; authors: K. E. Holloway and J. R. de Bruyn

The work described in this paper is an extension to the numerical work described in Chapter 3. I performed all the simulations and the data analysis and interpretation discussed in the paper. Dr. de Bruyn again assisted with the data analysis method and the interpretation of results.

I wrote the first draft of the paper. Dr. de Bruyn assisted with the editing and made suggestions for changes which we incorporated into the final manuscript.

2.3 Chapter 5: Spreading and fingering during spin coating; authors: K. E. Holloway, P. Habdas, N. Semsarillar, K. Burfitt, and J. R. de Bruyn

My supervisor, Dr. John de Bruyn, was responsible for the identification of the research topic. The experimental apparatus used for this research had previously been designed by P. Habdas and an undergraduate Engineering co-op student, N. Semsarilar, assembled and tested it. K. Burfitt did preliminary experiments. Dr. de Bruyn and I assembled the optical system described in this chapter. I performed all the experiments described in this paper and the subsequent data analysis, although Dr. de Bruyn assisted with determining the method used to do the analysis. Both Dr. de Bruyn and I were involved in interpreting the results.

I wrote the first draft of the manuscript. Dr. de Bruyn provided comments and suggestions for revision, which we incorporated into the final manuscript.

2.4 Chapter 6: Fingering in a yield-stress fluid during spin coating; authors: K. E. Holloway, H. Tabuteau, and J. R. de Bruyn

My supervisor, Dr. John de Bruyn, was responsible for the identification of the research topic. My preliminary experiments with Carbopol helped to shape what, in particular, the research focused on.

The Carbopol samples were made and the rheological measurements performed by Hervé Tabuteau, a post-doctoral fellow at the University of Western Ontario. I

performed all the spin coating experiments described in this paper and the subsequent data analysis. Both Dr. de Bruyn and I were involved in interpreting the results.

I wrote the first draft of the manuscript, with the exception of the sections describing of the sample preparation and rheological methods. Dr. de Bruyn provided comments and suggestions for revision, which I incorporated into the final manuscript.

Chapter 3

Viscous fingering with a single fluid

3.1 Abstract

We study fingering that occurs when hot glycerine displaces cooler, more viscous glycerine in a radial Hele-Shaw cell. We find that fingering occurs for a large enough initial viscosity contrast and for high enough flow rates of the displacing fluid. The wavelength of the fingering instability is proportional to the cell width for thin cells but the ratio of wavelength to cell width decreases for our thickest cell. Similar fingering is seen in numerical simulations of this system.

3.2 Introduction

The displacement of one fluid by another is a surprisingly rich and complex process with important applications in many fields [1, 2, 3, 4]. In particular, displacement in a Hele-Shaw cell — a thin layer of fluid confined between two parallel plates — models the corresponding flows in porous media, which are important in oil recovery [5]. When a less-viscous fluid displaces a more-viscous fluid, the interface between

them can become unstable and fingers of the less-viscous fluid will form and penetrate into the more-viscous fluid. This is known as viscous fingering. Previous experimental and theoretical work on viscous fingering [6] has involved two different fluids, miscible or immiscible, with different viscosities. In this paper, we present the results of experiments using a single fluid — glycerine — the viscosity of which depends strongly on temperature. Hot, less viscous glycerine at a temperature T_h is injected into a horizontally-oriented radial Hele-Shaw cell which is held at a lower temperature T_c and contains cold, more viscous glycerine. We observe a fingering instability for a range of experimental conditions.

Viscous fingering between two immiscible fluids confined between the plates of a Hele-Shaw cell has been studied extensively [1, 2, 3, 4, 7, 8]. In this case, there is a well-defined interface between the two fluids and surface tension acts to stabilize the interface at high wave number k . If the cell is horizontal (so that gravity is unimportant) the Saffman-Taylor [1] fingering instability will always occur when the less-viscous fluid displaces the more-viscous fluid, that is, when the viscosity ratio $M = \mu_1/\mu_2 > 1$. Here μ_1 and μ_2 are the viscosities of the displaced and displacing fluids, respectively. A linear stability analysis based on two-dimensional equations obtained by averaging over the gap width [1, 9] shows that there exists a particular mode with wavelength proportional to $b/Ca^{1/2}$ which has the highest linear growth rate and dominates the fingering pattern at early times. Here b is the cell width, that is, the spacing between the top and bottom plates of the Hele-Shaw cell, and the capillary number Ca is a measure of the ratio of viscous forces to surface tension. This wavelength is only observed experimentally for low Ca (high surface tension), however [7, 8], while at high Ca the wavelength becomes simply proportional to the cell width b [8].

Fingering between miscible fluids in a Hele-Shaw cell can also occur, although

this situation is less well-studied than the immiscible case [2, 10, 11, 12, 13, 14, 15]. There is no surface tension and no true interface between the two miscible fluids, but rather a gradient in concentration across the interfacial region which broadens with time due to diffusion. The dimensionless quantity which characterizes the flow is the Peclet number $Pe = \ell v/D$, where ℓ is a characteristic length scale of the flow, v a characteristic velocity, and D the diffusion coefficient; Pe is a measure of the importance of convective transport relative to diffusion.

The linear stability analysis of the fingering instability for miscible displacements is more subtle than in the immiscible case, since dispersion makes the base state time-dependent [12]. A straightforward application of the theory for the immiscible case with zero surface tension [11] indicates that the growth rate of perturbations increases with k without bound, which is physically unreasonable. Tan and Homsy [12] performed a careful linear stability analysis of miscible displacement in a porous medium, taking into account the effect of dispersion. When the injected fluid was less viscous than the displaced fluid ($M > 1$), fingering occurred. They found a cutoff wave number above which perturbations were damped by dispersion, and a most unstable wave number proportional to the mobility ratio of the two fluids. While dispersion normally stabilizes the flow at high wavenumber, Yortsos and Zeybek have shown that dispersion can also be destabilizing under certain conditions [16]. Yang and Yortsos [17] have also studied miscible displacements theoretically, and lattice gas simulations of miscible displacements have been carried out by Rakotomalala et al. [18].

Thermoviscous fingering — flow instability in a fluid with a strongly temperature-dependent viscosity flowing between cold, isothermal walls — has been studied theoretically by several groups [19, 20, 21, 22, 23], and some experimental results have been reported [19, 23]. This work has primarily been done in the context of magma

flow through fissures in the earth's crust. In the instability discussed in these papers [19, 20, 21, 22, 23] fingers develop in a flowing fluid which is in a thermal steady state. As discussed further below, this is not the situation we study: here the system is not in a thermal steady state and the fingers we see are closely related to those seen in experiments on miscible displacement.

Miscible displacement driven by an applied pressure has been studied experimentally by Paterson in a radial Hele-Shaw cell [11]. He found the wavelength λ of the instability to be approximately $4b$. Similar results were found by Snyder and Tait for rectilinear flow [25]. Miscible displacements in capillary tubes have been studied experimentally [26] and numerically [27], and miscible displacement in a three-dimensional porous medium has been studied experimentally using an acoustic technique [28]. Experiments on miscible displacement in a vertical Hele-Shaw cell have been carried out by Lajeunesse et al. [29, 30, 31]; they found the wavelength of the instability to be $\lambda = (5 \pm 1)b$. They also found both a critical flow velocity and a critical viscosity ratio M_c below which fingering did not occur. A theoretical analysis of their system gave $M_c = 3/2$ [31]. This agreed well with their experimental results as well as with the results of Snyder and Tait [25], who found $M_c = 3/2$ in the absence of gravity. The configuration studied by Lajeunesse et al. [29, 30, 31] was gravitationally stable and the displacement was driven by an applied pressure. Gravity-driven miscible displacements have been studied by Wooding [10] and more recently by Fernandez et al. [32], who found the pattern wavelength λ to scale as the reciprocal of the Rayleigh number Ra (which is the relevant parameter for their system) for low Ra , while λ was proportional to b at large Ra . Fernandez et al. [33] found similar behavior for the wavelength from a theoretical description in terms of a modified Brinkmann equation. A stability analysis of the three-dimensional Stokes equations by Graf et al. confirmed this behavior [34], and showed that at large Ra

the flow became significantly three-dimensional so that averaging across the gap was no longer valid.

The system we study here – hot glycerine forced into colder glycerine in a Hele-Shaw cell – is similar in many ways to miscible displacement involving two different fluids, with temperature replacing concentration, viscosity being a function of temperature, and thermal diffusion replacing molecular diffusion. There is again no true interface between the displaced and displacing fluids, rather there is a temperature gradient that is initially sharp but spreads with time due to thermal diffusion. There is, however, at least one significant difference between our system and two-fluid miscible displacement. If the surfaces of our cell were adiabatic, then the temperature of the injected fluid would not change as it flowed through the cell and heat transfer would only occur by thermal diffusion between the hot and cold fluids. This is, of course, not the case — the injected fluid loses heat to the upper and lower surfaces of the cell and cools considerably, with a corresponding increase in viscosity, as it moves through the cell. In mathematical terms, the boundary conditions at the top and bottom plates are not the same as they are in isothermal miscible displacement involving two fluids. This must be taken into account in the interpretation of our experimental results, as discussed below.

Our experimental apparatus and procedure are described in Sect. 3.3 and the results are presented in Sect. 3.4. In Sect. 3.5 our simulations are described and the results are presented. In Sect. 3.6 we discuss our results in the context of other work on miscible displacement.

3.3 Experiment

The apparatus used for the experiments is shown schematically in Fig. 4.1. The experimental fluid is contained in a horizontal Hele-Shaw cell defined by two horizontal plates separated by a small gap. The upper plate is a 10 cm diameter sapphire window, while the lower plate is aluminum. These plate materials were chosen due to their high thermal conductivity, in an effort to achieve isothermal boundary conditions. The plates are clamped together around six spacers positioned towards the outer edge of the cell. These spacers determine the width of the gap b . For this work we used $b = 0.5, 1, \text{ and } 2$ mm. The perimeter of the cell is open to the atmosphere except in the regions occupied by the spacers, so the pressure at the edge of the cell is equal to atmospheric pressure. The upper and lower surfaces of the cell are maintained at a temperature T_c by a temperature-controlled mixture of water and ethylene glycol antifreeze which circulates above and below the cell. T_c is measured by a thermistor located in the temperature-controlled fluid just below the lower surface of the cell. The cell is filled with glycerine before each run.

A cylindrical reservoir containing more glycerine is located below the cell. The fluid in this reservoir is heated to a temperature T_h , where $T_h > T_c$, by a second temperature-controlled water-antifreeze mixture which circulates through a jacket surrounding the cylinder. For the experiments reported here, T_h is maintained at 343.15 K (70°C). The glycerine in the reservoir is dyed black with nigrosin dye to distinguish it from the glycerine initially in the cell and to allow visualization of the flow.

The hot fluid in the reservoir can be forced into the cell through a short length of capillary tubing by pressurizing the piston shown in Fig. 4.1. The pressure on the piston is monitored with a transducer attached to the pressure line. The dyed

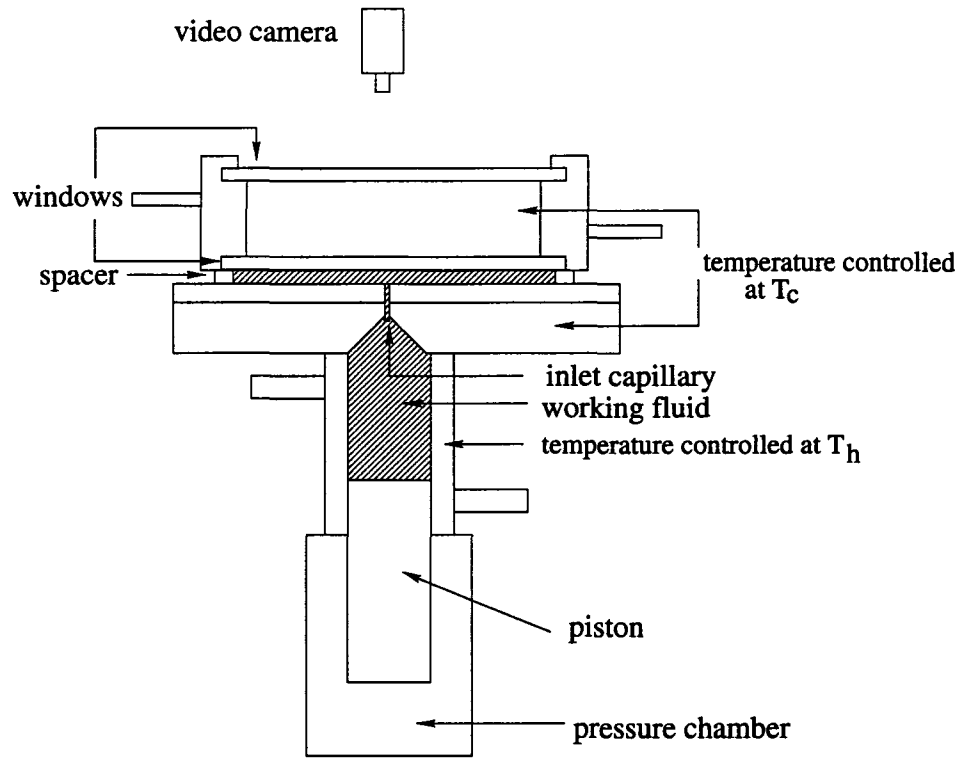


Figure 3.1: The experimental apparatus used in the fingering experiments. Glycerine is confined between the upper and lower surfaces of the cell and within the cylinder below the cell (the shaded areas in the figure). The glycerine in the cell is maintained at a temperature T_c while the glycerine in the cylinder is dyed black and maintained at a higher temperature T_h . The piston is used to force the hot glycerine into the cell. The flow is visualized by a video camera mounted above the apparatus.

glycerine enters the cell through a small hole drilled in the bottom plate, then spreads out radially, displacing the colder, more viscous glycerine. The flow is monitored with a video camera mounted above the cell and interfaced to a computer.

The viscosity μ of glycerine is a strong function of temperature. We measured $\mu(T)$ using a falling-ball viscosimeter over the temperature range $273.4 \text{ K} \leq T \leq 368.1 \text{ K}$. The viscosity data were well described by the function

$$\mu = \exp(a_0 + a_1T + a_2T^2) \quad (3.1)$$

where μ is the viscosity in kg/ms, T is the temperature in K, and the fit parameters are $a_0 = 77.9671$, $a_1 = -0.43983$, and $a_2 = 5.97562 \times 10^{-4}$.

3.4 Results

Figure 4.6 shows a sequence of images obtained from a run of the experiment with cell width $b = 1 \text{ mm}$. The hotter, dyed glycerine enters the cell at the center of the bottom plate and spreads radially as it displaces the surrounding colder, clear glycerine. Fingers have begun to develop by the time of Fig. 4.6(b) and grow as time progresses. Although the fingers are not perfectly uniform, they do have a characteristic width or wavelength λ , as is the case for radial fingering with distinct immiscible or miscible fluids. Tip splitting is observed in the later stages of the flow, as can be seen at the top left of Fig. 4.6(d). λ was determined by directly measuring the width of fingers from the images at the time when they first become visible, and averaging over all fingers in an image. The radial position r in the cell at which fingers first became visible did not vary systematically with either P or T_c . Although there was substantial scatter from run to run, on average we found $r = 0.80 \pm 0.28$,

1.3 ± 0.5 , and 1.3 ± 0.3 cm for $b = 0.5$, 1, and 2 mm respectively.

Figure 3.3 shows images from runs with $b = 0.5$ mm, 1 mm, and 2 mm. The images indicate that λ increases with b . On the other hand, we find that λ is independent of flow rate (i.e., driving pressure P) and viscosity contrast (i.e., cell temperature T_c) within the accuracy of our measurements. In Fig. 3.4(a) we plot λ as a function of T_c for several runs (with different values of P) for all three values of b , while Fig. 3.4(b) shows λ as a function of P . The average wavelengths of λ for the three cell widths are shown as dotted lines in both plots, with standard deviations indicated by the error bars at the left of the plots. While the increase in λ with b is evident, there is no systematic variation of λ with either T_c or P .

If we express λ in units of the cell width b we find $\lambda/b = (5.8 \pm 0.8)$, (5.3 ± 0.7) , and (3.7 ± 0.5) for $b = 0.5$ mm, 1 mm, and 2 mm respectively. λ/b is plotted as a function of b in the inset to Fig. 3.4(b). The values are equal within our uncertainty for the two thinner cells, but λ/b is significantly smaller for the thickest cell. These values of λ/b are consistent with the results of other fingering experiments involving two miscible fluids: Paterson[11] found $\lambda \approx 4b$ for miscible fingering in a radial geometry, while Lajeunesse et al.[29] found $\lambda = (5 \pm 1)b$ for miscible fingering in a vertically oriented Hele-Shaw cell.

The wavelength for $b = 1$ mm was also determined by using an edge detection algorithm to locate the perimeter of the dark injected fluid in the recorded images. The dominant angular wave number of the pattern was then determined from a Fourier transform of the perimeter as a function of angular position. Again, we find that the wavelength of the fingers when they are first detectable is independent of both the driving pressure and the initial viscosity ratio. With this technique we find $\lambda/b = 4.8 \pm 0.8$ for $b = 1$ mm. This value is a slightly lower than that found by direct measurement, possibly because the fingers can be detected earlier with this technique

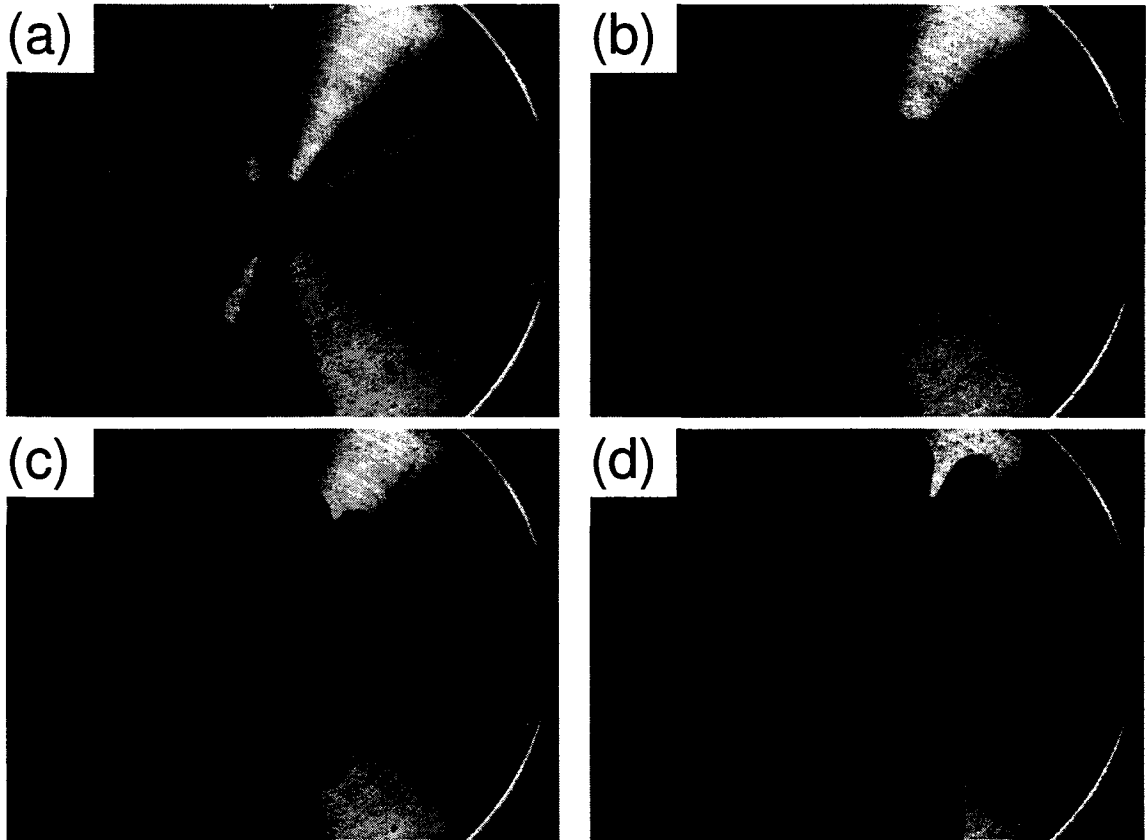


Figure 3.2: A sequence of images from a run of the experiment with $b = 1$ mm, $P = 74.8$ kPa, $T_c = 284.48$ K, and $T_h = 343.15$ K. The images were recorded at times (a) 0.33 s, (b) 0.75 s, (c) 0.92 s, and (d) 1.17 s after the start of the experiment. The field of view is 8.8 cm.

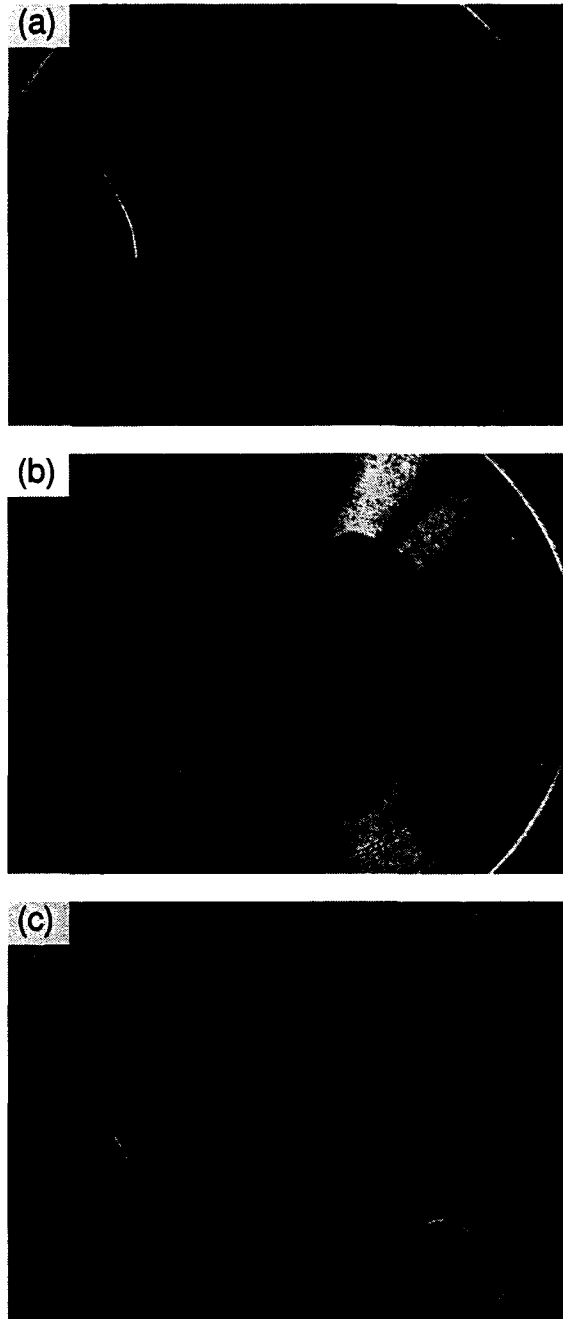


Figure 3.3: Images from runs of the experiment with different cell widths b . For all three runs $T_h = 343.15$ K. (a) $b = 0.5$ mm, $P = 189.6$ kPa, $T_c = 275.77$ K, (b) $b = 1$ mm, $P = 67.2$ kPa, $T_c = 277.94$ K and (c) $b = 2$ mm, $P = 76.4$ kPa, $T_c = 280.07$ K. Note the increase in finger width with increasing b .

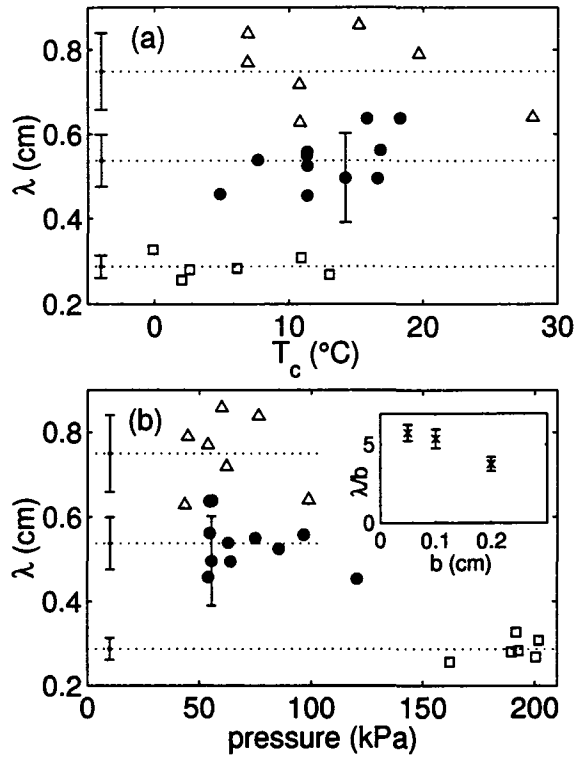


Figure 3.4: (a) Wavelength of the finger pattern as a function of cell temperature T_c . All runs plotted had $T_h = 343.15$ K but P varied from run to run. Wavelengths are determined by averaging over all fingers in the pattern; a typical standard deviation is shown for one point. Open squares: $b = 0.5$ mm, solid circles: $b = 1$ mm, open triangles: $b = 2$ mm. The dotted lines show the mean wavelength for each cell width, while the standard deviation is indicated by the error bars at the left of the graph. (b) Same as (a), but plotted as a function of driving pressure P . The inset shows the mean wavelength scaled by the cell width as a function of b .

than by eye. Attempts to use the same technique on experimental images from the other cell widths were not completely successful.

The growth rate σ of the fingers can be determined by plotting the amplitude of the dominant peak in the Fourier transform of the perimeter, as in Fig. 4.13. The amplitude of the peak (which is proportional to the length of the fingers) grows exponentially at early times, then flattens out at later times as nonlinear effects become important. We find growth rates in the range $3.0 \text{ s}^{-1} \leq \sigma \leq 15.0 \text{ s}^{-1}$ for $b = 1 \text{ mm}$; within our uncertainties the growth rate does not vary systematically with the initial viscosity ratio, but it does appear to decrease as the driving pressure increases.

Figure 3.6 shows the range of applied pressures and viscosity ratios for which fingering occurred for $b = 1 \text{ mm}$. The solid circles indicate points for which the fingering instability was observed. We emphasize that the viscosity ratio plotted here is the ratio of the viscosities of the hot and cold fluids at injection, which we refer to as m , and not the ratio at the location of the instability, M . The dashed line is a guide to the eye which indicates the stability boundary above which fingering occurs and below which the system is stable. Fingers are not observed for low flow rates or low initial viscosity ratios. Similar stability diagrams are obtained for $b = 0.5 \text{ mm}$ and $b = 2 \text{ mm}$, but the boundaries of the fingering regime vary with b : the low-pressure cut-off is higher for the smallest value of b , while the viscosity ratio boundary moves to lower m as b increases. The initial viscosity ratios below which fingering was not observed were approximately 30, 20, and 10 for $b = 0.5, 1, \text{ and } 2 \text{ mm}$ respectively, while the corresponding low-pressure cut-offs were approximately 170, 40, and 40 kPa.

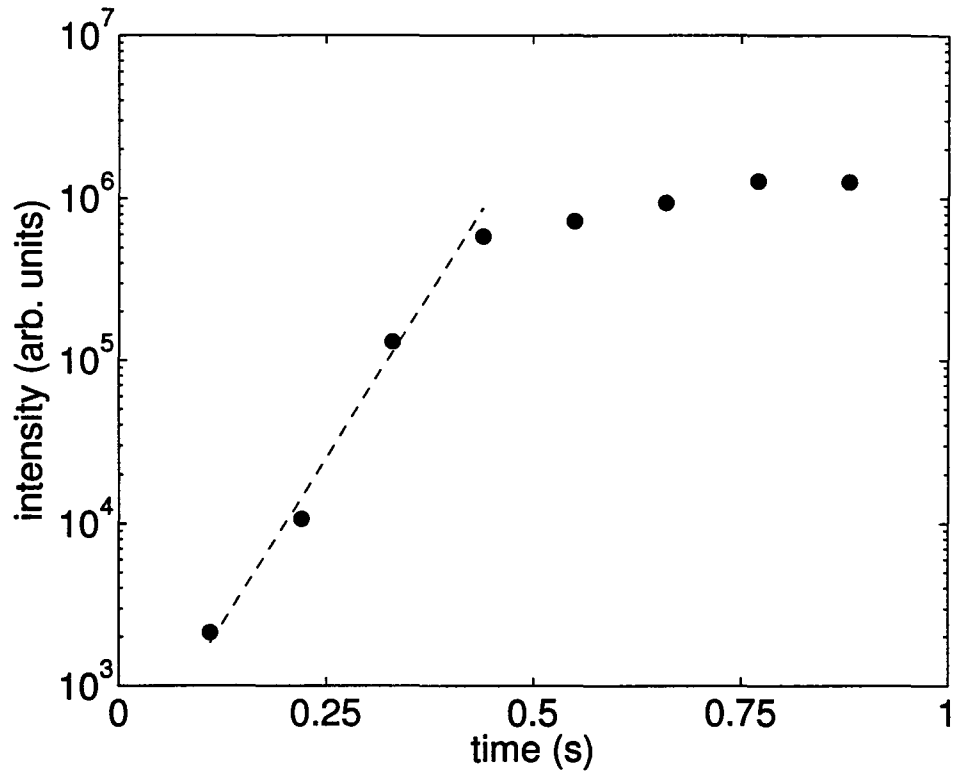


Figure 3.5: The intensity of the dominant peak in the Fourier spectrum of the boundary between injected and displaced fluid as a function of time for an experimental run with $T_c = 280.81$ K, $T_h = 343.15$ C, $P = 62.7$ kPa, and $b = 1$ mm. At early times, the intensity increases exponentially. The dashed line is a fit to the data at early times; its slope gives the exponential growth rate of the fingers.

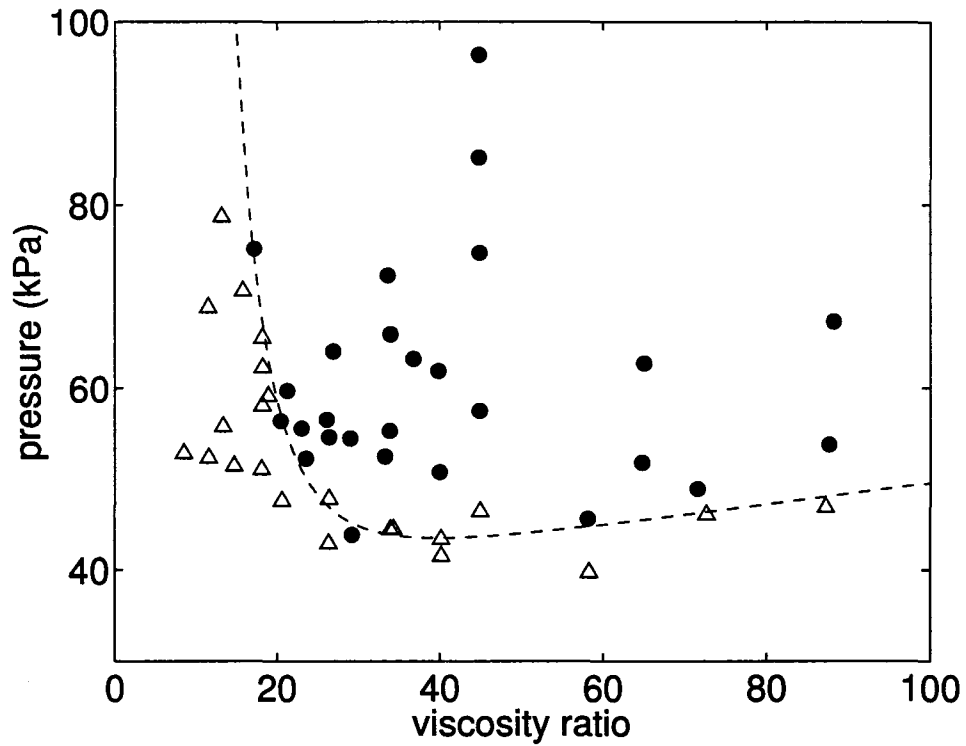


Figure 3.6: The measured stability diagram for $b = 1$ mm. The abscissa is the *initial* viscosity ratio m . The solid circles indicate conditions for which fingers were observed, while the open triangles show points for which fingering was not observed. The dashed line is a guide to the eye indicating the approximate location of the boundary above which the fingering instability occurs.

3.5 Simulations

We model our experimental system using Fluent [35], a computational fluid dynamics software package. The simulations are fully three-dimensional with the cell geometry and dimensions set to match the experimental cell, that is, two parallel plates separated by a small gap, b , with a circular inlet in the middle of the bottom plate. For the simulations described in this paper, the temperature of the incoming glycerine was fixed at $T_h = 343.15$ K, as in the experiments, while the velocity v_i of the incoming glycerine was varied between simulations. The upper and lower surfaces of the cell were held at a constant temperature, $T_c < T_h$, which was varied between simulations. The temperature dependence of the viscosity of glycerine was calculated using Eq. (3.1). No-slip boundary conditions were applied at the upper and lower surfaces of the cell, while the perimeter of the cell was open, i.e., the fluid was allowed to flow out of the outer edge of the cell. The flow of the hot glycerine into the colder glycerine was calculated as a function of time [36].

Figure 3.7 shows a sequence of images from a simulation with $b = 1$ mm. The images show the temperature in the horizontal plane midway between the plates. Comparison of Figs. 3.7 and 4.6 shows good qualitative agreement between the simulations and the experimental results. The hot glycerine (white in the figure) spreads radially and penetrates into the surrounding colder glycerine (black). The boundary between hot and cold fluid is initially smooth, but approximately periodic fingers appear and grow after some time.

The wavelength λ of the instability for the simulations was determined using the image analysis technique described above. Averaging over all the runs for which λ was calculated gives $\lambda/b = 4.0 \pm 1.0$, 2.6 ± 0.3 , and 2.3 ± 0.3 for $b = 0.5$, 1 and 2 mm respectively. These values are all somewhat smaller than the corresponding values

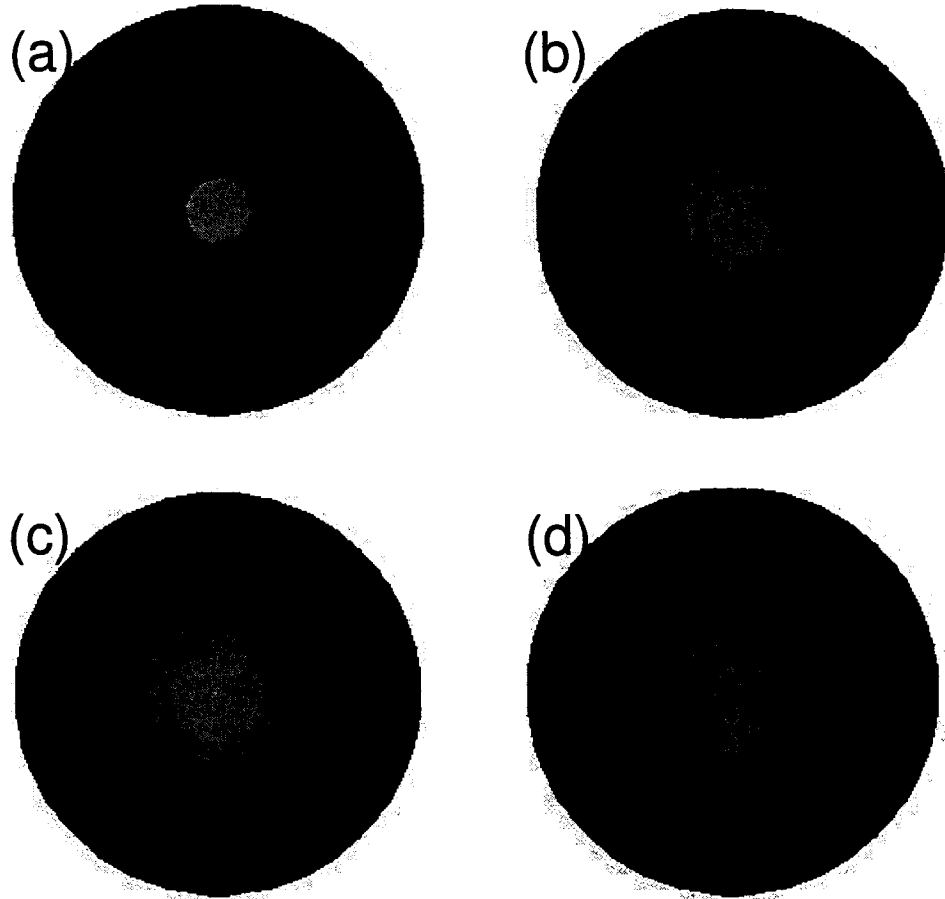


Figure 3.7: A time sequence of images from a simulation of the displacement of cold glycerine by injected hot glycerine. The gray scale represents temperature, with white being hot and black, cold. These images show the temperature at the midplane of the cell for $T_c = 278.15$ K, $T_h = 343.15$ K, $b = 1$ mm, and inlet velocity $v_i = 2$ m/s. The images are at times (a) 0.02 s, (b) 0.06 s, (c) 0.1 s, (d) 0.18 s.

obtained by direct measurement of the fingers in the experiments, and λ/b decreases steadily with increasing b .

The values of inlet velocity and initial viscosity ratio for which the instability was observed in the simulations with $b = 1$ mm are shown in Fig. 3.8(a). There is again reasonable agreement between the simulations and the experiments — there are critical values of the viscosity ratio and inlet velocity below which fingers are not observed, just as in the experimental results shown in Fig. 3.6. From Fig. 3.8(a), m_c is estimated to be approximately 20, in agreement with the experimental value. Simulations in which we attempted to impose a constant pressure inlet condition (as in the experiments) rather than a constant inlet flow velocity did not give physical results. It is possible, however, to extract the calculated inlet pressure from the constant inlet velocity simulations. The inlet pressure decreases substantially over the course of the run as the flow impedance of the cell decreases. Fig. 3.8(b) shows the range of existence of the fingering instability for the 1 mm simulations in terms of the initial viscosity contrast and the inlet pressure at a time (the earliest time at which the flow was calculated) of 0.001 s. The low pressure cut-off inferred from this diagram is on the order of 12 kPa, about 30% of the experimental result.

The value of the critical viscosity ratio determined here is again the viscosity ratio at the start of the simulation, i.e., at injection. The hot glycerine loses heat as it moves through the cell, so the viscosity ratio at the location of the instability will be significantly lower. We can obtain an estimate of the viscosity ratio at the location of the instability from our simulations. From the image analysis described above, we can determine the time at which the instability occurs — that is, the time at which the dominant peak in the Fourier spectrum starts to grow. At this time, we find the viscosity of the glycerine on both sides of the apparent interface. For simulations with m in the range $34.9 < m < 121.7$, we find $7.5 < M < 13$, a factor of 5 to 10 smaller.

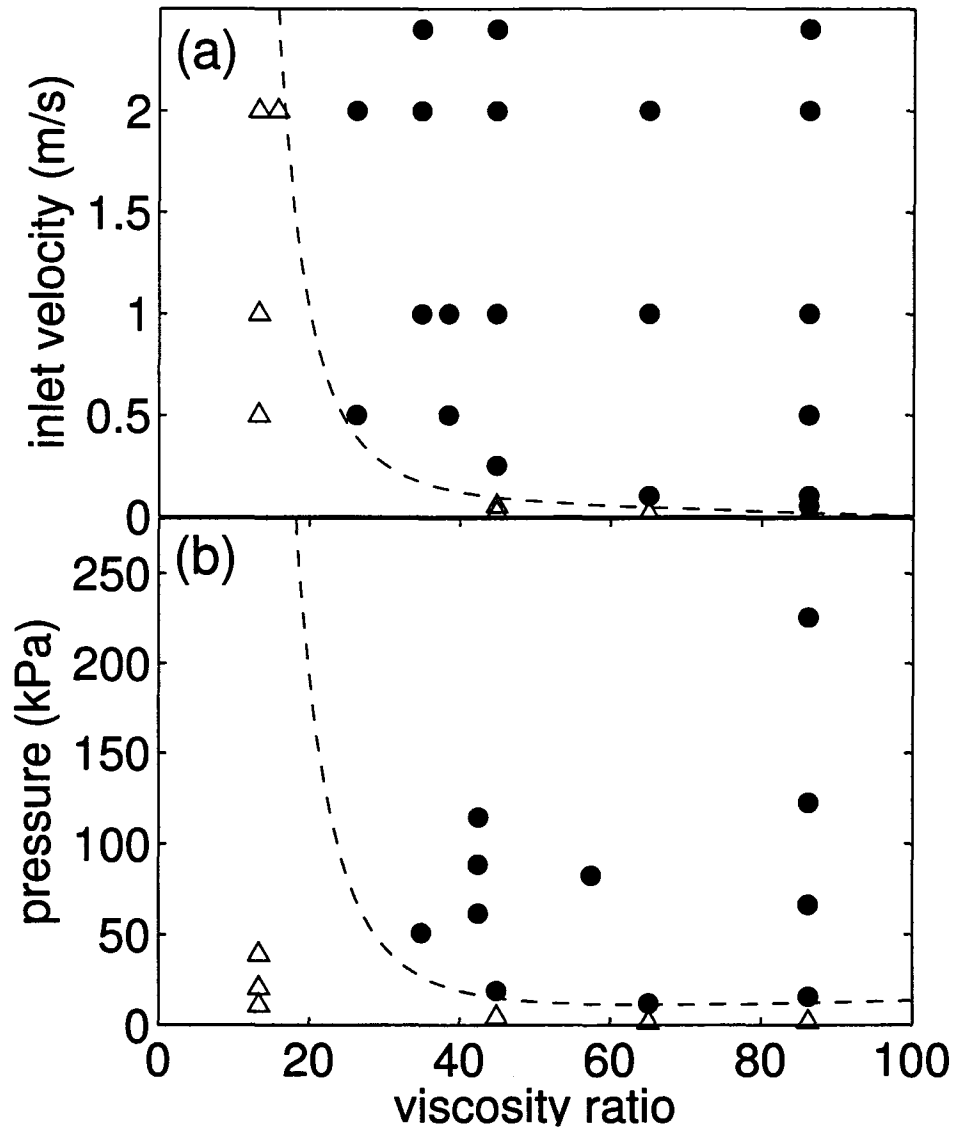


Figure 3.8: (a) The stability diagram determined from simulations with $b = 1$ mm. The symbols are as in Fig. 3.6. Here the ordinate is the injection velocity of the hot glycerine, which was the quantity controlled in the simulations. The dashed line is a guide to the eye. (b) The same data plotted in terms of the initial pressure at the inlet to the cell.

3.6 Discussion

We do not observe fingering when the initial viscosity ratio is smaller than a critical value, m_c . From experiments, we find $m_c \approx 30, 20,$ and 10 for $b = 0.5, 1,$ and 2 mm respectively, while the simulations give $m_c = 20$ for $b = 1$ mm. These values are substantially higher than the critical viscosity ratio $M_c = 1.5$ observed in isothermal miscible fingering experiments [29, 31]. However, as noted above, m is the ratio of viscosities of the fluids at injection. The injected fluid is initially at temperature T_h , but it cools as it flows through the cell. As a result the viscosity of the injected fluid increases and so the ratio of viscosities at the location of the instability will be substantially smaller than the initial ratio m . The simulation results indicate that M_c is in fact on the order of 10 , but this is still substantially larger than the previous results [29, 31].

Fingering also does not occur when the driving pressure P is below a certain value — roughly 50 kPa in Fig. 3.6. The instability occurs at approximately the same radial position regardless of experimental conditions, as discussed above. At low P , the flow is slow and the injected fluid cools so much that the viscosity contrast has vanished by the time it reaches the position r where the instability would normally occur. This results in the low-pressure cut-off seen in Fig. 3.6. The same reasoning can be applied to the low velocity cut-off observed in the simulations.

Experimentally, we found the pattern wavelength to depend only on the cell width b , with $\lambda/b = (5.6 \pm 0.8)$ being the average of the values for the two thinner cells studied. For the 2 mm cell we found $\lambda/b = (3.7 \pm 0.5)$, significantly smaller than for the thinner cells.

Based on previous studies of viscous fingering and related instabilities, [7, 8, 32, 33, 34] we expect a wavelength proportional to $1/Pe$ for small Pe , and proportional

to b for large Pe . Since in our case it is thermal diffusion that is relevant, it is the thermal Peclet number,

$$Pe = \ell v / \kappa, \quad (3.2)$$

that is relevant. Here κ is the thermal diffusivity. Using Darcy's law for flow in a Hele-Shaw cell,

$$v = -\frac{b^2}{12\mu} \nabla P. \quad (3.3)$$

We take μ here to be μ_1 , the viscosity of the displaced fluid. We approximate $\nabla P \approx -P/R$, where R is the radius of our experimental cell. With R as the characteristic length scale ℓ , we get

$$Pe \approx \frac{b^2 P}{12\mu_1 \kappa}. \quad (3.4)$$

For the conditions of our experiments, we find $3.6 \times 10^3 \leq Pe \leq 4.8 \times 10^7$, with most runs in the range $10^4 < Pe < 10^5$. Thus our experiments are all in the high- Pe regime.

Previous experiments on other miscible displacements at high values of Pe (or the equivalent dimensionless quantity) found the constant of proportionality to be of order 5 [11, 29, 30, 31, 32], and our results for the 0.5 mm and 1 mm cells are consistent with this. We obtain a lower constant of proportionality for the 2 mm cell. An obvious explanation for the difference would be the presence of three-dimensional effects in the thicker cell. However recent numerical work has shown that the crossover between the low- and high- Pe regimes results from three-dimensional effects which make the Hele-Shaw approximation invalid in the high Pe regime [34]. Our own simulations also show significant three-dimensional effects for all three cell thicknesses [36]. Thus we expect that the flow in our experiments is already three-dimensional, even in the thin cells, although presumably it could be more so in the thicker cell.

Despite the qualitative similarity in the phenomena observed, the simulations give values of λ/b which decrease with increasing b , and which are all somewhat lower than the experimental values. It may be that for some reason three-dimensional effects are more pronounced in the numerical simulations than in the experiments, and that this leads to a decrease in λ/b . This would be consistent with the invocation of three-dimensional effects to explain the decrease in λ/b for the thicker experimental cell. The differences may also be due in part to the fact that it is easier to detect the fingers at an early stage in the simulations due to the much lower noise level in the analyzed images.

A significant difference between the simulations and the experiments is that in the former the fluid was injected with a constant inlet velocity, while in the latter it was injected at approximately constant pressure. Attempts to use a constant pressure boundary condition in the simulations were unsuccessful, and the calculated inlet pressure in the simulations does vary considerably over the course of a run. Another difference is in the thermal boundary conditions at the cell walls. The walls of the experimental cell are kept cold by circulating coolant and because of their finite thermal conductivity will be subject to small temperature changes during an experimental run. In contrast, the walls of the computational cell are held at a fixed temperature.

Our system is similar to that in which thermoviscous fingering [19, 20, 21, 22, 23] is expected to occur in some respects, but there are important differences which make it clear that the fingering we observe is not due to the thermoviscous instability [24]. The initial condition in our case is such that hot glycerine encounters cold glycerine immediately upon entering the cell, so there is initially a large gradient in temperature between the hot and cold fluids. This leads to the formation of Saffman-Taylor-like fingers which preclude any possible later growth of thermoviscous fingers. In addition,

our system is not in a thermal steady state while the hot injected fluid penetrates into the cell, and we would have to wait several thermal diffusion times, $t_k = b^2/4\kappa$, to reach the steady state and for thermoviscous fingers to develop [21, 24]. With b equal to 1 mm and $\kappa \approx 10^{-7}$ m²/s, $t_k \approx 2.5$ s. In the runs in which we observe an instability, the fluid reaches the edge of the cell and the experiment is over in a time less than or on the order of this time scale.

Although there is no true surface tension between two miscible fluids, the concentration gradient across the interfacial region can give rise to a stress which acts as an effective surface tension [37, 38]. This is particularly significant when the interface is sharp, before it is smoothed by diffusion. Similarly, the temperature gradient in our system can lead to an effective surface tension which will be largest at early times. Our estimates of the magnitude of this effect suggest that it is several orders of magnitude too small to play a role in selecting the wavelength of the instability we have studied here.

3.7 Conclusion

We have performed experiments on miscible viscous fingering in a radial Hele-Shaw cell using a single fluid — glycerine — with a strongly temperature-dependent viscosity. All of our experiments are in the high Peclet number regime. Fingering occurred for large enough temperature difference between the injected and displaced fluid, and for high enough flow rates. We found the wavelength of the fingering pattern to depend only on the cell thickness, with $\lambda/b = (5.6 \pm 0.8)$ being the average value for our two thinner cells. λ/b was lower for our thickest cell ($b = 2$ mm), perhaps due to increased three-dimensionality of the flow. These results are consistent with wavelengths found in related experiments on fingering in miscible displacements.

Our simulations showed a fingering instability similar to that seen in the experiments. We found that the stability curves for the experiment and the simulations follow the same trend, that is, a critical viscosity ratio and critical inlet velocity necessary for fingering to occur. Our results also show that the wavelength depends only on the cell thickness, with $\lambda/b = 4.0 \pm 1.0$, 2.6 ± 0.3 , and 2.3 ± 0.3 for the 0.5, 1, and 2 mm cells respectively. The decrease in λ/b with increasing cell thickness may be due to the same effect as in the experiments. The simulations also allow us to estimate the critical viscosity ratio at the location of the instability, M_c , which is on the order of 10, much lower than the value of the initial viscosity ratio but higher than the value found in previous miscible fingering experiments.

Acknowledgments

We acknowledge helpful discussions with G. M. Homsy, J. Wylie, Y. Yortsos, and E. Thornhill. This research was supported by the Natural Sciences and Engineering Research Council of Canada and in part by an Atlantic Accord Career Development award.

Bibliography

- [1] P.G. Saffman and G. Taylor, Proc. R. Soc. London A **245**, 312 (1958).
- [2] G. M. Homsy, Annu. Rev. Fluid Mech. **19**, 271 (1987).
- [3] D. A. Kessler, J. Koplik, and H. Levine, Adv. Physics **37**, 255 (1988).
- [4] K. V. McCloud and J. V. Maher, Phys. Rep. **260**, 139 (1995).
- [5] L. W. Lake, Enhanced Oil Recovery (Prentice-Hall, Englewood Cliffs, 1989).
- [6] See for example Refs. [2, 3, 4] for reviews.
- [7] C.-W. Park, S. Gorell, and G. M. Homsy, J. Fluid Mech. **141**, 275 (1984).
- [8] T. Maxworthy, Phys. Rev. A **39**, 5863 (1989).
- [9] T. E. Faber, Fluid Dynamics for Physicists (Cambridge University Press, Cambridge, 1995).
- [10] R. A. Wooding, J. Fluid Mech. **39**, 477 (1969).
- [11] L. Paterson, Phys. Fluids **28**, 26 (1985).
- [12] C. T. Tan and G. M. Homsy, Phys. Fluids **29**, 3549 (1986).
- [13] C. T. Tan and G. M. Homsy, Phys. Fluids **31**, 1330 (1988).

- [14] W. B. Zimmerman and G. M. Homsy, *Phys. Fluids A* **4**, 1901 (1992).
- [15] O. Manickam and G. M. Homsy, *J. Fluid Mech.* **288**, 75 (1995).
- [16] Y. C. Yortsos and M. Zeybeck, *Phys. Fluids* **31**, 3511 (1988).
- [17] Z. Yang and Y. C. Yortsos, *Phys. Fluids* **9**, 286 (1997).
- [18] N. Rakotomalala, D. Salin, and P. Watzky, *J. Fluid Mech.* **338**, 277 (1997).
- [19] J. A. Whitehead and K. R. Helfrich, *J. Geophys. Res.* **96B**, 4145 (1991).
- [20] K. R. Helfrich, *J. Fluid Mech.* **305**, 219 (1995).
- [21] J. J. Wylie and J. R. Lister, *J. Fluid Mech.* **305**, 239 (1995).
- [22] S. J. S. Morris, *J. Fluid Mech.* **308**, 111 (1996).
- [23] J. J. Wylie, K. R. Helfrich, B. Dade, J. R. Lister, and J. F. Salzig, *Bull. Volcanol.* **60**, 432 (1999).
- [24] J. J. Wylie, private communication.
- [25] D. Snyder and S. Tait, *J. Fluid Mech.* **369**, 1 (1998).
- [26] P. Petitjeans and T. Maxworthy, *J. Fluid. Mech.* **326**, 37 (1996).
- [27] C.-Y. Chen and E. Meiburg, *J. Fluid. Mech.* **326**, 57 (1996).
- [28] J.-C. Bacri, N. Rakotomalala, D. Salin, and R. Wouméni, *Phys. Fluids A***4**, 1611 (1992).
- [29] E. Lajeunesse, J. Martin, N. Rakotomalala, and D. Salin, *Phys. Rev. Lett.* **79**, 5254 (1997).

- [30] E. Lajeunesse, J. Martin, N. Rakotomalala, D. Salin, and Y. C. Yortsos, *J. Fluid Mech.* **398**, 299 (1999).
- [31] E. Lajeunesse, J. Martin, N. Rakotomalala, D. Salin, and Y. C. Yortsos, *Phys. Fluids* **13**, 799 (2001).
- [32] J. Fernandez, P. Kurowski, P. Petitjeans, and E. Meiburg, *J. Fluid Mech.* **451**, 239 (2002).
- [33] J. Fernandez, P. Kurowski, L. Limat, and P. Petitjeans, *Phys. Fluids* **13**, 3120 (2001).
- [34] F. Graf, E. Meiburg, and C. Härtel, *J. Fluid Mech.* **451**, 261 (2002).
- [35] Fluent, Inc., Lebanon, NH USA. <http://www.fluent.com>
- [36] K. E. Holloway and J. R. de Bruyn, unpublished.
- [37] P. Petitjeans, *C. R. Acad. Sci. Paris* **322**, Series II b, 673 (1996).
- [38] D. D. Joseph, *Eur. J. Mech. B/Fluids* **9**, 565 (1990).

Chapter 4

Numerical simulations of a viscous fingering instability in a fluid with a temperature-dependent viscosity

4.1 Abstract

We have performed numerical simulations of the flow of hot glycerine as it displaces colder, more viscous glycerine in a radial Hele-Shaw cell. We find that fingering occurs for sufficiently high inlet velocities and viscosity ratios. The wavelength of the instability is independent of inlet velocity and viscosity ratio, but depends weakly on cell width. The growth rate of the fingers is found to increase with inlet velocity and decrease with the cell width. We compare our results with those from experiments.

4.2 Introduction

Viscous fingering is an interesting and important phenomenon that results when a viscous fluid is displaced by another, less viscous fluid [1]. Due to the viscosity

contrast between the fluids, the interface between them can become unstable and fingers of the less viscous fluid penetrate into the more viscous fluid. This instability has important applications in many fields, including the oil recovery process [2], so it is important to understand the conditions under which it occurs. It has previously been studied for both immiscible [1, 3, 4] and miscible [5, 6, 7, 8] fluids. Recently we have performed experiments on viscous fingering in a single fluid with a temperature dependent viscosity [9].

A substantial amount of work exists on fingering between two immiscible fluids in a Hele-Shaw cell, a thin fluid layer bounded by two parallel plates separated by a distance b (see Refs. [3, 4] for reviews). The considerable interest in this geometry is due to the mathematical analogy with flow in a porous medium [1, 3, 4]. A stability analysis of the governing equations shows that in the absence of gravity, the displacement of a more viscous fluid by a less viscous fluid will always result in instability [1, 10]. A well defined interface exists between the two immiscible fluids. This interface is unstable to all perturbations of wave number less than a cut-off wave number. At wave numbers higher than this cut-off, surface tension σ stabilizes the interface. The dimensionless parameter which characterizes the flow is the capillary number $Ca = \sigma/\mu v$, where μ is the viscosity and v a characteristic flow velocity. Ca is a measure of the relative importance of surface tension to viscous forces. For low Ca the wavelength of the instability $\lambda \propto b/Ca^{1/2}$ [11], but for high Ca (low surface tension) λ has been shown to be simply proportional to b [12].

In the case of viscous fingering between miscible fluids (see Ref. [3] for a review), there is not a well defined interface between the fluids but rather an initially sharp change in concentration that broadens with time due to diffusion. In this case Taylor dispersion, that is, the combined effects of molecular diffusion and shear flow, rather than surface tension, provides the high wave number cut-off [3]. Experiments on

miscible viscous fingering have shown that the wavelength λ of the instability is proportional to the cell width b [5, 6]. It has also been found both theoretically and experimentally [6, 7, 8, 13, 14] that the existence of the instability depends on a critical flow rate and critical viscosity ratio M_c being exceeded. The viscosity ratio $M = \mu_1/\mu_2$, where μ_1 and μ_2 are the viscosities of the displaced and displacing fluids respectively.

Recent experiments by Holloway and de Bruyn [9] studied fingering in a single fluid with a strongly temperature-dependent viscosity. Hot, less-viscous glycerine, dyed black for visualization purposes, was injected into colder, more-viscous glycerine contained in a temperature-controlled Hele-Shaw cell. These experiments showed that there was a critical value of the inlet pressure P and a critical value of the viscosity ratio which must be exceeded for the instability to occur. The wavelength of the instability was observed to be proportional to the cell width b for small cell widths. The observed instability was similar to miscible viscous fingering but with some important differences. The injected and displaced fluids were separated by a temperature gradient rather than a gradient in concentration, and diffusion of heat was the stabilizing mechanism instead of molecular diffusion. In addition, the hot glycerine cooled as it flowed through the cell due to heat loss to the cold walls — a situation which has no analog in miscible viscous fingering experiments.

In this paper numerical simulations of the displacement of cold glycerine by hotter, less-viscous glycerine are presented and compared with our previous experiments [9]. The simulations will be described in Section 4.3 and the results presented in Section 4.4. In Section 4.5 the results of the simulations will be compared to the experimental results. Section 4.6 is a brief conclusion.

4.3 Method

4.3.1 Problem Set-up

A sketch of the problem under consideration is shown in Fig. 4.1. We want to model the flow and temperature fields within a fluid contained in the narrow gap of a radial Hele-Shaw cell, the walls of which are maintained at temperature T_c . Hot fluid is injected into the cell through a small hole in the center of the bottom plate and displaces the cold fluid initially present in the cell. The geometry and dimensions of the cell were chosen to match those of the Hele-Shaw cell used in our previous experiments [9]. The cell consists of two circular plates of diameter 10 cm separated by a small gap b , which was varied between simulations. The hole in the center of the lower plate has a diameter of 1.84 mm. The perimeter of the cell is open so that fluid can flow out there. The viscosity of the fluid is temperature dependent as described below. Changes in other fluid parameters due to temperature are expected to be much smaller than the change in viscosity and are neglected.

4.3.2 Numerical Method

We performed our numerical simulations using Fluent [15], a commercial program which solves the equations for conservation of mass, momentum, and energy using a control volume technique [16]. The specific equations solved by Fluent are given in Appendix B. The control volumes here are the cells of the numerical grid shown in Fig. 4.2, which was created using Gambit [17], a Fluent preprocessor. The concentration of control volumes is set to be greater towards the center of the grid to capture the smaller-scale structure of the flow there.

In the control volume technique, the equations are integrated over the control vol-

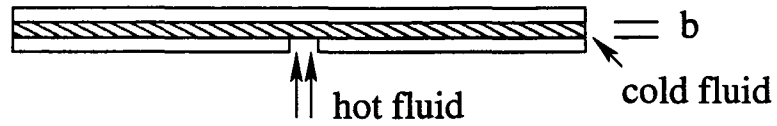


Figure 4.1: A sketch of the problem to be solved. The geometry consists of two circular, parallel walls at a temperature T_c separated by a small gap b . The cell initially contains fluid at temperature T_c . Fluid with $T_h > T_c$ is injected through a small hole in the center of the bottom wall.

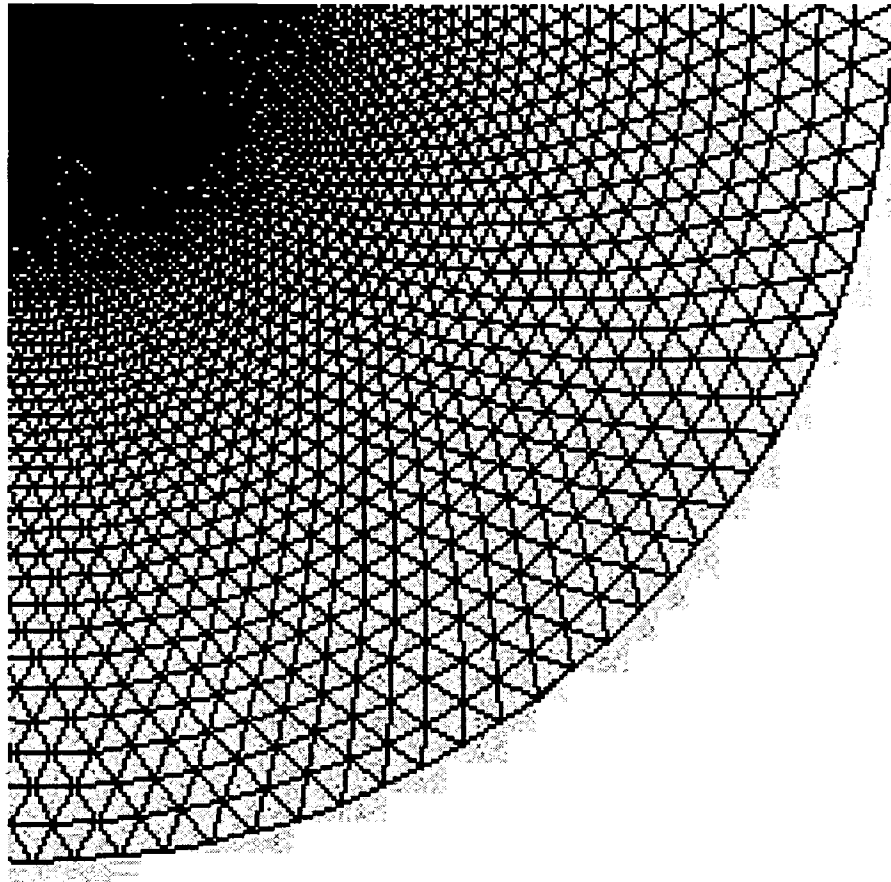


Figure 4.2: A segment of the midplane of the numerical grid used in the simulations. The grid consists of 364520 wedge shaped cells with 10 levels in the vertical direction.

umes, then discretized and linearized to give algebraic equations for the unknowns. A segregated three-dimensional solver is used to find solutions to these equations at each time step. The momentum, continuity, and energy equation are solved sequentially [15, 18]. A first order upwind scheme is used to solve the momentum and energy equations. Details can be found in the Fluent User's Guide [15].

A volume of fluid (VOF) method is used in most of the simulations presented here to track the region separating the hot and cold fluids. The VOF method is typically used for immiscible fluids. To adapt it to our situation, we define the hot and cold glycerine as two separate phases and assign a value of 0 to the surface tension between them [19]. While there is no true interface in this case, there is a region between the two phases where some control volumes contain both hot and cold fluid. The VOF method determines the amount of each phase present in every control volume. The advantage of using the VOF method is the increased information obtained about the boundary between the two phases; the disadvantage is significantly longer computation time. Some of our simulations, particularly those used to produce most of the data for Fig. 4.14 below, did not use this method. The results were the same whether the VOF method was used or not.

4.3.3 Boundary Conditions and Material Parameters

The velocity v_i with which the fluid enters the cell at the inlet hole is specified. The velocity of the fluid in the interior of the cell is initialized to zero. A no-slip boundary condition ($\bar{v} = 0$) is prescribed on the walls of the cell. At the outer edge of the cell, the pressure is set to be equal to the atmospheric pressure. A constant temperature T_c is specified on the cell walls, and the temperature T_h of the injected fluid is also specified. For the simulations reported here, T_h is always set at 343.15 K.

Table 4.1: Values of the material properties of glycerine used in the simulations.

density ρ	1259.9 kg/m ³
specific heat C_p	2427 J/kgK
thermal conductivity α	0.286 W/mK
molecular weight	92.06

The simulations are done for three cell widths: $b = 0.5, 1,$ and 2 mm, corresponding to the widths of the experimental cells [9]. For $b = 0.5$ mm, v_i was chosen to be in the range 0.5 to 1.5 m/s and T_c is set between 275 and 285 K. For $b = 1$ mm, $0.01 \leq v_i \leq 2.5$ m/s and $275 \leq T_c \leq 287$ K, and for $b = 2$ mm, $2 \leq v_i \leq 3.5$ m/s and $265 \leq T_c \leq 280$ K. The range of values of v_i was chosen to include the regime in which an instability was observed.

For the simulations reported in Section 3, both the injected and displaced fluids are glycerine. The viscosity of the glycerine in the simulations was set to have the experimentally measured temperature dependence, which is well described by $\mu = \exp(A_0 + A_1T + A_2T^2)$ where μ is the viscosity in kg/ms, T is the temperature in K, $A_0 = 77.9671$, $A_1 = -0.43983$ and $A_2 = 5.97562 \times 10^{-4}$ [9]. The remaining material parameters for glycerine are taken to be independent of T and are given in Table 4.1.

4.3.4 Grid and Time Step Independence

To determine how the results obtained from our simulations depend on the coarseness of the numerical grid, we performed several runs under identical conditions — chosen to give a fingering instability — but with grids made up of different numbers of grid cells. Fig. 4.3 shows the temperature along a radial line through the midplane of the cell. With the exception of the coarsest grid, the temperature profiles calculated using the different grids agree quite well. The number of fingers which formed in

each case was determined for each run at a time of 0.01 s, as described below. The results, shown in Fig. 4.4(a), indicate that the number of fingers varies from 8 to 11 depending on which grid is used. The two coarsest grids have the fewest fingers. On the basis of these results, and as a compromise between accuracy and computation time and data storage requirements, a grid with 364520 cells was chosen for the calculations presented here. Using this grid, the number of fingers was determined as the size of the time step was varied. As shown in Fig. 4.4(b), the number of fingers is independent of the size of the time step for the time shown. The time step for our simulations was chosen to be 0.0001 s.

4.3.5 Validation

To confirm that Fluent could properly model a fingering instability, we performed several simulations of isothermal miscible displacements. In this case, Saffman-Taylor fingering is expected if the viscosity of the injected fluid is lower than that of the displaced fluid [1, 3, 4]. Fluent has been previously used to study miscible viscous fingering in a rectangular geometry[19], although in that case, the fluids used and the information taken from the simulations were different from what is the case here. We used water with density $\rho = 998.2 \text{ kg/m}^3$ and viscosity $\mu = 0.001003 \text{ kg/ms}$ as the less viscous fluid and glycerine, $\rho = 1259.9 \text{ kg/m}^3$, $\mu = 0.799 \text{ kg/ms}$, as the more viscous fluid. These simulations did not include heat transfer and the VOF method described above was used. Fig. 4.5(a) shows an image from a run in which glycerine was injected into water. Here $b = 1 \text{ mm}$ and $v_i = 2 \text{ m/s}$. The grayscale in the image shows the volume fraction of glycerine in each numerical cell, with white indicating pure glycerine and black indicating water. In this case the interface between the two fluids is stable, as expected when a more viscous fluid is injected into a less viscous

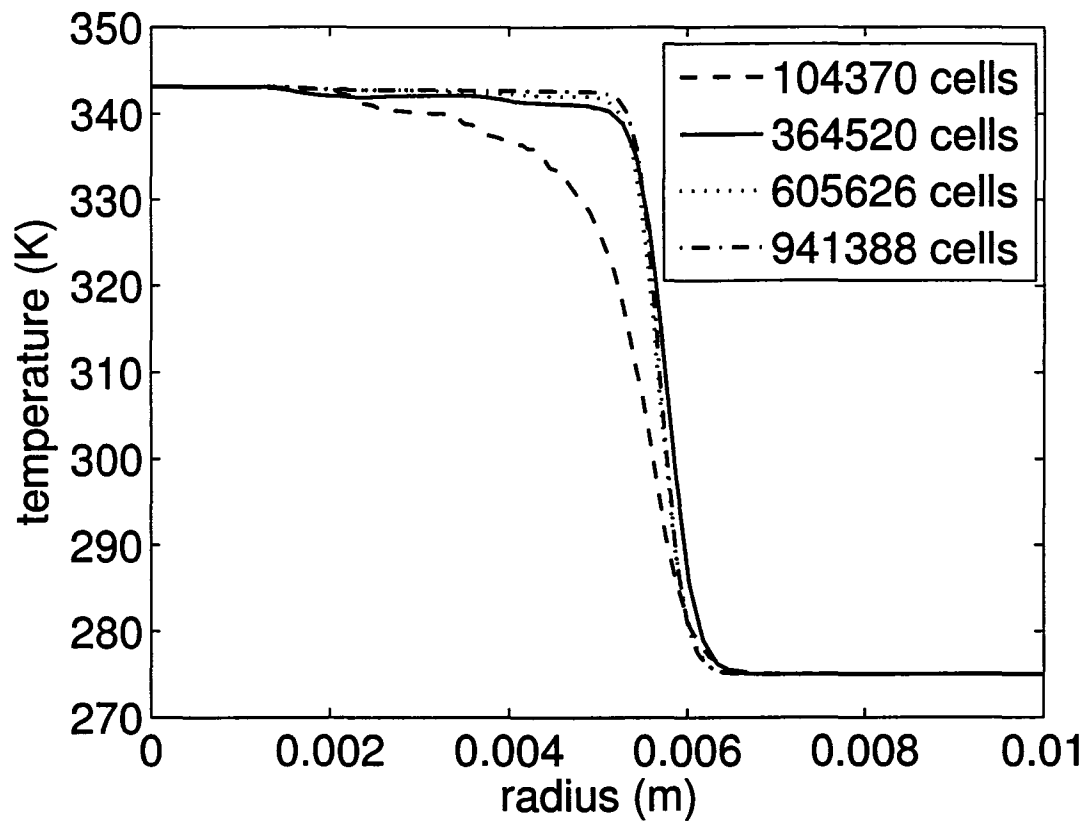


Figure 4.3: Temperature along a radial line in the midplane of the cell at a time of 0.01 s for several different numerical grids. The time step was 0.0001 s, $T_c = 275$ K, $v_i = 2$ mm, and $b = 1$ mm.

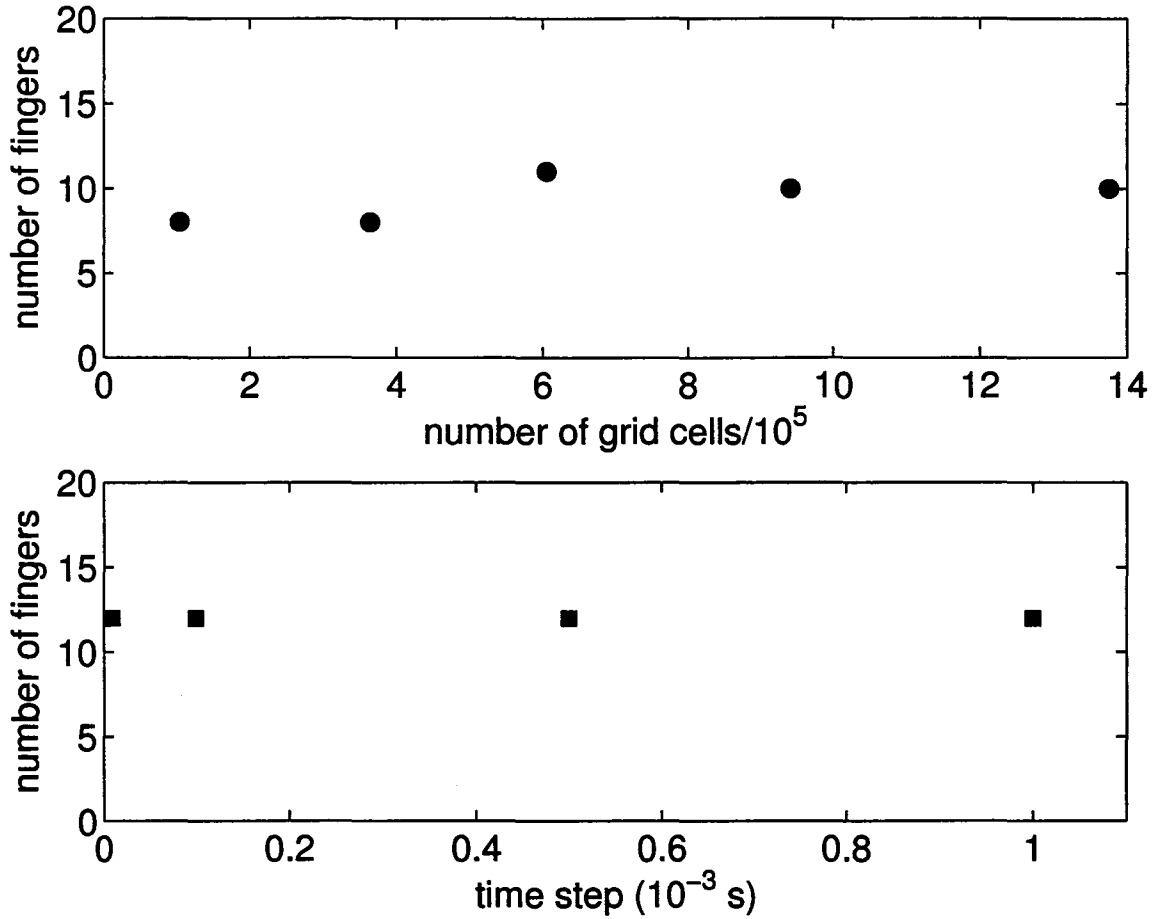


Figure 4.4: (a) Number of fingers at a time of 0.01 s as a function of the number of cells in the numerical grid. The time step here is 0.0001 s. (b) Number of fingers at a time of 0.15 s as a function of time step for a grid with 364520 cells. For all runs shown here, $T_c = 275K$ and $v_i = 2$ m/s.

fluid. In contrast, fig. 4.5(b) shows an image from a run in which water was injected into glycerine. Here the injected fluid has a lower viscosity, the interface is unstable, and fingers of water penetrate into the glycerine as expected.

Simulations of water injected into glycerine were performed for cell widths b of 0.5, 1, and 2 mm. For $b = 1$ mm inlet velocities v_i of 1 and 2 m/s were used, while for $b = 0.5$ and 2 mm $v_i = 2$ m/s. The average wavelength of the resulting finger patterns, determined using the method described below, was $\langle \lambda \rangle / b = 6.1 \pm 1.5$. This value agrees with the results found in previous miscible viscous fingering experiments[5],[6].

4.4 Results

Fig. 4.6 shows a sequence of images from a simulation in which hot glycerine ($T_h = 343.15$ K) is injected into cold glycerine ($T_c = 284$ K). The image shows contours of radial velocity in the midplane of the cell. Initially (Fig. 4.6(a)) the contours are circular, indicating uniform radial flow. As time progresses, however, the radial flow becomes unstable and fingers form, as in Fig. 4.6(b). Figure 4.7 shows the temperature in the cell midplane corresponding to Fig. 4.6(c). In this figure white represents T_h and black represents T_c . Figs. 4.6(b) and 4.7 show that the fingers are composed of the injected hot glycerine penetrating into the colder glycerine. These images are strikingly similar to those obtained in our previous experiments [9]: Fig. 4.8 shows an image from an experiment with $b = 1$ mm, inlet pressure $P = 62700$ Pa, $T_c = 280.8$ K and $T_h = 343.15$ K. In this image, the injected hot glycerine (black) has formed fingers which have penetrated into the colder glycerine (clear). The similarities and differences between the experiments and simulations will be discussed in the next section.

Fig. 4.9 is a grayscale image of the tangential component of the flow velocity in

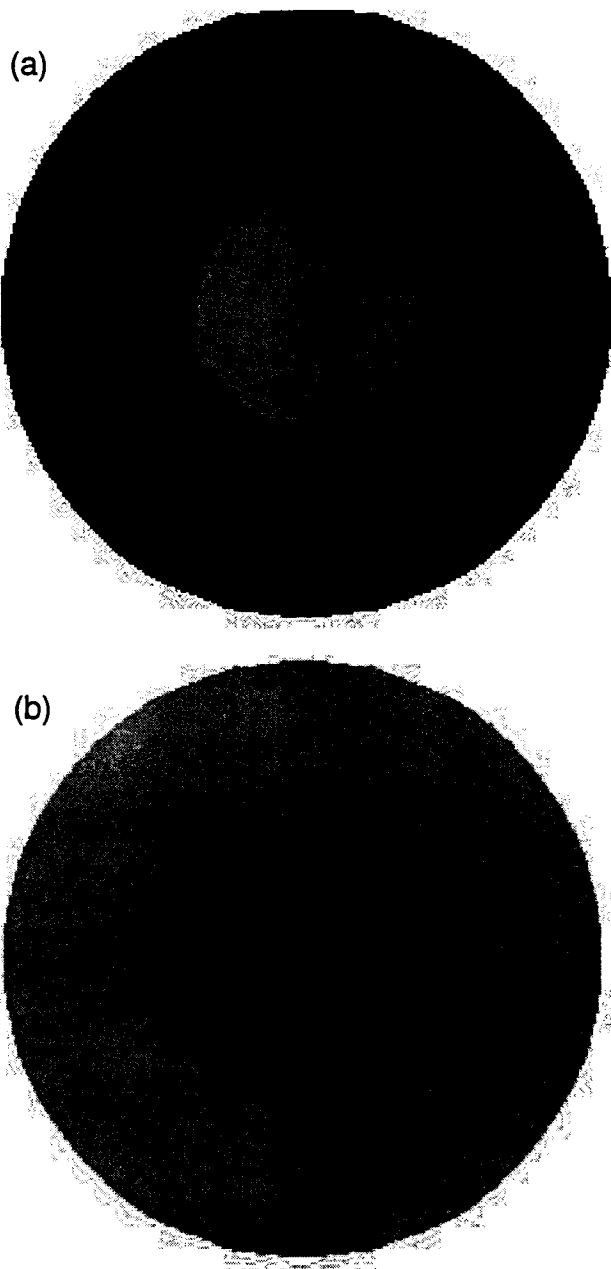
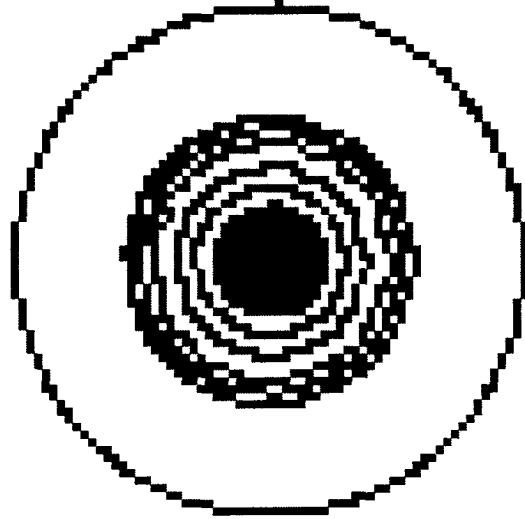


Figure 4.5: (a) Results from a simulation of glycerine injected into water with $b = 1$ mm and $v_i = 2$ m/s at a time of 0.2 s. (b) Water injected into glycerine for the same conditions as (a). Light and dark represent glycerine and water respectively.

(a)



(b)

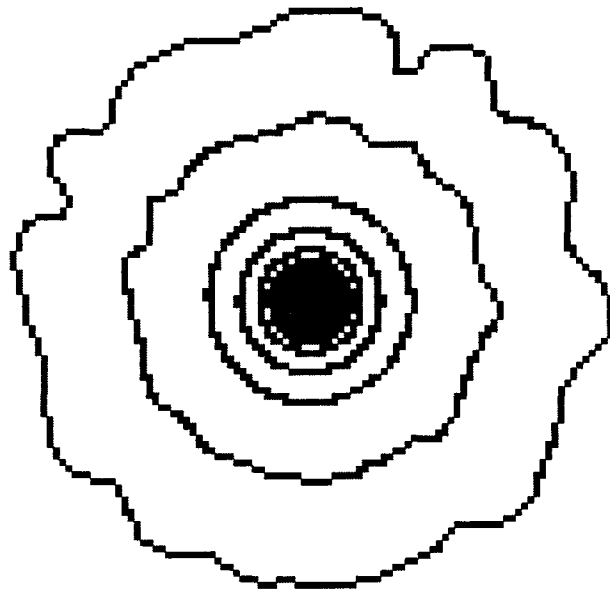


Figure 4.6: Contours of radial velocity on the midplane of the cell from a simulation with $b = 1\text{mm}$, $v_i = 1\text{ m/s}$, $T_c = 284\text{ K}$, and $T_h = 343.15\text{ K}$ at (a) 0.02 s and (b) 0.14 s . The field of view is 0.0439 m .

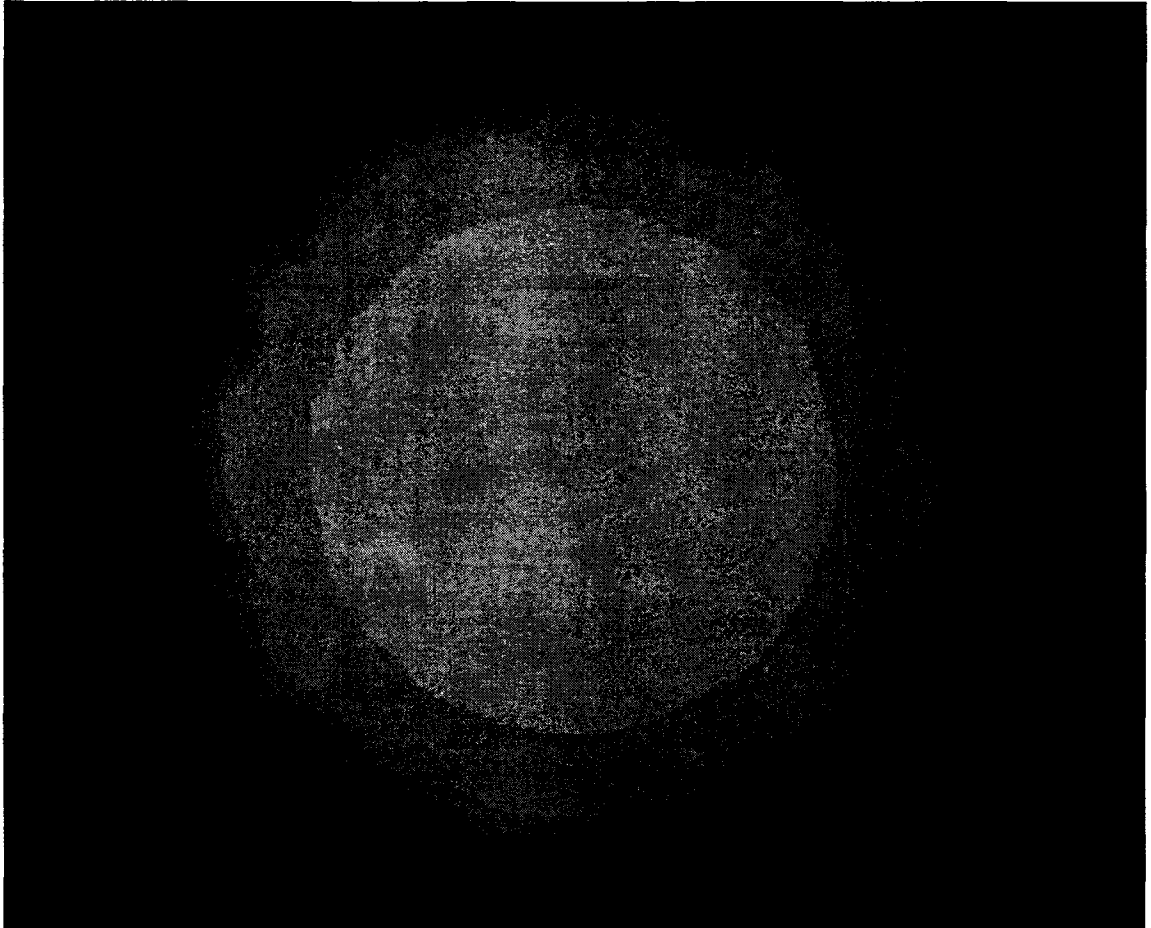


Figure 4.7: A simulation image showing the temperature in the midplane of the cell corresponding to Fig. 4.6(b). Light represents T_h and dark, T_c .

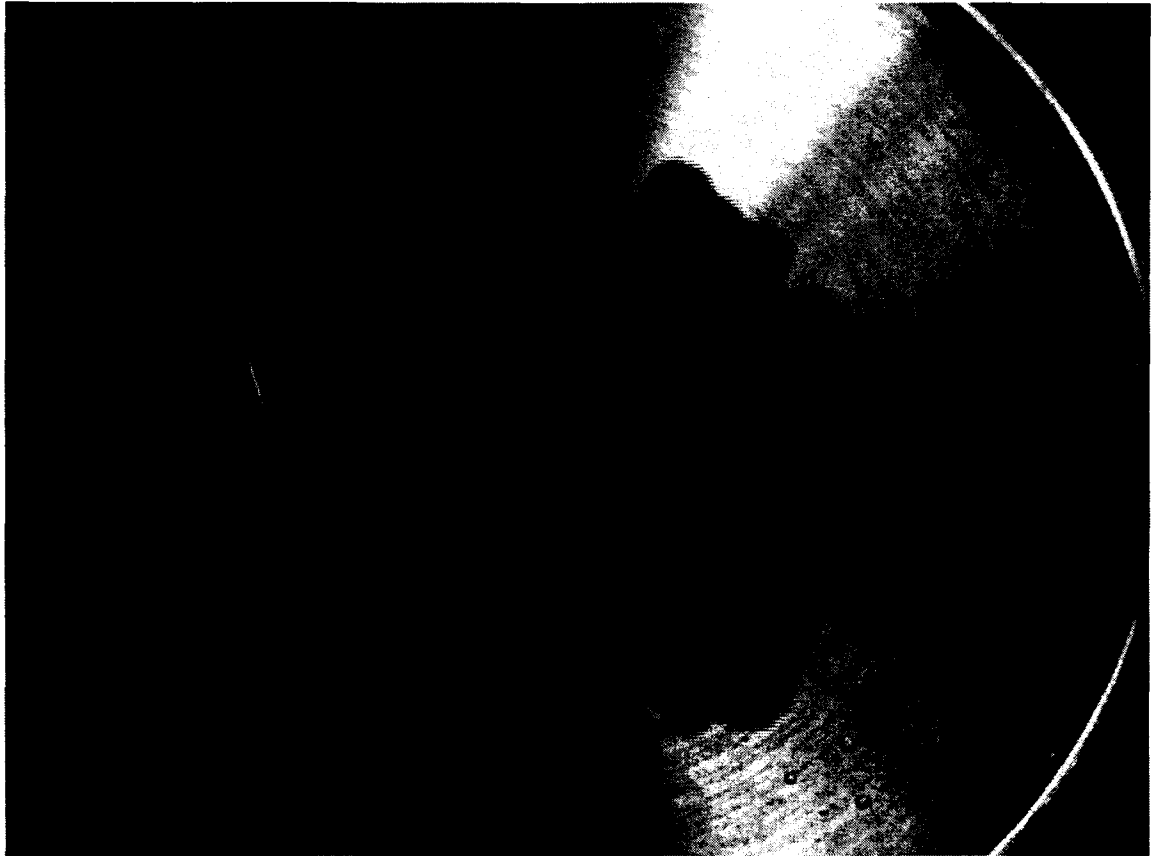


Figure 4.8: An image from an experimental run with $b = 1$ mm, $T_c = 280.81$ K, and inlet pressure $P = 62700$ Pa at a time of 1.1 s after the start of the run. The hot glycerine is dyed black to distinguish it from the cold glycerine initially in the cell.

the midplane of the cell, with dark indicating negative (clockwise) and light, positive tangential velocities. This is overlaid with contours of radial velocity to show the finger positions. Within the fingers, the direction of the tangential velocity indicates that the flow of the injected hot glycerine is focused towards the tips of the fingers. In the region outside the fingers the cold glycerine flows away from the fingers.

While the spacing of the fingers in Fig. 4.6 is not perfectly uniform, they do have a characteristic wavelength. Data from the simulations can be analyzed to obtain information about the wavelength λ and growth rate σ of the fingers. In particular, grayscale images showing the volume fraction of hot and cold glycerine in each numerical cell, obtained with the VOF method described above, are used for analysis as they provide information about the boundary between the injected and displaced fluid.

The method used to analyze the images is the same as that used in our experimental work [9]. The radial position r of the boundary between the hot and cold glycerine, measured from the center of the cell, was determined as a function of the azimuthal angle θ . $r(\theta)$ is then Fourier transformed and the peak of the FFT power spectrum at early times is used to find the angular wavenumber n of the instability. n corresponds to the number of fingers around the perimeter of the boundary. The wavelength λ of the instability is then given by $\lambda = 2\pi r_c/n$, where r_c is the radial position of the boundary at the time when the instability first becomes apparent in the FFT, that is, at which the peak at n starts to grow.

Figure 4.10(a) shows a sample image, with black indicating the hot injected fluid. The FFT of the boundary is shown in Fig. 4.10(b). The length of the fingers is expected to grow as $e^{\sigma t}$ at early times [1, 3]. Fig. 4.10(c) is a semilogarithmic plot of the amplitude of the peak at $n = 8$ as a function of time. The data at early times fall on a straight line, the slope of which gives the growth rate σ . The small peak at

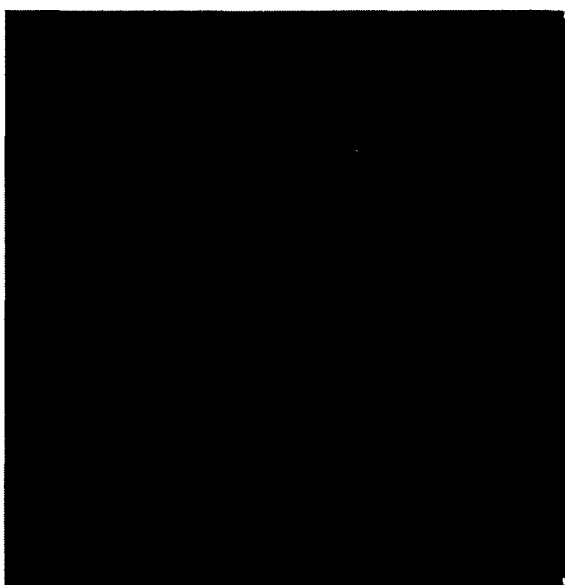


Figure 4.9: A grayscale simulation image showing the tangential velocity in the cell midplane overlaid with contours of radial velocity. The light and dark areas (indicating positive and negative tangential velocity, respectively) show that flow is focused towards the finger tips. The conditions were the same as in Fig. 4.7.

$n = 1$ in Fig. 4.10(b) arises simply because the origin of the coordinate system used in the analysis of the data does not coincide exactly with the center of the injected fluid.

For the simulations discussed in this paper, the angular wave number $n = 8$ at early times for all runs involving hot glycerine injected into colder glycerine, that is, the dominant peak of the FFT indicated that there were eight fingers around the boundary between the two fluids. The radius at which the instability first appears does not vary systematically with T_c or v_i within the scatter of our results, but does appear to increase with b , and since $\lambda = 2\pi r_c/n$, the same is true of the wavelength. Fig. 4.11(a) shows λ as a function of v_i for the three cell widths, for several values of T_c , while Fig. 4.11(b) shows λ as a function of T_c for different values of v_i .

Averaging over all runs for a given cell width b , we find $\langle \lambda \rangle = 2.2 \pm 0.4, 2.5 \pm 0.3$, and 3.6 ± 0.5 mm for $b = 0.5, 1$, and 2 mm respectively. The values of $\langle \lambda \rangle$ for $b = 0.5$ and 1 mm are very similar, but $\langle \lambda \rangle$ is larger for the 2 mm cell. Figure 4.12 shows $\langle \lambda \rangle$ as a function of b from both the simulations and the experiments [9]. With the exception of the values for $b = 0.5$ mm, the simulation results are lower than the values obtained from our experimental work. The dimensionless ratio $\langle \lambda \rangle/b$ is plotted in the inset to Fig. 4.12. Experimentally, we had found that $\langle \lambda \rangle/b = 5.6 \pm 0.8$ for the two smaller cell widths, while $\langle \lambda \rangle/b = 3.7 \pm 0.5$ for $b = 2$ mm. From the simulations, $\langle \lambda \rangle/b = 4.4 \pm 0.8, 2.5 \pm 0.3$, and 1.8 ± 0.3 for $b = 0.5, 1$, and 2 mm respectively.

While uncertainties in the fitting process led to some scatter in the values of the growth rates obtained from the simulations, σ was found to be independent of the wall temperature T_c . For the two thicker cells, the growth rate increased with increasing inlet velocity, while for $b = 0.5$ mm there was substantial scatter in the data and no systematic dependence on v_i could be discerned. σ was also found to decrease with increasing b . Based on these results, we averaged the growth rates obtained at a given

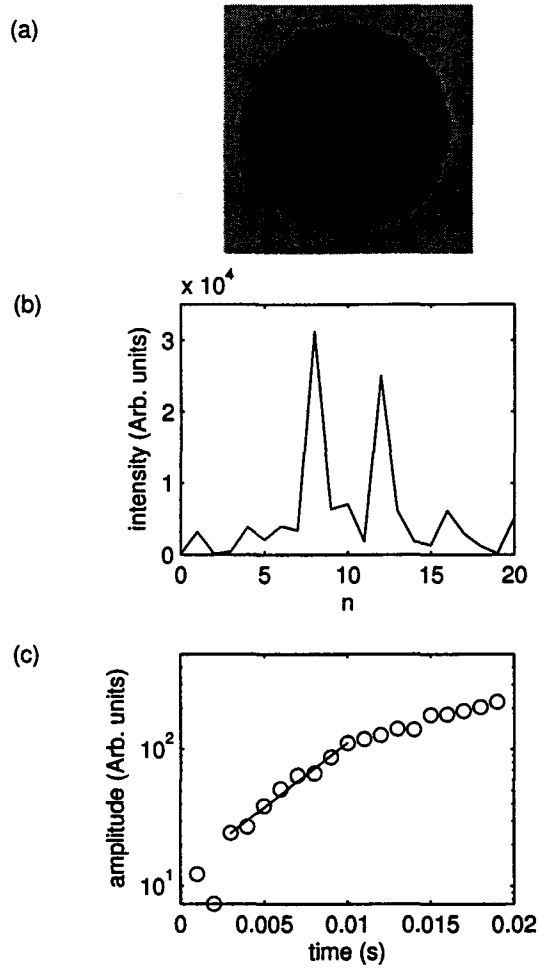


Figure 4.10: (a) An image from a simulation with $b = 1$ mm, $v_i = 2$ m/s, and $T_c = 275$ K at a time of 0.016 s. Black represents the injected hot glycerine and the surrounding gray represents the colder glycerine. (b) The Fourier power spectrum of $r(\theta)$ determined from the boundary in (a). (c) Amplitude as a function of time of the peak at $n = 8$. A fit to the data at early times is indicated by the solid line.

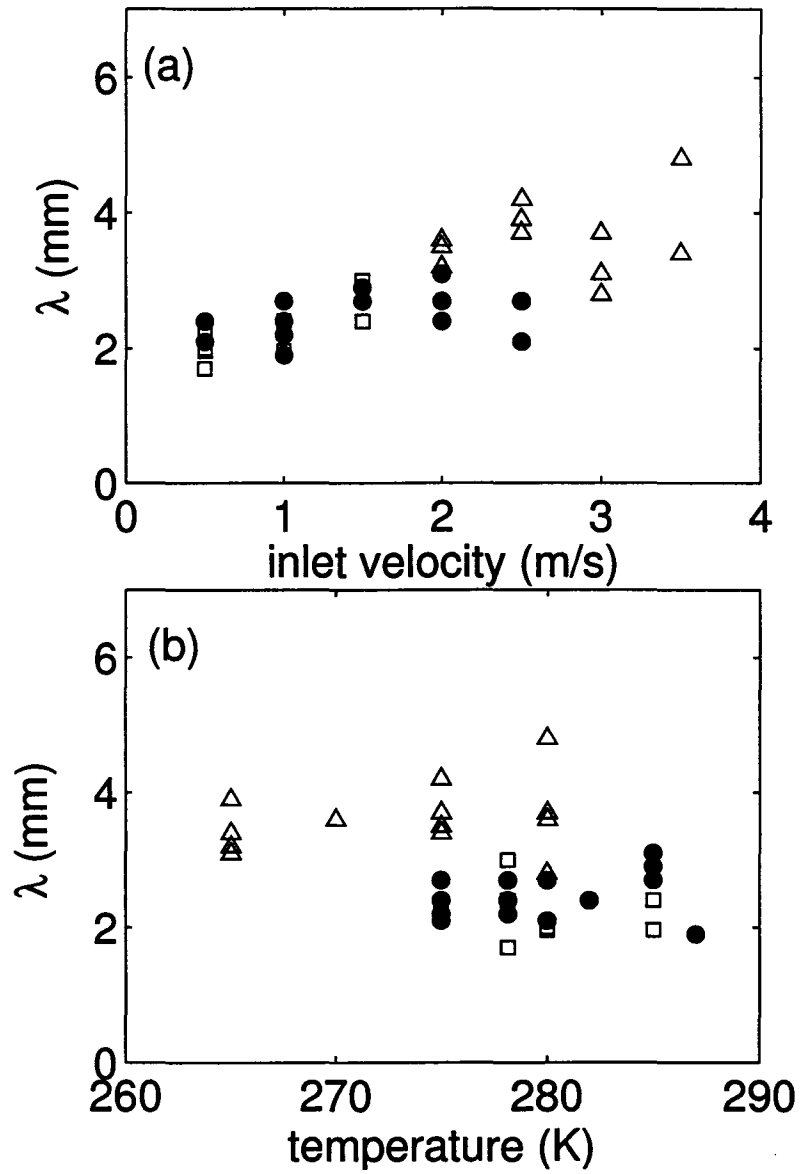


Figure 4.11: (a) The wavelength λ of the fingers as a function of inlet velocity obtained from the simulations. Open squares: $b = 0.5$ mm; solid circles: $b = 1$ mm; open triangles: $b = 2$ mm. (b) Wavelength as a function of T_c .

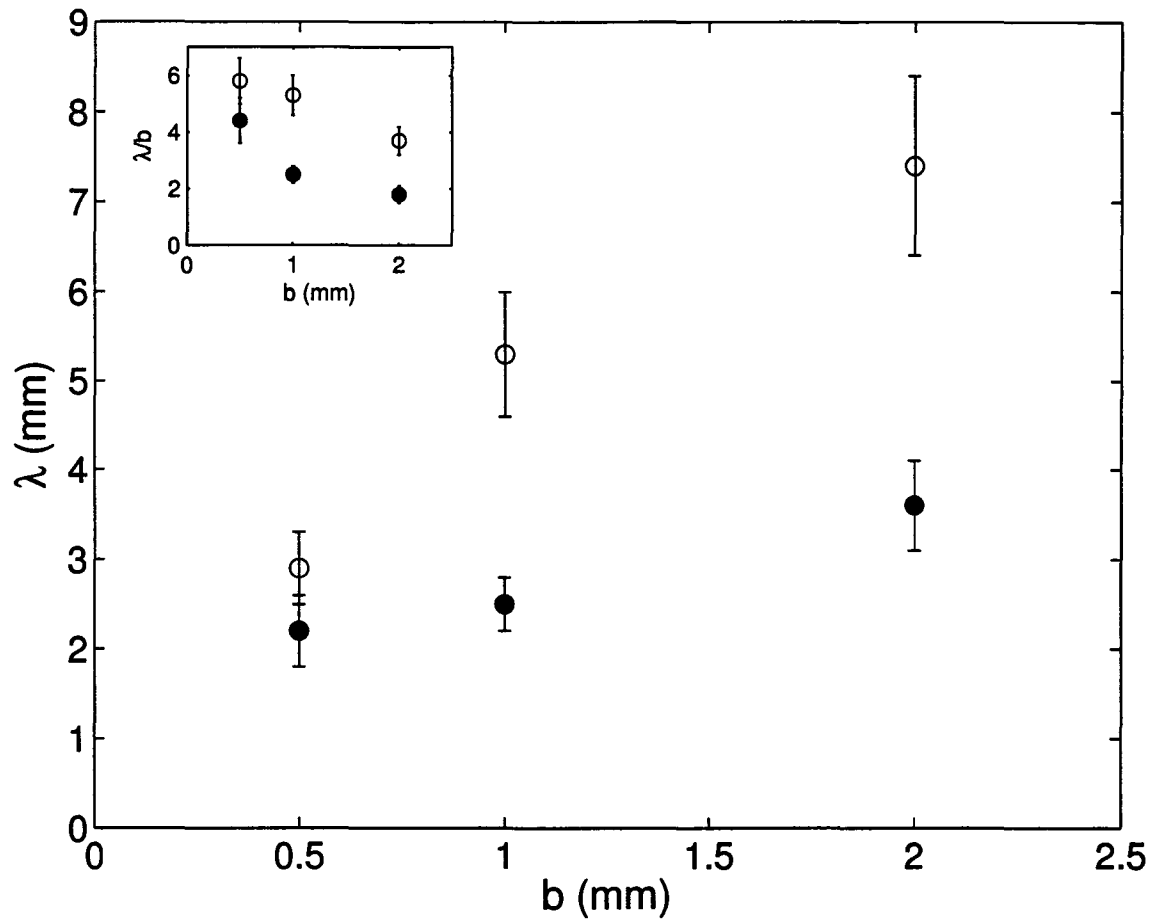


Figure 4.12: The wavelength averaged over T_c and v_i plotted as a function of cell width b for both simulations (solid circles) and experiment (open circles). The inset shows the ratio λ/b for both cases.

velocity and cell width, but different temperatures. The averaged growth rates were scaled by $1/t_\kappa$, where t_κ is the thermal diffusion time, $t_\kappa = b^2/\kappa$. $\kappa = \alpha/\rho C_p$ is the thermal diffusivity, defined in terms of the quantities listed in Table 4.1. The inlet velocities were scaled by b/t_κ . σt_κ is plotted as a function of $v_i b/t_\kappa$ in Fig. 4.13. The data scaled in this way collapse and, within our scatter, fall on a single curve.

Fingering is only observed over a range of values of wall temperature (i.e., the viscosity ratio) and inlet velocity. Outside of this range the boundary between the injected and displaced fluid is stable over the duration of our simulations. Figure 4.14 shows the stability diagram for $b = 1$ mm. Fingering is only observed for high enough values of the velocity and the viscosity ratio $\mu(T_c)/\mu(T_h)$. From the figure, fingers are not observed below $M_c \approx 20$. This value of M_c is much higher than the value of $3/2$ expected from previous theoretical and experimental work on fingering between two miscible fluids [14, 6, 7, 8]. This is due to the fact that the viscosity ratio in used Fig. 4.14 is that determined from the temperatures of the injected and displaced fluids at the start of a simulation. By the time the injected fluid spreads to r_c where the fingers start to grow, it will have cooled substantially and the value of M there will be lower. We determined the viscosity ratio at the location of the instability (which we denote by m_c) from our simulation results by finding the temperature and viscosity on either side of the boundary region separating the two fluids when it reaches r_c . Applying this method to various runs with $b = 1$ mm gives an estimate of the critical viscosity ratio at the location of the instability of $m_c \approx 4$, much closer to but still higher than the expected value.

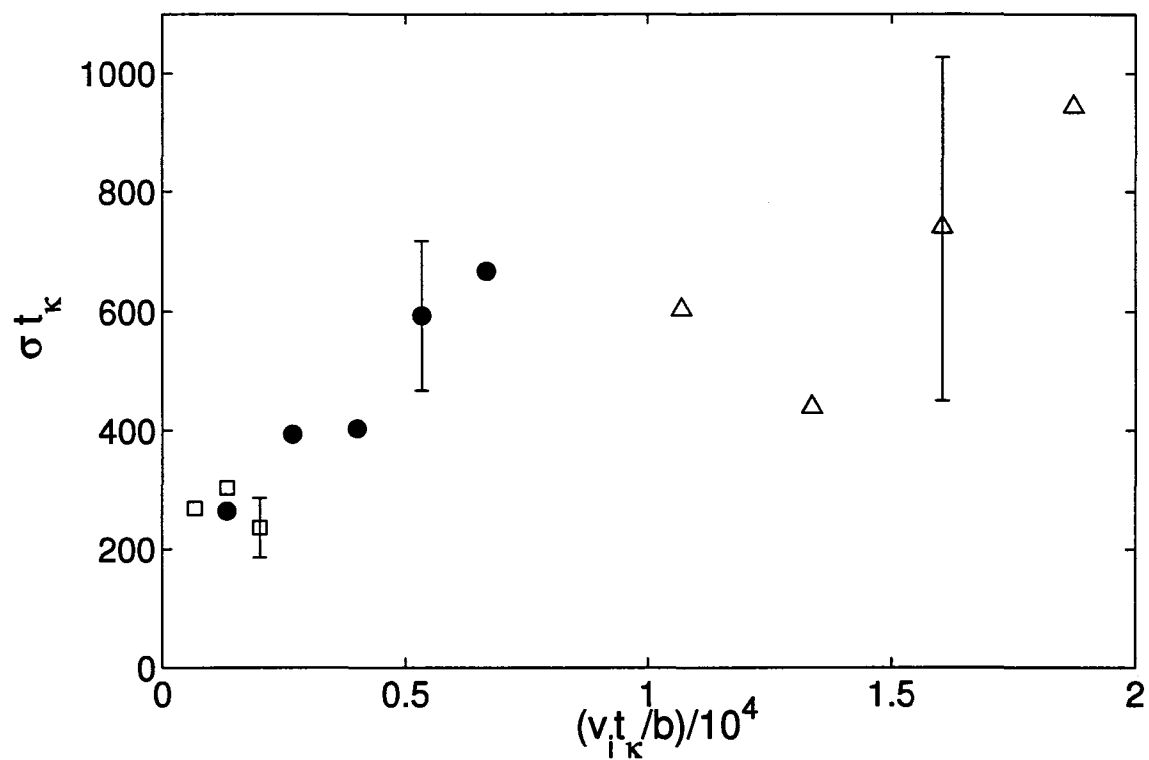


Figure 4.13: The scaled growth rate σt_κ as a function of scaled inlet velocity $v_{i\kappa}/b$ obtained from the simulations. Squares: $b = 0.5$ mm, circles: $b = 1$ mm, triangles: $b = 2$ mm.

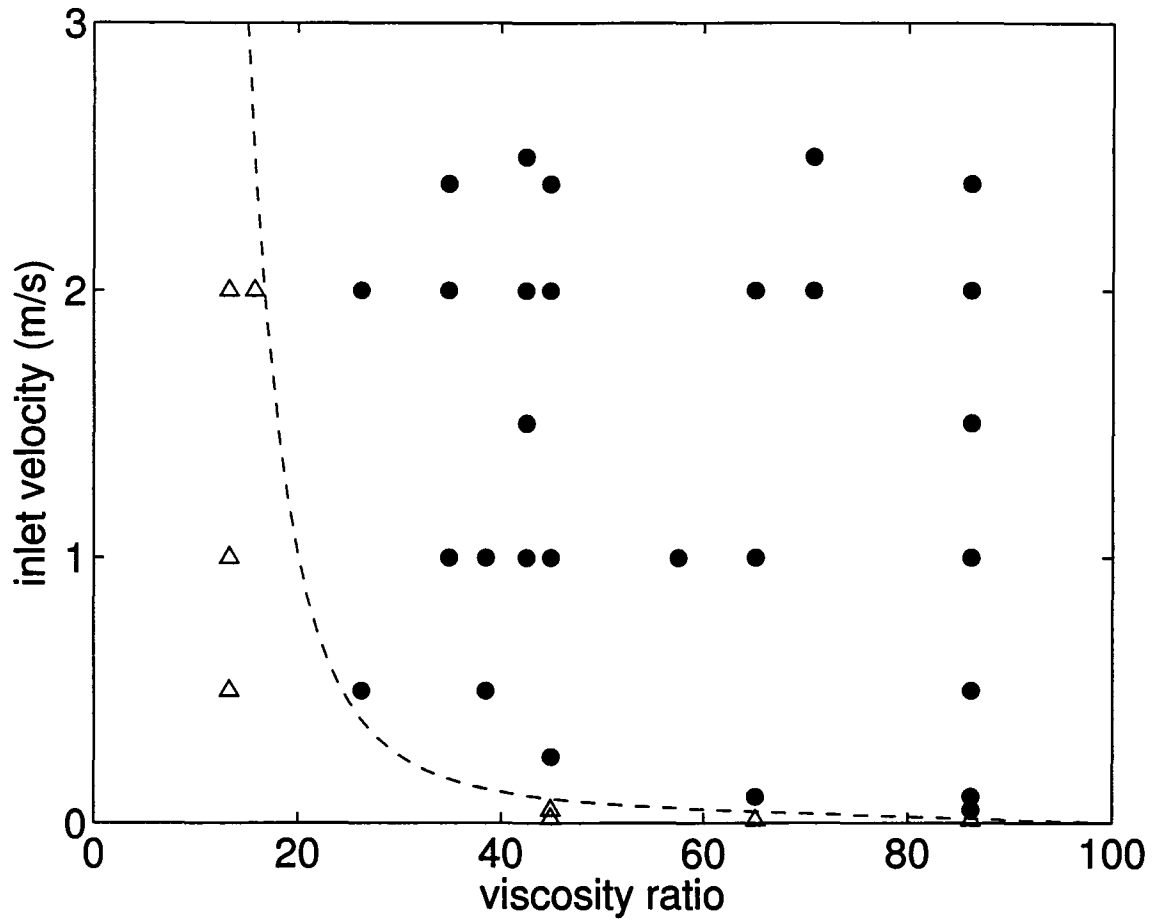


Figure 4.14: A stability diagram showing the range of existence of the fingering instability determined from the simulations for $b = 1$ mm. The solid circles represent simulations for which fingering was observed and the open triangles cases where there was no fingering. The dashed line is the approximate stability boundary above which the flow is unstable and below which it is stable.

4.5 Discussion

The fingering instability observed in our simulations looks very similar to that seen in our previous experiments [9] but, as discussed below, there are some important quantitative differences. There are also differences between the system we simulate and the experiments that may affect our results. First, in the simulations the walls of the cell are kept at a constant temperature whereas in the experiments they are kept cool by circulating coolant and may heat up as hot glycerine flows through the cell. Second, the boundary conditions at the inlet to the cell are different. In the simulations, the velocity of the glycerine entering the cell is specified, while in the experiments, we applied a pressure to a piston to force the glycerine into the cell. Attempts to perform simulations with a constant pressure at the inlet were not successful.

In the simulations, λ for a given cell width was found to be independent of both the viscosity ratio and the inlet velocity. Similarly, in our experiments λ was independent of the viscosity ratio and the inlet pressure [9]. Based on previous theoretical and experimental work [12, 11, 20, 21, 22], we would expect λ to be proportional to b in the high Peclet number regime. The Peclet number $Pe = lv/\kappa$, where l is a characteristic length, v a characteristic velocity, and κ the thermal diffusivity, is a measure of the importance of convective flow relative to thermal diffusion. In our simulations, $5300 \leq Pe \leq 1.9 \times 10^6$, so we are always in the high Pe regime. The same was true in our experimental studies. Our experimentally measured wavelengths appeared to be proportional to b for small b , but the ratio $\langle \lambda \rangle / b$ decreased for the largest cell. In contrast, the wavelength of the simulated fingering patterns is not proportional to cell width, but rather increases only weakly with b over the range covered here. The wavelength determined from the simulations for $b = 0.5$ mm is the

same as for the experiments, but the wavelengths for the two larger cell widths are lower than those observed in our experimental work.

We had previously suggested [9] that the decrease in $\langle\lambda\rangle/b$ for $b = 2$ mm in the experiments might be due to increased three-dimensional effects in the thicker cell, and recent simulations of density-driven miscible viscous fingering [22] indicated that the flow was significantly three-dimensional even in thin cells. Thus the decrease in $\langle\lambda\rangle/b$ in our simulations may also be due to three-dimensional effects. In support of this suggestion, we show in Fig. 4.15 the velocity field in a vertical plane near the center of the numerical cell for the three cell thicknesses. For $b = 2$ mm the flow is significantly three dimensional, with the velocity vectors indicating some circulation of the fluid in the region of the inlet hole.

Another possible reason for the difference in the experimental and simulated values of λ is that, because of reduced noise, the instability can be detected relatively earlier in the simulations than in the experimental images. Finally, it is often difficult to determine a starting time for the instability from the FFT data in the simulations, and this affects the values of λ .

The growth rates of the instability determined from the simulations are significantly higher than those obtained from the experiments. Experimentally, for $b = 1$ mm we found $3.0 \text{ s}^{-1} \leq \sigma \leq 15.0 \text{ s}^{-1}$ [9]; the simulations give growth rates 20 times higher. This difference may be due to earlier detection of the signal in the simulation images as described above or it may indicate a real difference between the simulations and the experiments.

There are practical limitations to the simulations that may affect the results discussed above. The data files produced by the program are large and as a compromise between data collection and storage requirements, data were saved every 10th time step (corresponding to 0.001 s of simulated time). However, for a given v_i , flow in

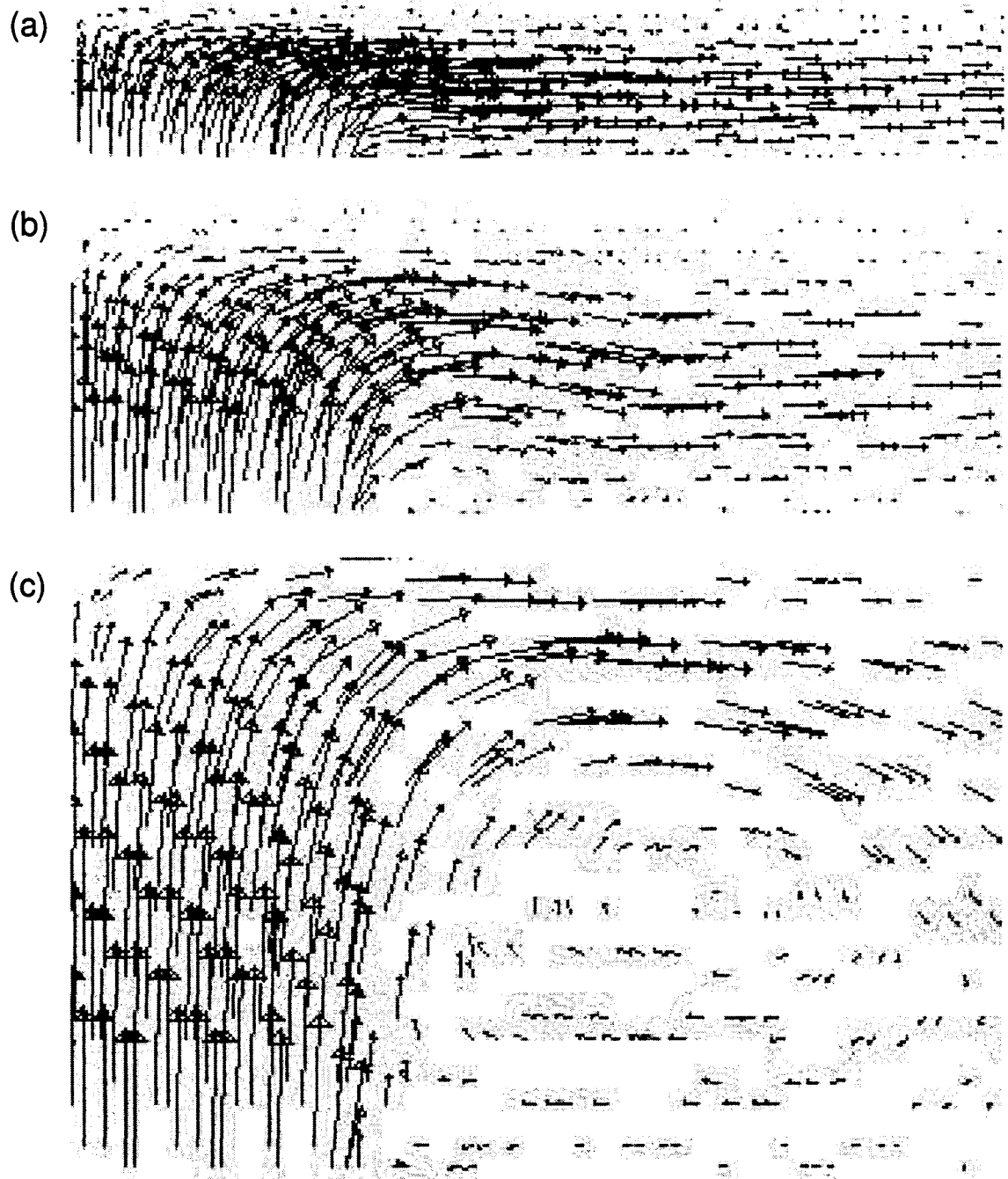


Figure 4.15: Velocity vectors shown for a portion of a vertical plane of the numerical grid. The field of view is 3 mm and the inlet hole is at the bottom left in each case. (a) $b = 0.5$ mm, $v_i = 1$ m/s, $T_c = 278.15$ K, $t = 0.018$ s; (b) $b = 1$ mm, $v_i = 1.5$ m/s, $T_c = 275$ K, $t = 0.02$ s; and (c) $b = 2$ mm, $v_i = 3.5$ m/s, $T_c = 280$ K, $t = 0.035$ s. The velocity vectors show increased three-dimensional flow as b is increased.

the cell is much faster for lower cell widths and so it is possible that more data would improve the results, especially for the determination of σ for $b = 0.5$ mm. The same number of grid cells is used for all runs, regardless of cell width. This means that the resolution in the vertical direction decreases as b is increased, which could increase the scatter for the $b = 2$ mm case.

As discussed above, fingering was not observed for low values of M or v_i . Similar behavior was seen in the experiments [9], in which the flow was stable at low viscosity ratios and inlet pressures. The critical viscosity ratio $M_c \approx 20$ obtained from Fig. 4.14 for $b = 1$ mm agrees well with our experimental value of M_c [9], but is much greater than expected based on previous theory and experiments on miscible fingering [14, 6, 7, 8]. By accounting for the cooling of the hot glycerine as it flows through the cell and calculating the viscosity ratio at the location at which the instability first becomes visible, a critical viscosity ratio $m_c \approx 4$ is obtained. While still higher than expected [14, 6, 7, 8], this is much closer to the expected value of the critical viscosity ratio.

4.6 Conclusion

We have performed numerical simulations of a fingering instability in a single fluid with a strongly temperature-dependent viscosity. Fingering only occurs for high enough values of the inlet velocity and the viscosity ratio, in agreement with behavior seen in our experimental work [9]. The wavelength λ of the fingers is independent of both inlet velocity and viscosity ratio, again consistent with the experimental results. Except for the thinnest cell studied, the wavelengths obtained from the simulations are smaller than those from the experiments, and do not depend as strongly on cell width. The growth rates of the fingers were higher than those determined from ex-

periments. Despite these difference, the instability seen in the simulations is very similar to that seen experimentally.

Acknowledgments

We gratefully acknowledge helpful discussions with E. Thornhill. The simulations were done using the computer resources of the Atlantic Computational Excellence Network at Memorial University. This research was supported by the National Sciences and Engineering Research Council of Canada.

Bibliography

- [1] P.G. Saffman and G. Taylor, Proc. R. Soc. London A **245**, 312 (1958).
- [2] L. W. Lake, Enhanced Oil Recovery (Prentice-Hall, Englewood Cliffs, 1989).
- [3] G. M. Homsy, Annu. Rev. Fluid Mech. **19**, 271 (1987).
- [4] K. V. McCloud and J. V. Maher, Phys. Rep. **260**, 139 (1995).
- [5] L. Paterson, Phys. Fluids **28**, 26 (1985).
- [6] E. Lajeunesse, J. Martin, N. Rakotomalala, and D. Salin, Phys. Rev. Lett. **79**, 5254 (1997).
- [7] E. Lajeunesse, J. Martin, N. Rakotomalala, D. Salin, and Y. C. Yortsos, J. Fluid Mech. **398**, 299 (1999).
- [8] E. Lajeunesse, J. Martin, N. Rakotomalala, D. Salin, and Y. C. Yortsos, Phys. Fluids **13**, 799 (2001).
- [9] K. E. Holloway and J. R. de Bruyn, Can. J. Phys. **83** 551 (2005).
- [10] R. L. Chouke, P. van Meurs, and C. van der Poel, Trans. AIME **216**, 188 (1959).
- [11] C.W. Park, S. Gorell, and G.M. Homsy, J. Fluid Mech. **139**, 291 (1984).
- [12] T. Maxworthy, Phys. Rev. A **39**, 5863 (1989).

- [13] C.T. Tan and G.M. Homsy, *Phys Fluids* **29**, 3549 (1986).
- [14] Z. Yang and Y. C. Yortsos, *Phys. Fluids* **9**, 286 (1997).
- [15] Fluent Inc. FLUENT Version 6.1.22 [computer program]. Fluent Inc., Lebanon, N.H. 2004.
- [16] H. K. Versteeg and W. Malalasekera, *An Introduction to Computational Fluid Dynamics: The Finite Volume Method* (Reading, MA: Addison-Wesley, 1995).
- [17] Fluent Inc. GAMBIT Version 2.0.4 [computer program]. Fluent Inc., Lebanon, N.H. 2004.
- [18] S. V. Patankar, *Numerical Heat Transfer and Fluid Flow* (Hemisphere, Washington, D.C., 1980).
- [19] C. Ji, G. Ahmadi, and D. Smith, *Journal of Energy and Environment research*, **2**, 99 (2002).
- [20] J. Fernandez, P. Kurowski, P. Petitjeans, and E. Meiburg, *J. Fluid Mech.* **451**, 239 (2002).
- [21] J. Fernandez, P. Kurowski, L. Limat, and P. Petitjeans, *Phys. Fluids* **13**, 3120 (2001).
- [22] F. Graf, E. Meiburg, and C. Hartel, *J. Fluid Mech.* **451**, 261 (2002).

Chapter 5

Spreading and fingering in spin coating

5.1 Abstract

We study the spreading and fingering of drops of silicone oil on a rotating substrate for a range of rotation speeds and drop volumes. The spreading of the drop prior to the onset of fingering is found to follow the theoretically predicted time dependence, but with a large shift in time scale. For the full range of experimental parameters studied, the contact line becomes unstable and fingers develop when the radius of the drop becomes sufficiently large. We study the growth of perturbations around the perimeter of the drop, and find the growth rate of the most unstable mode to agree well with the predictions of lubrication theory. The number of fingers which form around the perimeter of the drop is found to be a function of both rotation speed and drop volume, and is also in excellent agreement with theoretical predictions.

5.2 Introduction

Spin coating is a process whereby a volume of fluid spreads on a rotating substrate due to the action of centrifugal force. Spin coating is used industrially to form thin, uniform coating films in, for example, the manufacture of CDs and flat-screen televisions, and in microlithography. A drop of fluid positioned on the axis of rotation of a spinning substrate flattens in the middle and forms a capillary ridge around its perimeter as it spreads radially. The capillary ridge can become unstable, leading to the development of fingers at the liquid-substrate contact line [1, 3, 2]. This in turn can lead to nonuniform coating of the substrate. Similar contact-line instabilities are observed in thin film flows down an inclined plane [4, 5, 6, 7, 8, 9] and in film flows driven by surface tension gradients [10, 11].

Several previous experimental studies of the fingering instability in spin coating have been carried out, beginning with the early work of Emslie et al. [1] Melo et al. [2] studied fingering for a range of viscosities, rotation speeds, and fluid volumes using silicone oil. Homsy and coworkers [3, 12] studied spin coating in both Newtonian and Non-Newtonian fluids. Togashi et al. [13] performed spin coating experiments for two Newtonian fluids and derived an analytical expression for the drop radius at which fingering appeared. Other workers have extended the range of rotation speeds [14] and volumes [15] studied. Features of the flow investigated in these experiments include the spreading of the drop prior to fingering, the evolution of the drop profile, the critical radius at which the instability occurs, the number of fingers which formed at the instability, and the growth rates of the fingers.

The spreading of the fluid drop prior to fingering has also been studied theoretically [1, 16, 17, 3, 2]. Emslie et al. [1] solved the equation for a cylindrical volume of fluid spreading under the action of a centrifugal force using the method of character-

istics, and showed that the drop radius r should evolve with time t as

$$\frac{r}{r_0} = \left(1 + \frac{4}{3} \frac{t H_0^2 \rho \omega^2}{\eta} \right)^{1/4} \quad (5.1)$$

or, in dimensionless form, as

$$r^*(t) = \left(1 + \frac{4}{3} t^* \right)^{1/4}. \quad (5.2)$$

Here r^* is given in units of r_0 , the initial radius of the drop, and t^* in units of the time scale for flow in the region near the contact line, $t_0 = \eta/H_0^2\rho\omega^2$. η is the viscosity of the fluid and ρ its density, ω the angular frequency of the spinning substrate, and H_0 the initial height of the drop. In deriving Eqs. (5.1) and (5.2) it was assumed that drop remains cylindrical and that its volume is constant. Wilson et al. also studied the spreading of a fluid drop prior to the onset of the fingering instability [16]. They found analytic solutions for $r(t)$ when the surface tension $\gamma = 0$ and in the low- γ limit, and studied the problem numerically for finite γ . Their finite- γ solution agreed with the experimental data of Fraysse and Homsy [3] while the analytic solution in the asymptotic limit described the behavior of $r(t)$ qualitatively but not quantitatively.

Once the radius of the fluid drop becomes large enough, the contact line becomes unstable and fingers appear. This instability has been treated theoretically in the context of lubrication theory. Troian et al. [4] studied the linear stability of the contact line for the flow of thin film of fluid down an inclined plane, a situation that is mathematically equivalent to flow under the influence of a centrifugal force. They assumed the presence of a thin precursor film ahead of the contact line to remove contact line singularities. They showed that the contact line is unstable for wave numbers $q \leq 0.9/\ell$, with the fastest growing mode at $q_m \approx 0.45/\ell$. Here

$\ell = H(3Ca)^{-1/3}$ is a characteristic length scale near the contact line. H is the height of the film in the region far from the contact line; for the spin coating problem in the lubrication approximation $H = (3u_0\eta/\rho\omega^2r)^{1/2}$ [3]. $Ca = \eta u_0/\gamma$ is the capillary number. Here u_0 is the flow velocity near the contact line. The dimensionless growth rate of the fastest growing mode was found to be approximately 0.5, depending weakly on the thickness of the precursor film. Spaid and Homsy [18] studied the stability of the contact line using a slip model and found the results to be independent of the contact line model. McKinley and co-workers [19, 20, 21] studied the linear stability of a drop of fluid spreading due to either a centrifugal force or a jet of air and Schwartz and Roy [22] have recently developed a mathematical model to study the stability of fluid drops during spin coating.

Defining r_c as the value of r at which fingers first form at time t_c , and assuming the drop volume V is conserved, it is straightforward to show that

$$\ell(t_c) = \left(\frac{\gamma V}{\pi \rho \omega^2 r_c^3} \right)^{1/3}. \quad (5.3)$$

From this and the wave number of the fastest growing mode, the number of fingers n that form is found to be [3]

$$n = \frac{\pi}{7} r_c^2 \left(\frac{\pi \rho \omega^2}{\gamma V} \right)^{1/3}. \quad (5.4)$$

In this paper, we present the results of a systematic study of the fingering instability in spin coating experiments using a relatively low viscosity silicone oil as the experimental fluid. We perform the experiments for a large range of drop volumes and angular velocities. In particular, our work focusses more on the growth rates of the fingers than previous work has [2, 3]. In section 5.3 we describe the experimental

apparatus and procedure. The results of our experiments are presented in 5.4, and in section 5.5 we compare our results with theoretical predictions and previous work.

5.3 Experiment

The experimental apparatus was designed to permit accurate positioning of the fluid drops at the center of the rotating substrate, as well as visualization of the perimeter of the drop as it spreads under the influence of the centrifugal force. The substrate is a circular transparent sapphire plate 10 cm in diameter. It is securely mounted in a holder, and a ball bearing system allows the holder to be rotated by a computer-controlled microstepper motor. The angular velocity ω is varied under computer control in the range 10.5-63 rad/s. The angular acceleration of the plate is also controllable, but is fixed at the maximum accessible value of 168 rad/s² for all runs discussed in this paper. With this acceleration the plate reached its set angular speed in approximately 0.4 s for the highest ω , and in all cases well before the onset of the fingering instability.

The spreading and fingering of the fluid drop was visualized with a shadowgraph optical system [23]. Light from a bright red light-emitting diode is collimated by two lenses arranged as a simple telescope, then directed to pass through the transparent sapphire plate from below. Another lens then focuses the shadowgraph image onto a charge-coupled device video camera mounted above the apparatus. Contrast in the shadowgraph is due to the deflection of light by thickness variations in the fluid. In our arrangement, this method produces high quality images in which the edges of the fluid drop are clearly defined, as shown in Fig. 5.1. The video camera is interfaced to a computer which records images of the flow as it progresses. Images are recorded at intervals chosen between 0.033 s and 0.1 s, and the integration time of the camera

is fixed at 10^{-4} s.

The plate is cleaned prior to each run with warm soapy water and then rinsed with clean water and finally with acetone. The plate is mounted in the apparatus and the system is carefully levelled. It is important that the fluid drop be accurately placed at the center of the plate. To find the center, we used a jig consisting of a metal plate with a small hole machined in its center that could be precisely positioned on the plate holder. Two micrometer-driven translation stages are used to position an arm above the center of the plate. A length of fine plastic tubing attached to a syringe pump is then mounted vertically in the arm. The syringe pump is used to place a specified volume of fluid onto the plate at a rate of 1 ml/min. The volume of fluid used ranged from 50 to 250 μl .

The experimental fluid is a Newtonian silicone oil with a viscosity η of 0.053 kg/ms at 20°C as measured with a shear rheometer using a cone-and-plate geometry. The density of the oil is $\rho = 963$ kg/m³ and its surface tension is $\gamma = 0.0208$ N/m. This silicone oil completely wets the sapphire surface and so has a contact angle of 0. As a result, the drops start to spread immediately once they are deposited on the plate. For our experiments, the drops were allowed to relax for 30 s before the rotation was started. The radius of a 100 μl drop of fluid increases by 0.16 cm during this relaxation time. We take r_0 to be the radius of the fluid drop at the end of this relaxation time, when the motor is turned on.

5.4 Results

Figure 5.1 shows a sequence of images from a run with a drop of volume $V = 50$ μl and angular speed $\omega = 36.8$ rad/s. The contact line is initially circular, as shown in Fig. 5.1(a). As the drop is rotated it spreads radially under the action of the centrifugal

force, initially flattening, then becoming thinner in the middle with a capillary ridge around the perimeter. At some radius r_c the contact line becomes unstable and fingers start to form, as shown in Fig. 5.1(b) and (c). As time progresses these fingers grow, and additional fingers can appear between those that form initially. As seen in Fig. 5.1, the spacing of the fingers around the perimeter of the drop is approximately uniform. Fingering was observed for the full range of experimental parameters studied here, and the behavior we observe is very similar to that reported in Refs. [3, 2].

Figure 5.2 shows the spreading of the drop from $t = 0$ to the time t_c at which the fingers begin to form. Figure 5.2(a) shows r/r_0 as a function of t for several runs on drops of the same volume but with different angular speeds. The same data are plotted on logarithmic axes in Fig. 5.2(b). As the plots show, there is an initial period during which the drop radius changes very little, followed by a period of more rapid spreading which appears linear in time in Fig. 5.2(a). The spreading rate of the drop depends strongly on ω ; analogous experiments for different V at fixed ω give similar results and show that the spreading rate also depends on V .

The theory of spin coating derived by Emslie et al. [1] predicts that the radius of the spreading drop should be described by Eq. 5.2, in which r is scaled by the initial radius r_0 and the time is scaled by t_0 , the characteristic time scale of the outer region of the flow [3]. Our data are plotted in this form in Fig. 5.3. The scaled data collapse very well, and have a dependence on t/t_0 that is close to the predicted $1/4$ power law at large times. On the other hand, our data are systematically shifted to the right of the predicted curve — shown as the dashed line in Fig. 5.3 — and the agreement cannot be improved by shifting our time origin by any reasonable amount. In contrast, Fraysse and Homsy found a rather poor collapse of their data using this scaling [3], and both they and Melo et al. [2] found that the spreading curves at

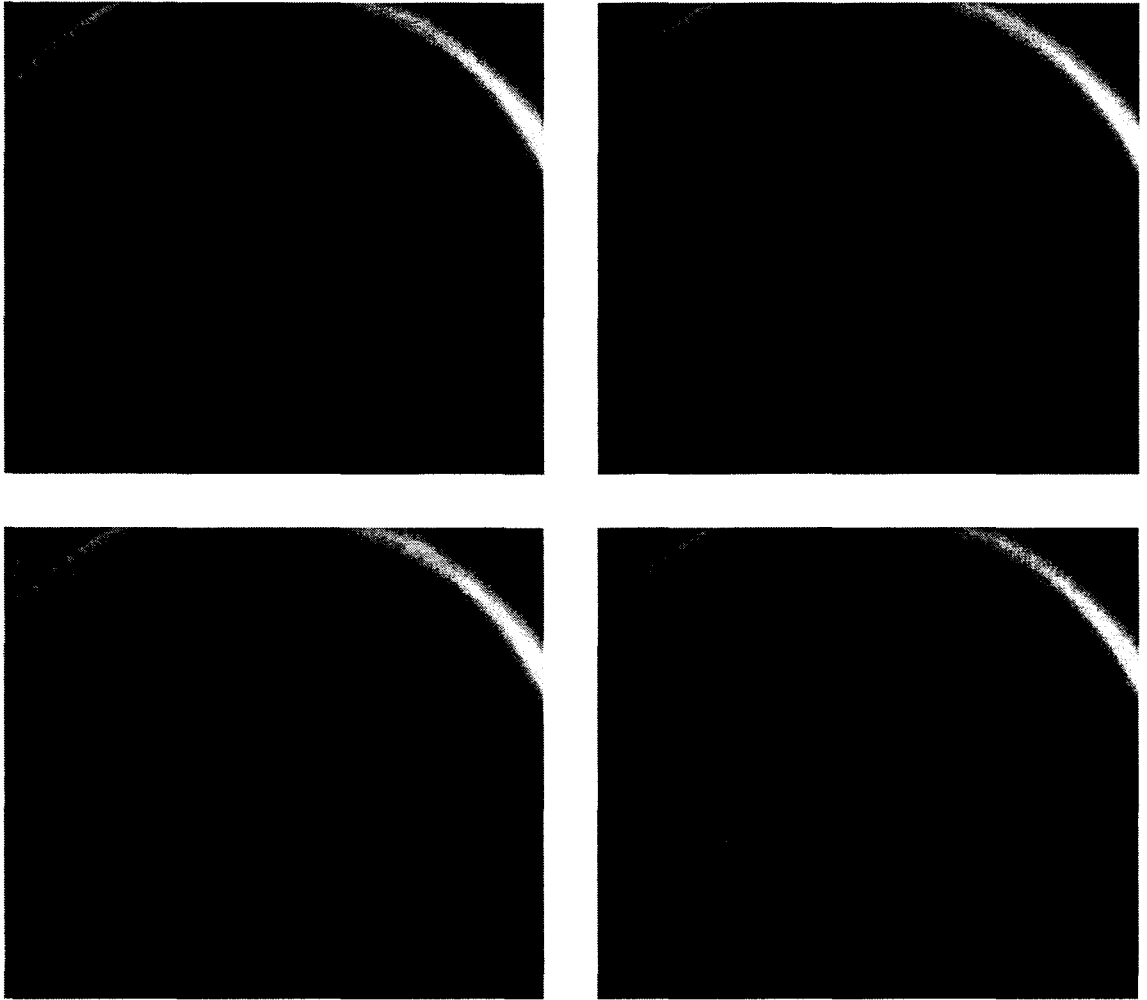


Figure 5.1: Shadowgraph images showing the spreading and fingering of a droplet of volume $V = 50\mu\text{l}$. The outer edge of the dark annular region corresponds to the edge of the drop. The angular speed ω of the turntable is 36.8 rad/s . Time $t = 0$ corresponds to the start of the rotation. At $t = 1.45\text{ s}$ (a) the drop is circular. At $t = 11.45\text{ s}$ (b) perturbations have started to grow around the perimeter of the drop. In image (c) ($t = 21.45\text{ s}$) and (d) ($t = 31.45\text{ s}$) fingers have developed and grown.

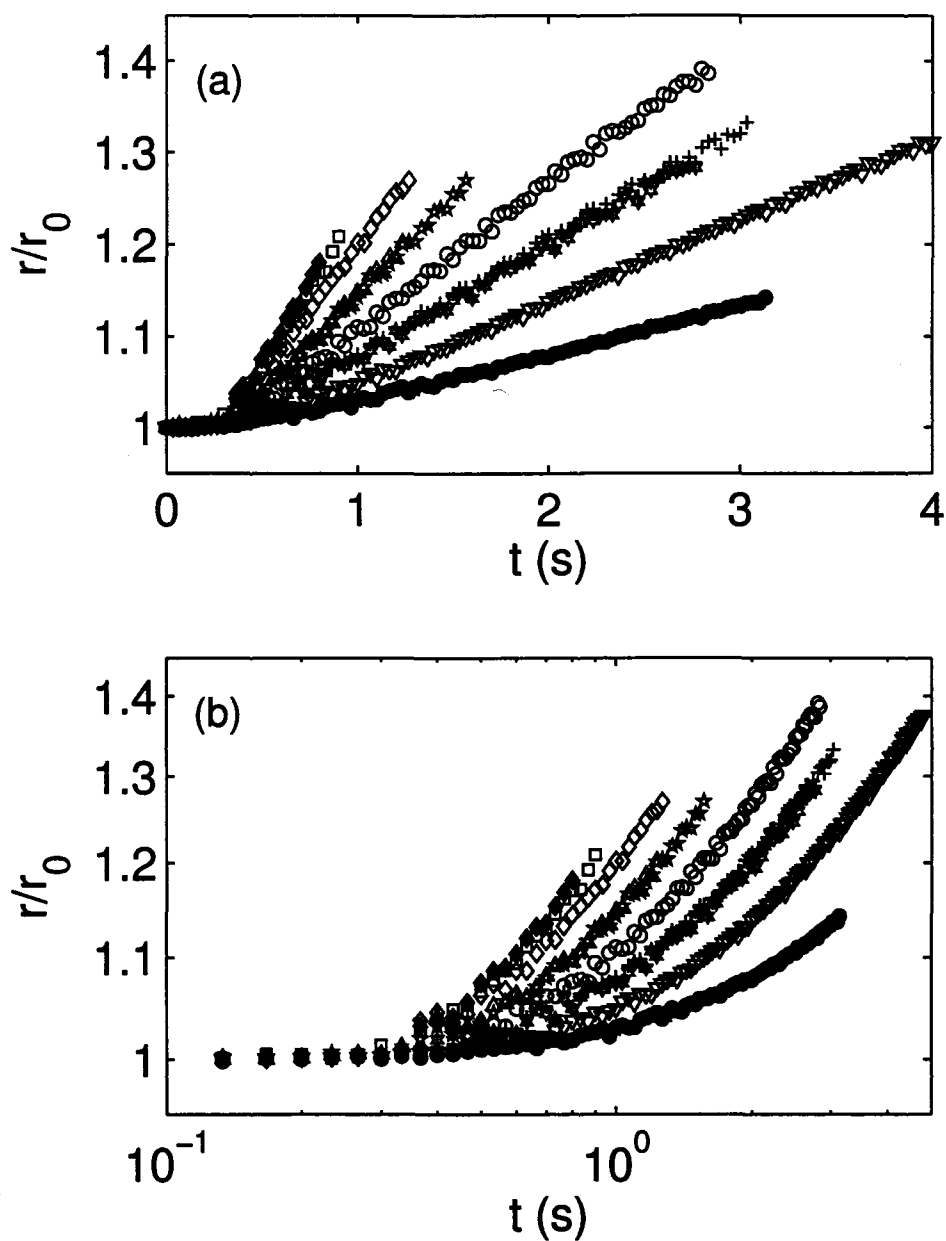


Figure 5.2: Spreading of drops of volume $V = 100 \mu\text{l}$. (a) shows r/r_0 as a function of time for several drops of the same volume with angular velocities ω ranging from 26.3 rad/s to 57.8 rad/s, indicated by the different symbols. The higher slopes correspond to higher values of ω . (b) shows the same data with logarithmic axes.

longer times had a logarithmic slope greater than the predicted value of $1/4$.

The above discussion notwithstanding, Fig. 5.2(a) suggests that, over the limited range of times from the end of the period of slow growth until the onset of fingering, the radius of the drop is very well described by a linear function of time. The slopes of the $r(t)/r_0$ plots in this region are plotted in Fig. 5.4 as a function of V for two angular speeds and as a function of ω for two values of V . In both cases the dependence of the slope on the abscissa can be described by power laws: the slope is proportional to $V^{0.73 \pm 0.05}$ and to $\omega^{2.47 \pm 0.17}$. Overall we found that $r/r_0 = (1.64 \pm 0.10) \times 10^{-7} \omega^{2.47} V^{0.73} t$ in this regime, with ω in rad/s and V in μl .

To study the fingering instability that develops after the period of uniform spreading discussed above, we analyze the experimental images using a Fourier transform technique [3, 24, 25]. The perimeter of the drop $r(\theta)$, where θ is the angular coordinate about the axis of rotation, is Fourier transformed to give the Fourier power spectrum as a function of the angular wave number n . n indicates the number of periods of the mode as θ is varied by 2π radians, that is, the number of maxima around the perimeter of the drop. A typical power spectrum is shown in Fig. 5.5(a). The large peak at $n = 1$ arises because the drop is slightly off-center despite our best efforts to position it accurately. Each of several hundred images from a given run is analyzed in this way, and the amplitude of the modes as a function of time t extracted. A typical result is shown in Fig. 5.5(b), where the amplitude of the $n = 7$ mode from the run shown in Fig. 5.5(a) is plotted against time. In this case, the amplitude is initially constant, then starts to grow at a time $t_c = 5.9$ s. The growth is initially well-described by an exponential function of the form $e^{\sigma t}$, but at later times the growth slows and the amplitude approaches a constant. The initial growth rate σ is calculated for each n from a fit to the amplitude data over the range of exponential growth. Fig. 5.6 shows σ as a function of n for the run shown in Figs. 5.1 and 5.5. To

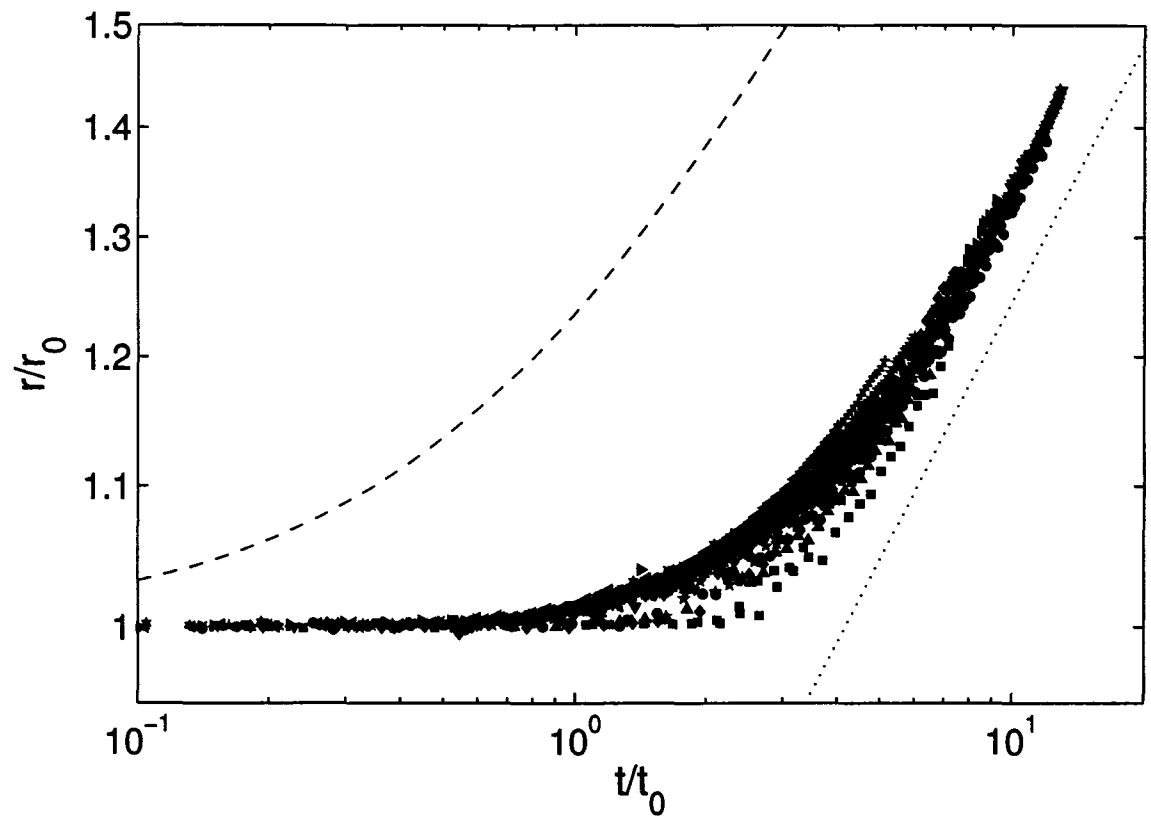


Figure 5.3: r/r_0 plotted as a function of scaled time, t/t_0 , where t_0 is defined in the text. 23 different data sets are shown, covering a range of volumes and angular speeds. The dashed line is the prediction of Eq. 5.2, and the dotted line is a 1/4-power law plotted for comparison.

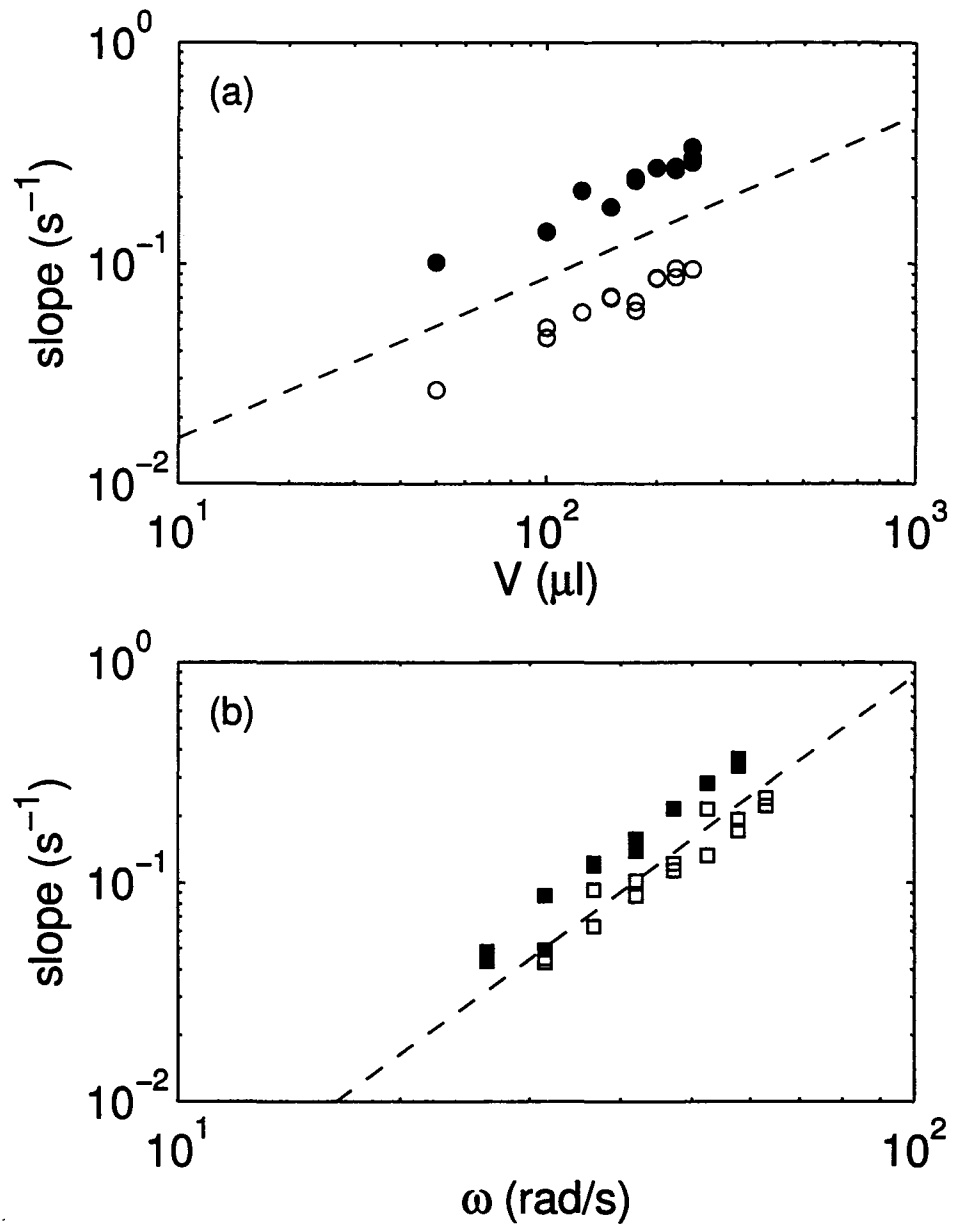


Figure 5.4: The slope of the apparently linear region of the spreading data $r(t)/r_0$ vs. t shown in Fig. 5.2 plotted as a function of volume (a) and angular speed (b). In (a), the open circles are for $\omega = 26.3$ rad/s, the solid circles for $\omega = 42.0$ rad/s, and the dashed line is a power law with exponent 0.73. In (b) the open squares are for $V = 50 \mu\text{l}$, the solid squares for $V = 100 \mu\text{l}$, and the dashed line is a power law with an exponent 2.47.

reduce the noise, the plotted growth rates have been averaged over the modes $n - 1$, n , and $n + 1$, but substantial scatter remains, particularly at higher n . Nonetheless it is evident that σ is positive for a range of n and becomes negative at high n , as expected since surface tension acts to stabilize modes at high n . In this particular case σ is a maximum for $n = 7$. This corresponds with the number of fingers seen to develop in Fig. 5.1 at early times.

Figure 5.7(a) shows the growth rate σ as a function of ω , while Fig. 5.7(b) shows σ as a function of V . σ increases with both angular speed and volume. The dependence on ω is well described by a power law with an exponent of 3.41 ± 0.01 , while the volume dependence is linear. Combining these, our results give $\sigma = (3.4 \pm 0.1) \times 10^{-8} V \omega^{3.41}$, where V is in μl and ω in rad/s . To get the growth rate in nondimensional form, we scale σ by the time scale ℓ/u_0 , where we take u_0 as the radial speed of the perimeter of the drop at $t = t_c$. The scaled growth rates are plotted in Fig. 5.8 and, within the experimental scatter, cluster around a mean value of 0.43 ± 0.16 , in excellent agreement with the theoretical predictions of Ref. [4] and with previous experiments on spin coating [3].

The radius r_c at which fingers begin to form is plotted against the drop volume and angular speed in Fig. 5.9. For a given V , r_c is independent of ω over the range of angular speeds studied, having average values of 0.0090 ± 0.0008 m for $V = 50 \mu\text{l}$ and 0.0118 ± 0.0009 m for $V = 100 \mu\text{l}$. r_c increases with V as $V^{0.36 \pm 0.02}$, consistent with the $V^{1/3}$ dependence one might expect from simple dimensional considerations.

The number of fingers n that form at the instability is shown as a function of volume for two values of ω in Fig. 5.10 and as a function of speed for $V = 50$ and $100 \mu\text{l}$ in Fig. 5.11. While there is some scatter in our data, our results show a systematic increase in n with both ω and V over the range covered by our experiments. In fact our experimental results are in quantitative agreement with Eq. (5.4): The dashed

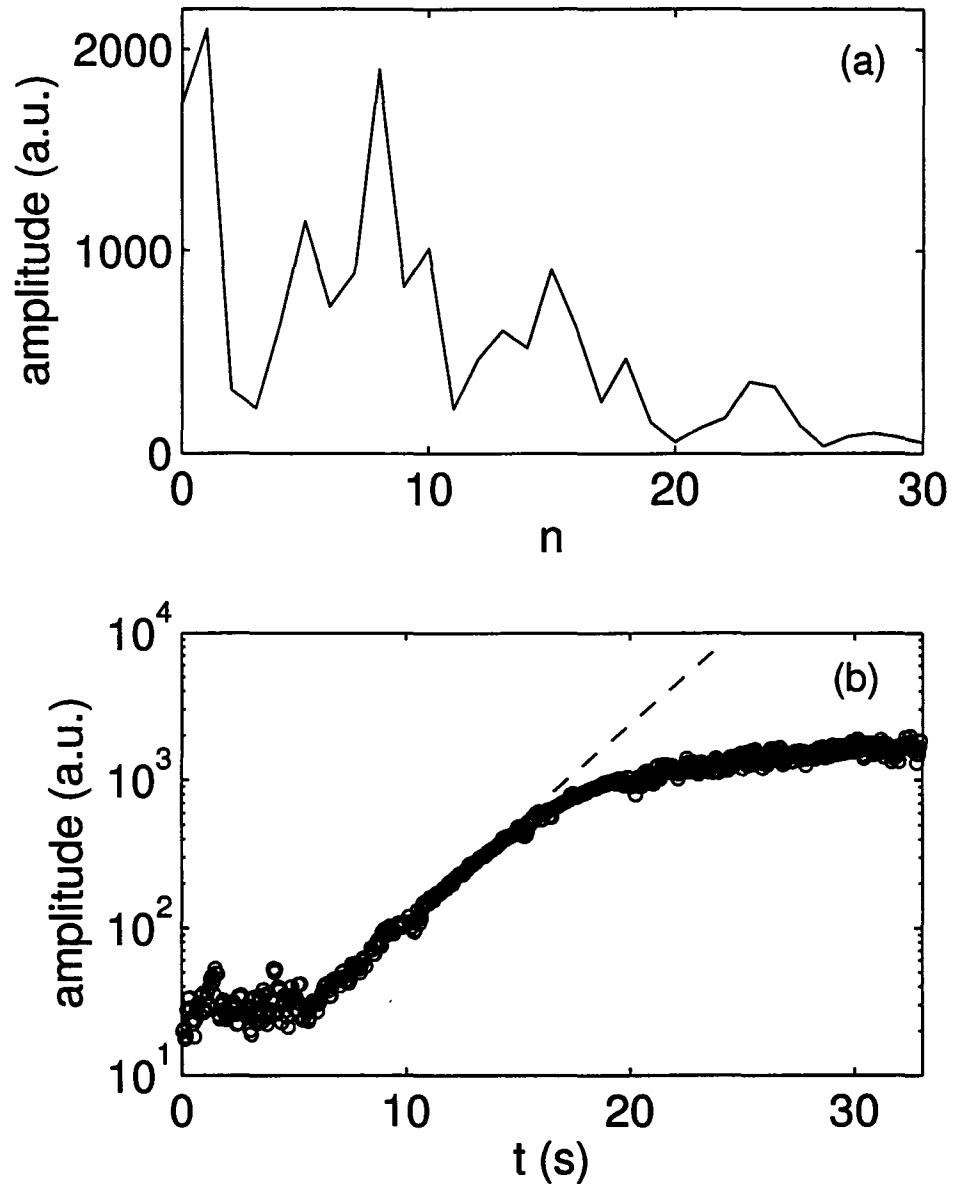


Figure 5.5: (a) The Fourier power spectrum of the perimeter of a drop with $V = 50\mu\text{l}$ a time $t = 21.45$ s after the start of spinning at $\omega = 36.8 \text{ s}^{-1}$. n is the azimuthal wave-number. (b) The Fourier power of the fastest growing mode at $n = 7$ for the same run as in (a). The onset time of the fingering instability t_c is indicated by the arrow, and the dashed line is a fit to an exponential growth law at early times after the onset.

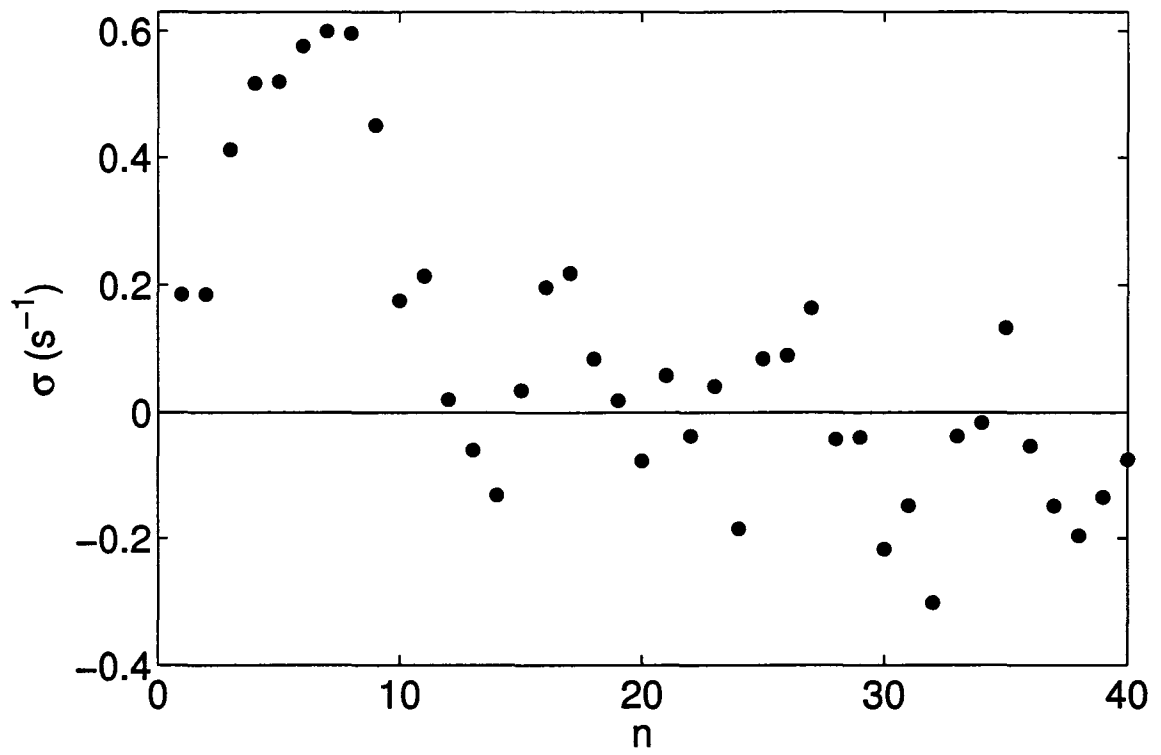


Figure 5.6: The exponential growth rate σ as a function of mode number n for the run of Fig. 5.5.

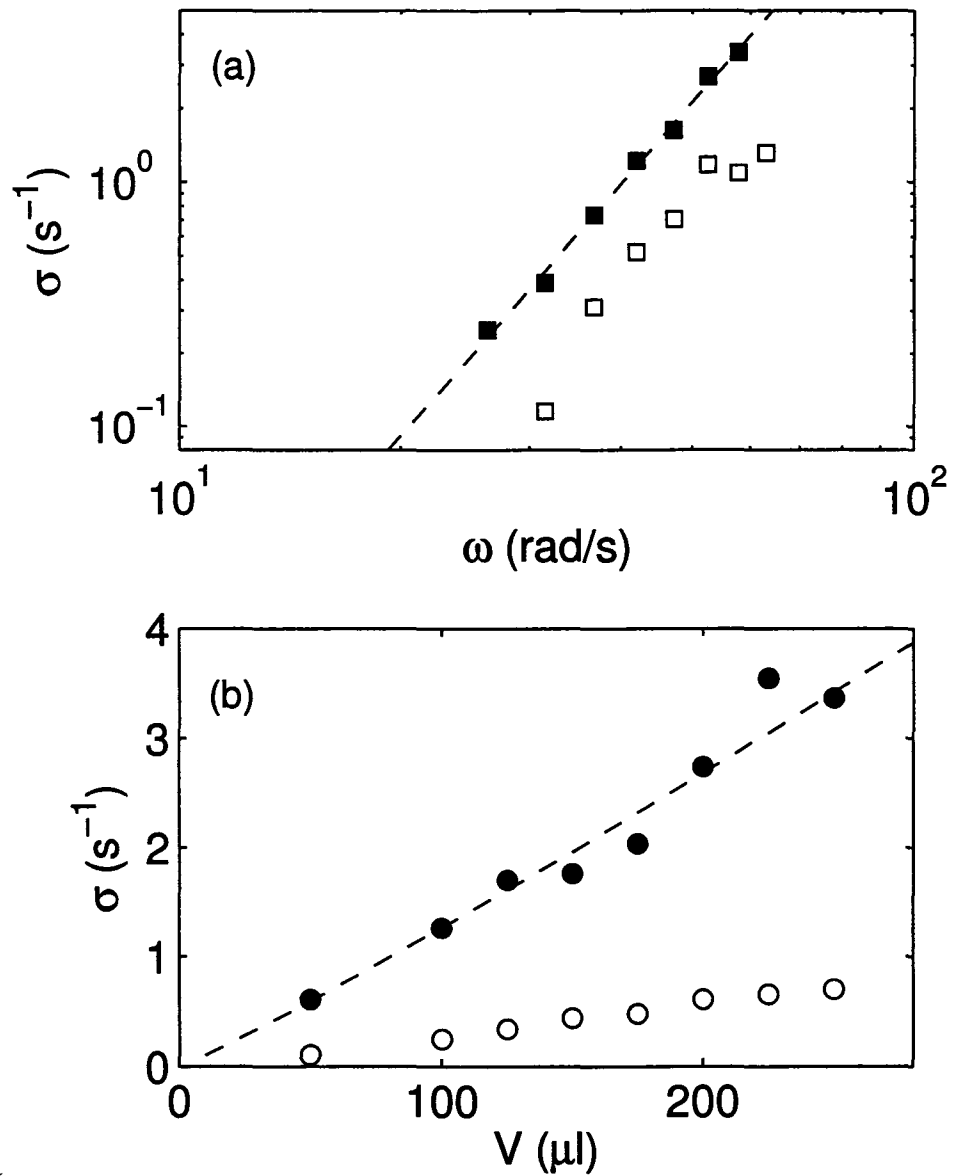


Figure 5.7: The growth rate σ of the fingers plotted against ω in (a) and against volume V in (b). In (a) the open squares are for $V = 50 \mu\text{l}$, the solid squares for $V = 100 \mu\text{l}$, and the dashed line is a power law fit to the data for $V = 100 \mu\text{l}$. In (b), the open circles are for $\omega = 26.3 \text{ rad/s}$, the solid circles for $\omega = 42.0 \text{ rad/s}$, and the dashed line is a straight line fit to the higher ω data.

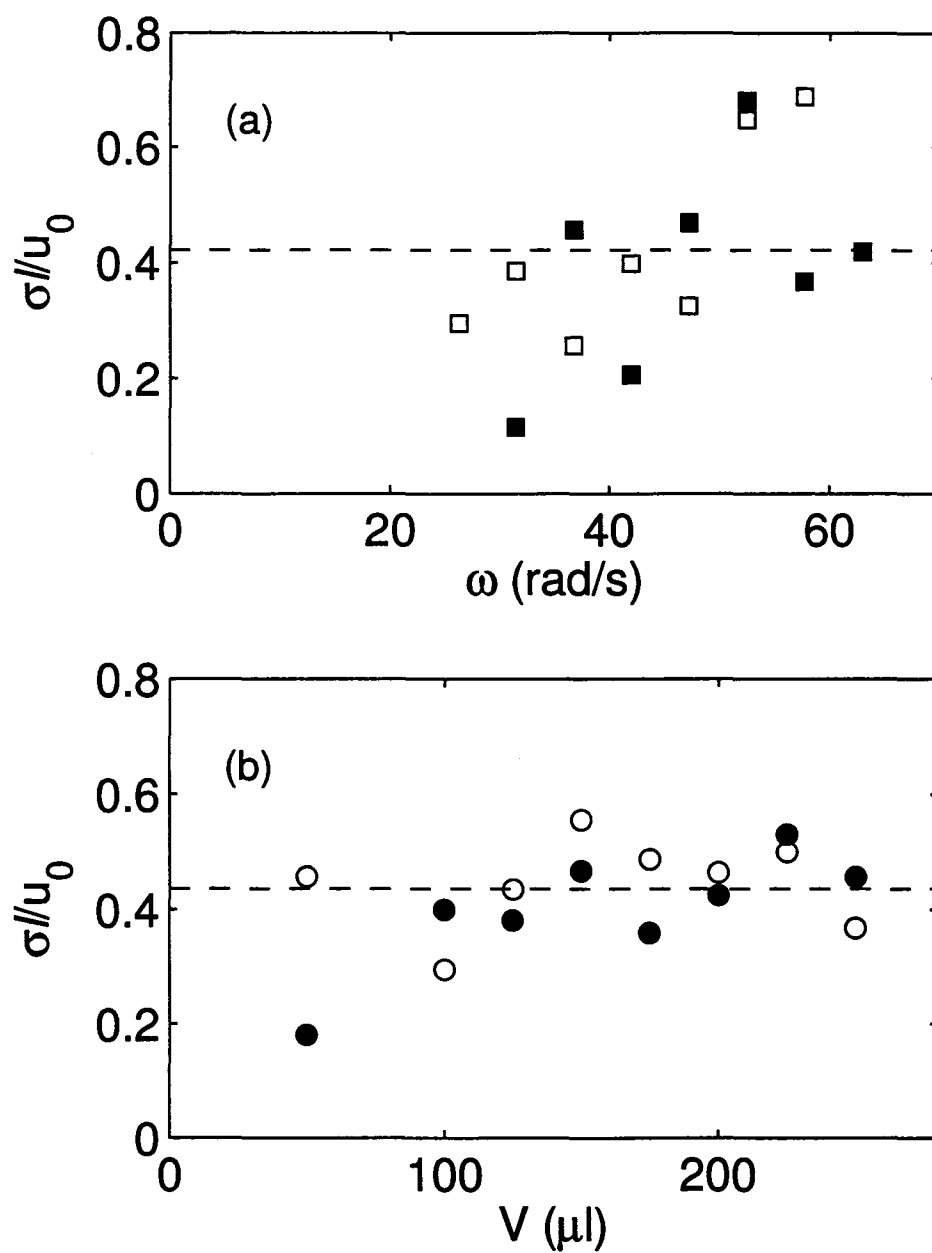


Figure 5.8: The scaled growth rate plotted as a function of ω in (a) and against V in (b). The dashed line is the mean value in each case. The experimental parameters and symbols are the same as in the previous figure.

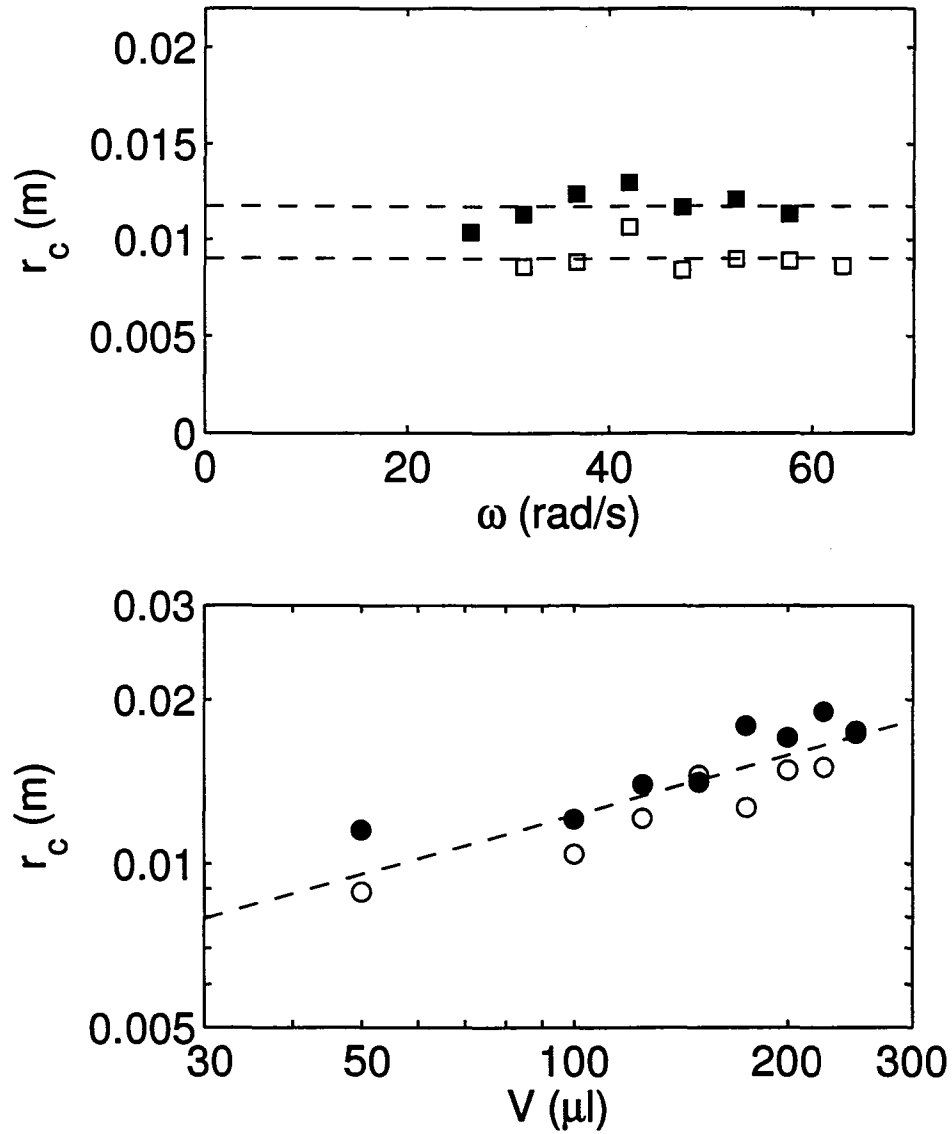


Figure 5.9: The critical radius r_c as a function of ω (a) and as a function of V (b). In (a), the open squares are for $V = 50 \mu\text{l}$ and solid squares for $V = 100 \mu\text{l}$. In (b), the open circles are for $\omega = 26.3 \text{ rad/s}$ and solid circles for $\omega = 42.0 \text{ rad/s}$. The two dashed lines in (a) show the average values of the data and in (b) the dashed line is a fit to all of the data.

lines in Figs. 5.10 and 5.11 are the theoretical predictions, calculated using the fits to our measured values of r_c described in the previous paragraph. There are no free parameters, and, within the scatter of our data, the agreement is excellent. The insets to Figs. 5.10 and 5.11 show the ratio of the predicted n values to the experimental results, determined using the individual r_c values rather than the fits. These ratios are all close to 1, again indicating the very good agreement between our measurements and the theoretical predictions. These results are in contrast to previous work, which suggested that the number of fingers was independent of both ω and V [3, 2]. This result led Fraysse and Homsy [3] to assume a particular functional form for r_c in order that the ω and V dependence in Eq. (5.4) would cancel out. Our measurements of r_c , shown in Fig. 5.9, do *not* follow the form assumed in Ref. [3], however.

5.5 Discussion

The time-dependence we observe for the spreading of the fluid drop before the onset of fingering agrees qualitatively with the predictions of Eq. (5.2), as shown in Fig.5.3, but the theoretical curve is significantly shifted from the experimental data. This can perhaps be explained by the theoretical assumption that the drop is cylindrical in shape, whereas in practice there is a significant, and time-dependent, radial variation in the height of the drop. The theoretical curve in Fig. 5.3 can be brought closer to the experimental data by a 60% change in the initial radius values, in effect changing the time scale t_0 by the same fraction. This shift is much larger than any experimental uncertainty, and seems larger than might be accounted for by the variation in drop shape. Fraysse and Homsy [3] found a similar result in their experiments, but required a shift in r_0 of only 10%-15% to bring theory and experiment into agreement. This persistent discrepancy between theory and experiment suggests that the scalings used

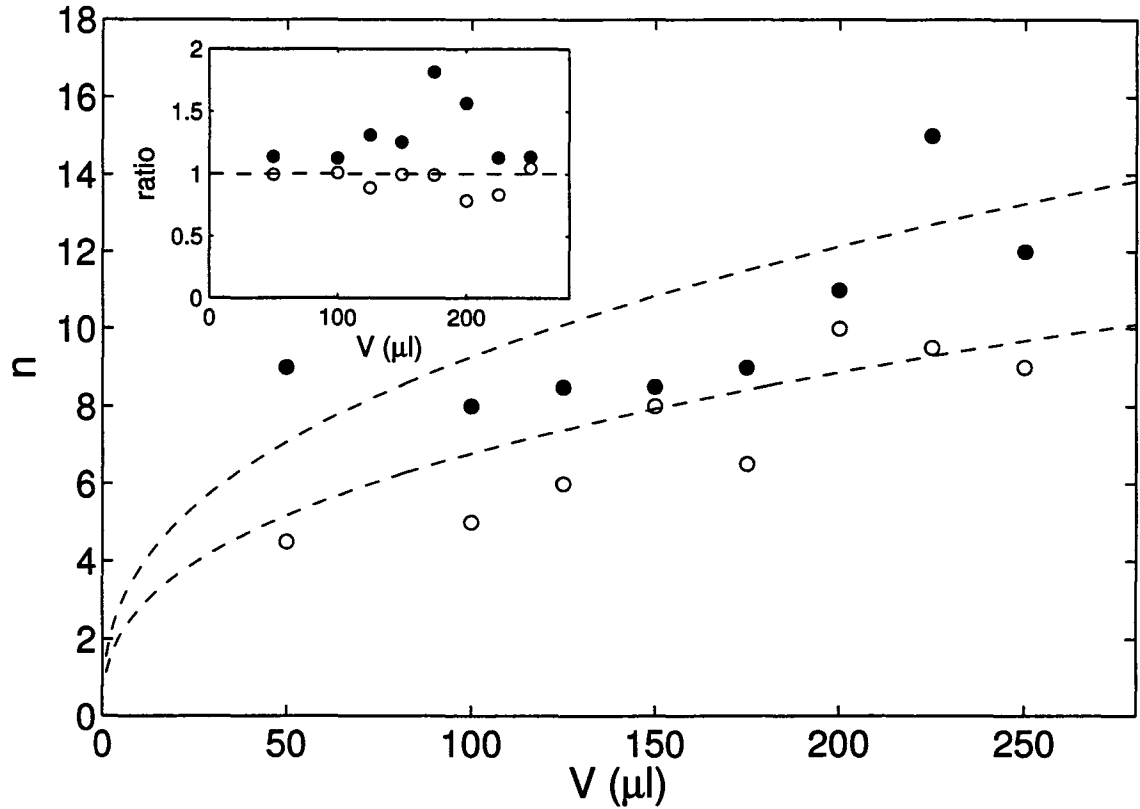


Figure 5.10: The number of fingers n as a function of V for two values of the rotation speed. The open circles are for $\omega = 26.3$ rad/s and the solid circles for $\omega = 42.0$ rad/s. The dashed lines are the predictions of the theoretical expression, Eq. 5.4, using the fits to the experimental data for the critical radius r_c shown in Fig. 5.9. There are no free parameters. The inset shows the ratio of the predicted number of fingers, calculated using the individual measured values of r_c , to the measured value of n .

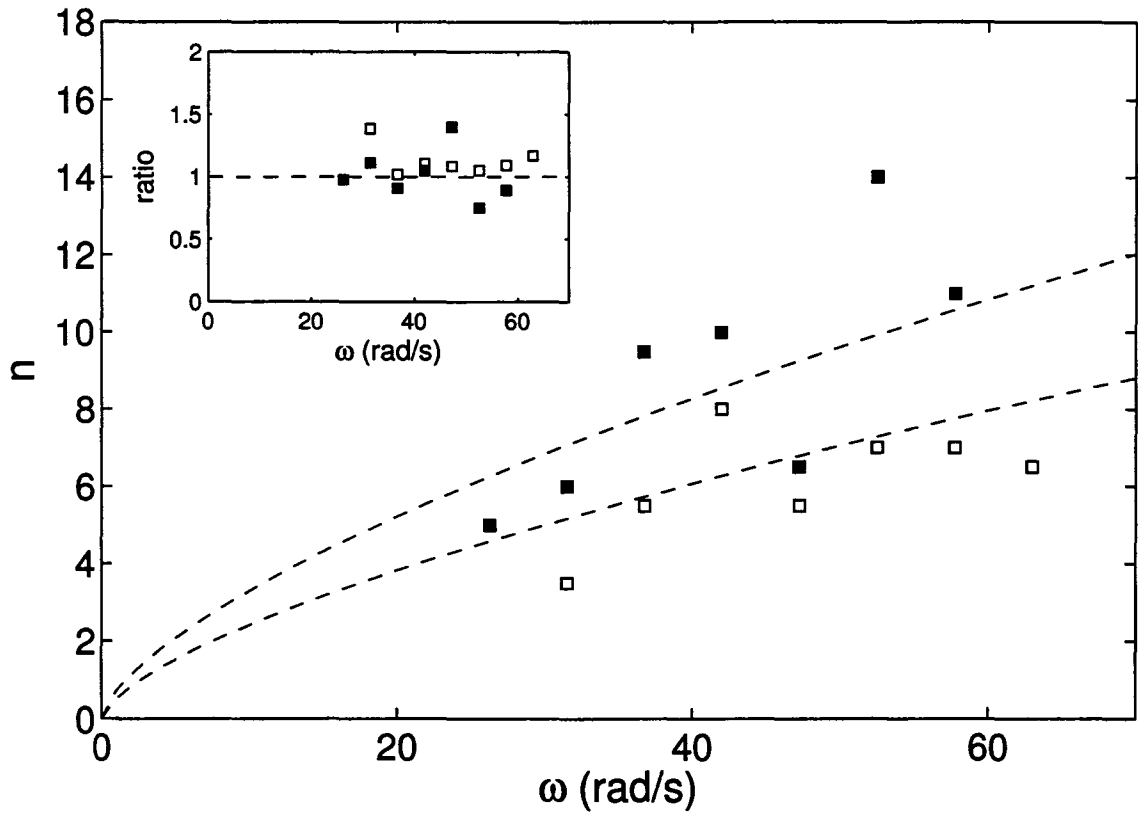


Figure 5.11: n as a function of ω for $V = 50 \mu\text{l}$ (open squares) and $V = 100 \mu\text{l}$ (solid squares). The dashed lines are again the predictions of Eq. 5.4, using the fits to the data for r_c shown in Fig. 5.9. The inset shows the ratio of the predicted number of fingers, calculated using the individual measured values of r_c , to the measured value of n .

in the derivation of Eq. (5.2) are inappropriate, as previously suggested in Ref. [3]. The alternative scaling introduced in [3], however, is based on an assumed dependence of the critical radius r_c on the experimental parameters which is clearly not supported by our data. We note that, in our experiments, ω is increasing to its set value over part of the initial period of slow spreading, although in all cases it is constant by the time the spreading rate starts to increase. This means that the time scale t_0 is in fact changing over the early part of the experiment, and may account in part for the discrepancy between experiment and theory.

Although Fig. 5.3 shows that at long times the spreading of the fluid drop approaches the expected $t^{1/4}$ power-law behavior, over the relatively short time during which the spreading occurs the data are well-represented by a linear increase of r_0 with time. The slope of this linear spreading, which has units of s^{-1} , is approximately proportional to $V^{3/4}\omega^{5/2}$. Dimensional analysis can be used to form an inverse time scale given by $V^{3/4}\omega^{5/2}\rho^{3/4}/\gamma^{3/4}$, which has the correct volume and angular velocity dependence, but the theoretical basis for such a time scale, if any, is not clear.

The growth rate σ of the fingers was found to be approximately proportional to $V\omega^{7/2}$. Scaling σ by ℓ/U_0 , as described in section 5.4 gives dimensionless growth rates that are constant within the experimental scatter and in excellent agreement with the predictions of lubrication theory [4]. Similarly good agreement was found in Ref. [3]. Since the length ℓ is proportional to H and assuming a cylindrical drop with volume $\sim Hr^2$, the scaling of the growth rates implies that the radial velocity $u_0 \sim \omega^{7/2}$ at the contact line at the onset of instability.

Fraysse and Homsy found the number of fingers n that appeared at the onset of the instability to be constant for the range of experimental parameters they studied [3]. Melo et al. [2] plotted their data as a function of the parameter $\beta = \gamma/\rho\omega^2V$ which, for our range of experimental parameters, is in the range $0.022 \leq \beta \leq 0.63$.

This is within the range in which Melo et al. [2] found both n and r_c to be constant. In contrast, we observe a weak but significant increase in n with both V and ω that is in quantitative agreement with the theoretical prediction, Eq. 5.4. We also find r_c to depend on V , as shown in Fig. 5.9. As noted, the functional form of r_c assumed in Ref. [3] to account for their observed constant n does not agree with our measurements. The good agreement between our results and the theory of Troian et al. [4], confirms the applicability of that work to a variety of mathematically-equivalent contact line instabilities.

Recent stability analyses of the spin coating problem have shown that for low values of the dimensionless parameter $S = \rho\omega^2V/\gamma\theta^3$, the $n = 1$ mode is always the most unstable mode [22, 21]. Here θ is the contact angle of the fluid on the substrate. This mode corresponds to a circular drop of fluid moving off-center. Our experiments involved a wetting fluid, so $\theta = 0$ and S is infinite, so we do not expect this result to apply to our system. We do find that the mode at $n = 1$ has a positive growth rate, as shown for one particular run in Fig.5.6, but it is never the most unstable mode. Typically the $n = 1$ mode has a fairly large initial amplitude, indicating that the drop is not perfectly centered at the start of the experiment, but the amplitude grows more slowly than several higher modes. Experiments with a non-wetting fluid at low S would provide a useful validation of this theoretical work.

5.6 Conclusion

We have studied the spin coating of a drop of silicone oil for a range of volumes and rotation speeds. The drop spread under the influence of the centrifugal force in qualitative agreement with theoretical predictions, but with a substantial shift in scaled time, suggesting that the scaling used in the theoretical expression is inappropriate.

Once the radius of the spreading drop became large enough, an instability developed at the contact line, leading to the formation of fingers around the perimeter. This fingering instability was observed for all experimental parameters studied. The number of fingers increased with both angular speed and drop volume while the scaled growth rate of the fingers was constant, both in excellent quantitative agreement with theoretical predictions.

Acknowledgements

This research was supported by the Natural Sciences and Engineering Council of Canada. We thank N. P. Chafe and A. Walsh for useful discussions.

Bibliography

- [1] A. G. Emslie, F. T. Bonner and L. G. Peck, *J. App. Phys.* **29**, 858 (1957).
- [2] F. Melo, J. F. Joanny, and S. Fauve, *Phys. Rev. Lett.* **63**, 1958 (1989).
- [3] N. Fraysse and G. M. Homsy, *Phys. Fluids*, **6**, 1491 (1994).
- [4] S. M. Troian, E. Herbolzheimer, S. A. Safran and J. F. Joanny, *Europhys. Lett.* **10**, 25 (1989).
- [5] H. E. Huppert. *Nature (U.K.)*, **300**, 427 (1982).
- [6] L. W. Schwartz, *Phys. Fluids A*, **1**, 443 (1989).
- [7] J. R. de Bruyn, *Phys. Rev. A*, **46**, R4500 (1992).
- [8] J. M. Jerrett and J. R. de Bruyn, *Phys. Fluids A*, **4**, 234 (1992).
- [9] J. R. de Bruyn, P. Habdas, and S. Kim, *Phys. Rev. E*, **66**, 031504-1 (2002).
- [10] S. M. Troian, X. L. Wu, and S. A. Safran, *Phys. Rev. Lett.* **62**, 1496 (1989).
- [11] S. M. Troian, E. Herbolzheimer, and S. A. Safran, *Phys. Rev. Lett.* **65**, 333 (1990).
- [12] M. A. Spaid and G. M. Homsy, *Phys. Fluids*, **4**, 823 (1997).

- [13] S. Togashi, T. Ohta, and H. Azuma, *J. Chem. Eng. Jpn.* **34**, 1402 (2001).
- [14] M.-W. Wang and F.-C. Chou, *J. Electrochem. Soc.* **148**, 283 (2001).
- [15] I. Veretennikov, A. Agarwal, A. Indeikina, and H.-C. Chang, *J. Colloid Interface Sci.* **215**, 425 (1999).
- [16] S. K. Wilson, R. Hunt, and B. R. Duffy, *J. Fluid Mech.* **413**, 65 (2000).
- [17] Y. D. Shikhmurzaev, *Phys. Fluids.* **9**, 266 (1997).
- [18] M. A. Spaid and G. M. Homsy, *Phys. Fluids*, **8**, 460 (1996).
- [19] I. S. McKinley, S. K. Wilson, and B. R. Duffy, *Phys. Fluids*, **11**, 30 (1999).
- [20] I. S. McKinley and S. K. Wilson, *Phys. Fluids*, **13**, 872 (2001).
- [21] I. S. McKinley and S. K. Wilson, *Phys. Fluids*, **14**, 133 (2002).
- [22] L. W. Schwartz and R. V. Roy, *Phys. Fluids*, **16**, 569 (2004).
- [23] W. Merzkirch, *Flow Visualization* (Academic, Orlando, 1987).
- [24] K. E. Holloway and J. R. de Bruyn, *Can. J. Phys.* **83**, 551 (2005).
- [25] K. E. Holloway and J. R. de Bruyn, *Can. J. Phys.*, to be published.

Chapter 6

Spreading and fingering in a yield-stress fluid during spin coating

6.1 Abstract

We study the spreading and fingering of small droplets of a yield-stress fluid subjected to a centrifugal force on a rotating substrate. The initial spreading of the droplets is found to be due to an elastic deformation of the fluid. We find that one or more fingers form at the contact line of the drop for large enough fluid volumes and rotation speeds. The fingering is qualitatively different from the contact line instability observed in other fluids, and appears to be a localized phenomenon that occurs when the stress at some point on the perimeter of the drop exceeds the yield stress.

6.2 Introduction

The process of spin coating involves depositing a volume of fluid on a substrate which is then rapidly rotated, forcing the fluid to spread due to the centrifugal force. Industrially, spin coating is used as a method of forming thin, uniform films. For example, this method is used to produce coatings on disks used for data storage [1]. In spin coating, as in other flows in which a contact line is driven by an external force, an instability can occur at the contact line of the fluid [2, 3, 4, 5, 6, 7, 8, 9, 10, 11] leading to the formation and growth of fingers of the fluid. In the case of spin coating, this can lead to uneven coating thicknesses. Fingering instabilities also occur during flow down an inclined plane [5, 6, 7, 8, 9] and spreading due to marangoni forces [10, 11].

Although fingering in Newtonian fluids has been studied extensively [2, 3, 4, 5, 6, 7, 8, 9, 10, 11, 12, 13, 14, 15, 16, 17, 18, 19], there have been rather few investigations of fingering in non-Newtonian fluids in general [4, 16, 12, 20, 21, 22, 23, 24] and yield stress fluids in particular [25, 26, 27, 28, 29, 30]. Non-Newtonian fluids differ from Newtonian fluids in that the viscosity η is not a constant, but rather is a function of the strain rate $\dot{\gamma}$. Yield-stress fluids flow when the stress on the fluid exceeds a threshold value referred to as the yield stress (or equivalently when the strain exceeds the a yield strain); below this value the fluid responds elastically to the applied stress, that is, it acts like a solid. In this paper we study the spreading and fingering of small droplets of Carbopol, a yield-stress polymer gel, subjected to a centrifugal force.

The properties of non-Newtonian fluids can lead to interesting pattern formation phenomena, in some cases very different from their Newtonian counterparts. For example, the injection of a solvent into a viscoelastic fluid within a thin cell can lead to fracture patterns [20, 21] similar to those seen in solids. Experiments in which air

was injected into a yield-stress fluid in a Hele-Shaw cell resulted in finger patterns with a high degree of branching [25]. Some other studies of fingering in non-Newtonian fluids are described in Refs. [4, 12, 16, 22, 26, 30].

Most previous studies of spin coating have involved Newtonian fluids, although spin coating using non-Newtonian fluids has also been studied to some extent. Fraysse and Homsy [4] experimentally studied the spreading of an elastic fluid drop and the fingering which occurred at the contact line during spin coating. Spaid and Homsy experimentally [16] and theoretically [12, 22] studied spreading and fingering with an elastic fluid. Borkar et al. [23] studied the spin coating of viscoelastic fluids experimentally and theoretically, but make no mention of a fingering instability. Acrivos et al. [24], following the work of Emslie et al. for Newtonian fluids [2], studied the evolution of fluid profiles for non-Newtonian fluids for power law fluids.

Spin coating in yield-stress fluids has been the topic of several previous numerical studies [27, 28, 29] which used different constitutive relations to model the yield-stress fluids. These studies found that an initially uniform film becomes nonuniform in height during the spinning process. The results of experiments performed with a yield-stress fluid agreed with these predictions [27]. Tabuteau et al. [30] studied the spreading of yield-stress fluids both theoretically and experimentally. They calculated a critical angular velocity ω_c for the fluidization of the material for different geometrical conditions. In their experiments, they studied the effect of substrate roughness, angular acceleration, yield stress, and sample size on the spreading. While their work focussed mainly on spreading, they also observed the formation of fingers around the perimeter of the sample at high enough ω . de Bruyn et al. [26] experimentally studied the fingering instability that occurred at the contact line of a yield-stress clay suspension flowing down an inclined plane. They compared the wavelength of the instability with the predictions of a model that took into account the yield-stress

behaviour of the material. Previous work showed that a sheet of yield-stress fluid on an inclined plane will not flow if either the angle of inclination or the thickness of the sheet is too small [31].

The remainder of this paper is organized as follows. The experimental details are presented in Section 6.3 and the results presented in Section 6.4. A discussion of the results follows in Section 6.5.

6.3 Experimental Method and Materials

The experimental apparatus is identical to that used in our previous experiments on spin coating in a Newtonian fluid [19]. The substrate is a transparent, circular sapphire plate 10 cm diameter. The plate is mounted on a bearing and can be rotated by a computer controlled microstepper motor. In the work described here, its angular velocity ω is varied in the range 10.5 – 63 rad/s. The acceleration of the plate is fixed at 168 rad/s². The plate reaches its final velocity in 0.15 s for the lowest speed used and 0.375 s for the highest speed used. Observations indicate that this acceleration time is much less than the time at which fingering begins. Prior to the start of a run, the plate is cleaned with warm, soapy water and rinsed in acetone. A length of fine tubing attached to a syringe pump is mounted in a vertical holder and, using two micrometer-driven translation stages, is precisely positioned above the center of the plate. The syringe pump is set to deposit a specified volume of fluid V in the range 0.2-1 ml on the substrate at a rate of 1 ml/min. The fluid drop is then allowed to relax for 5 min before rotation begins.

A shadowgraph optical system is used to visualize the flow. A collimated beam of light from a bright red LED was passed through the sample from below and focused onto a video camera mounted above the substrate. As Fig. 6.3 shows, this method

provides very clear visualization of the perimeter of the fluid drops. The contrast seen in the images within the fluid drop is due to variations in the height of the fluid which cause deflections of the light beam.

The experimental fluids used were aqueous solutions of Carbopol ETD 2050 [32], with concentrations $c = 0.2\%$ and 0.4% by weight. Carbopol is a commercial product used as a thickener, and is based on cross-linked linear polyacrylic acid chains. Carbopol dispersions behave as yield-stress fluids due to interactions among a network of micron-sized microgel particles [33]. The samples were prepared by slowly adding Carbopol powder to continuously stirred deionized water. Sodium hydroxide solution was then added to raise the pH to 6. The solutions were further mixed for several hours with a motorized mixer to completely homogenize the material. At the concentrations used here, the solutions were very weak gels with density equal to 1000 ± 5 kg/m³ at 22°C.

Rheometric characterization of the Carbopol samples was performed using an ARES RHS controlled-strain rheometer equipped with stainless steel concentric cylinders with inner and outer radii of 16 mm and 17 mm, respectively, and an immersed length of 34 mm. The sample temperature was maintained at 22°C by a temperature-controlled circulating fluid bath. The flow curve was measured by imposing a steady shear and recording the corresponding steady-state stress, starting at high shear rate and working downwards. The linear elastic and viscous moduli, G' and G'' respectively, were measured as a function of frequency by applying a small-amplitude oscillatory shear.

6.4 Results

6.4.1 Rheology

The rheometric measurements show that our Carbopol samples behave as yield-stress fluids with a small but measurable yield stress. Figure 6.1 shows the flow curves for the two concentrations of Carbopol. In both cases the data were well described by fits to a Herschel-Bulkley model,

$$\tau = \tau_o + K\dot{\gamma}^n, \quad (6.1)$$

where τ_o is the yield stress, K the consistency, and n a power law index. We find $\tau_o = 1.49 \pm 0.02$ Pa for $c = 0.2\%$ and $\tau_o = 1.74 \pm 0.16$ Pa for $c = 0.4\%$. For $\tau > \tau_o$, the samples are shear thinning, that is, the viscosity $\tau/\dot{\gamma}$ decreases with increasing strain rate. Figure 6.2 shows G' and G'' for the two concentrations. In both cases the elastic modulus is an order of magnitude larger than the viscous modulus and is nearly independent of frequency, as expected for a yield-stress gel.

6.4.2 Spreading and fingering

Fig. 6.3 shows a sequence of images from a run using Carbopol with $c = 0.4\%$, $\omega = 47.3$ rad/s, and $V = 0.5$ ml. The edge of the fluid drop is initially approximately circular as shown in Fig. 6.3(a). Since the Carbopol has a yield stress, there were inevitably small irregularities in its shape. These irregularities were not observed to have an effect on the subsequent flow. When the substrate is spun, the drop spreads by a small amount under the action of the centrifugal force. In most cases, a roll or ridge was observed to form around the perimeter of the drop, as previously observed for Newtonian fluids [3, 4, 19] and for yield-stress fluids [30]. This ridge can be seen

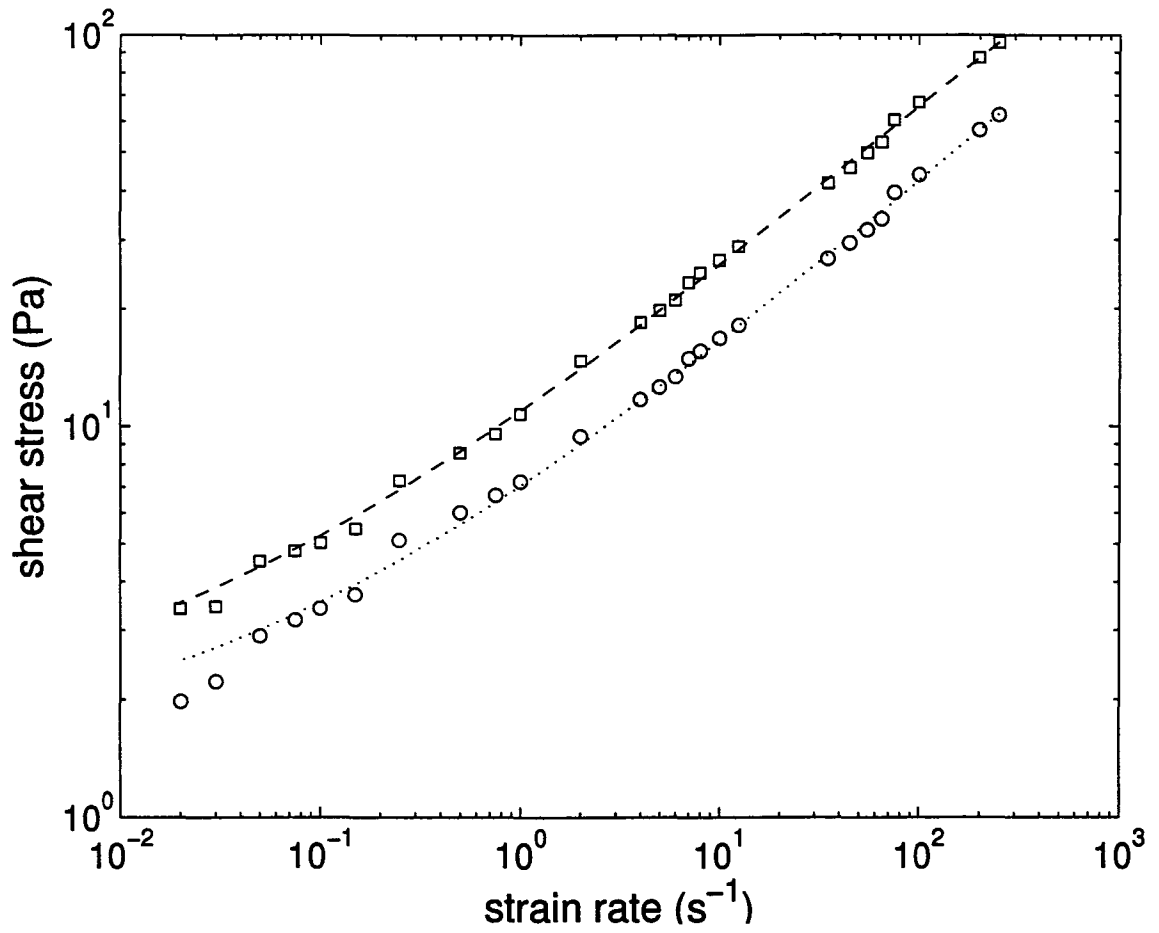


Figure 6.1: Mean measured flow curves for $c = 0.2\%$ (circles) and $c = 0.4\%$ (squares). The lines are fits to the data using the Herschel-Bulkley model, Eq. (6.1).

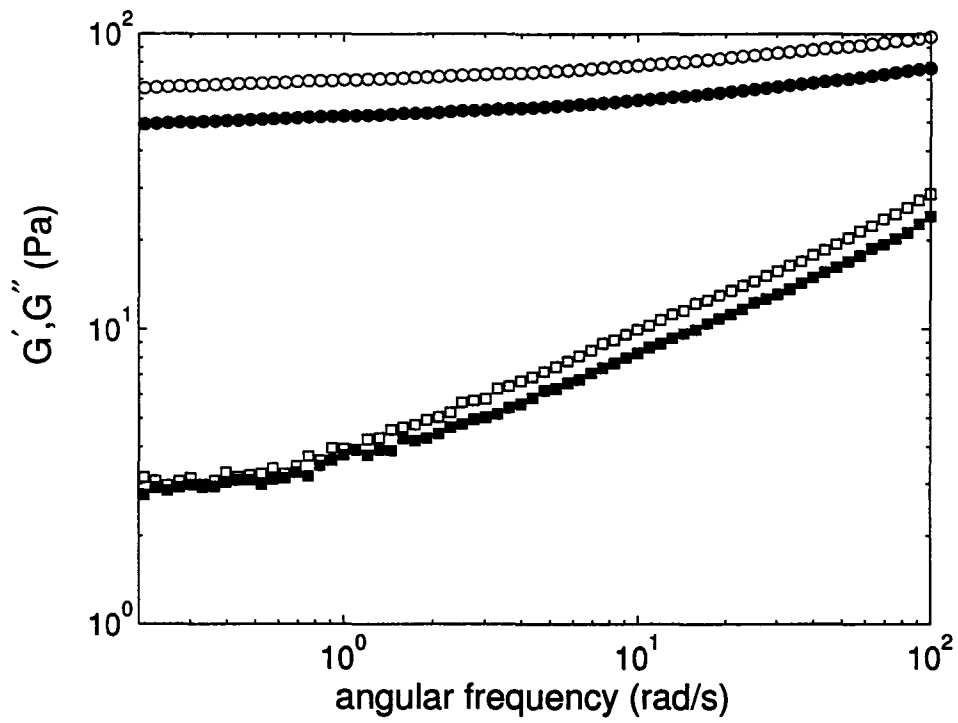


Figure 6.2: The elastic modulus G' (circles) and viscous modulus G'' (squares) as a function of frequency for 0.2% carbopol (solid symbols) and 0.4% carbopol (open symbols).

in Figs. 6.3 and 6.4 as the light region close to the perimeter. For high enough drop volume and angular speed, one or more fingers eventually form and grow at the perimeter of the drop, as shown in Fig. 6.3(b)-(d). In the run shown in Fig. 6.3, and indeed in the majority of runs, only one finger formed over the duration of the experiment. In some cases, however, more than one finger appeared, as illustrated in Fig. 6.4. In such cases, the fingers generally did not form simultaneously, nor were they equally spaced around the perimeter.

Each of the hundreds of experimental images from each run are analysed as follows. First, an edge detection algorithm is used to identify the perimeter of the Carbopol drop, then a circle is fitted to the edge of the drop [34]. The center of the fitted circle is not fixed but is allowed to vary depending on the shape of the drop. The radial strain on the drop is a measure of the spreading of the drop and is given by $\gamma_r = (r_f - r_{fo})/r_{fo}$, where r_f is the radius of the fitted circle and r_{fo} is its value at the start of the run. Figure 6.5 shows γ_r plotted as a function of time for a run in which the Carbopol drop did *not* finger. γ_r initially increases, then reaches a constant value $\gamma_{r,1}$. The data are, in general, well described by a simple exponential function approaching a constant value at long times with a time constant on the order of 0.01 s⁻¹. For $c = 0.2\%$, $0 \leq \gamma_{r,1} \leq 0.066$ and for $c = 0.4\%$, $0 \leq \gamma_{r,1} \leq 0.17$. $\gamma_r = 0.17$, then, is a lower limit of the yield strain for our Carbopol samples.

For drops for which fingering was observed, the spreading is linear at early times. Figure 6.6 shows γ_r for $c = 0.4\%$ and values of ω and V for which fingering was observed. γ_r is plotted as a function of time for $\gamma_r \leq 0.17$, the highest value of $\gamma_{r,1}$ measured for non-fingering drops. Figure 6.6(a) shows γ_r for a fixed drop volume and several values of ω , while Fig. 6.6(b) shows γ_r for fixed ω and several different values of V . In general γ_r is seen to increase more rapidly with increasing ω and with increasing V .

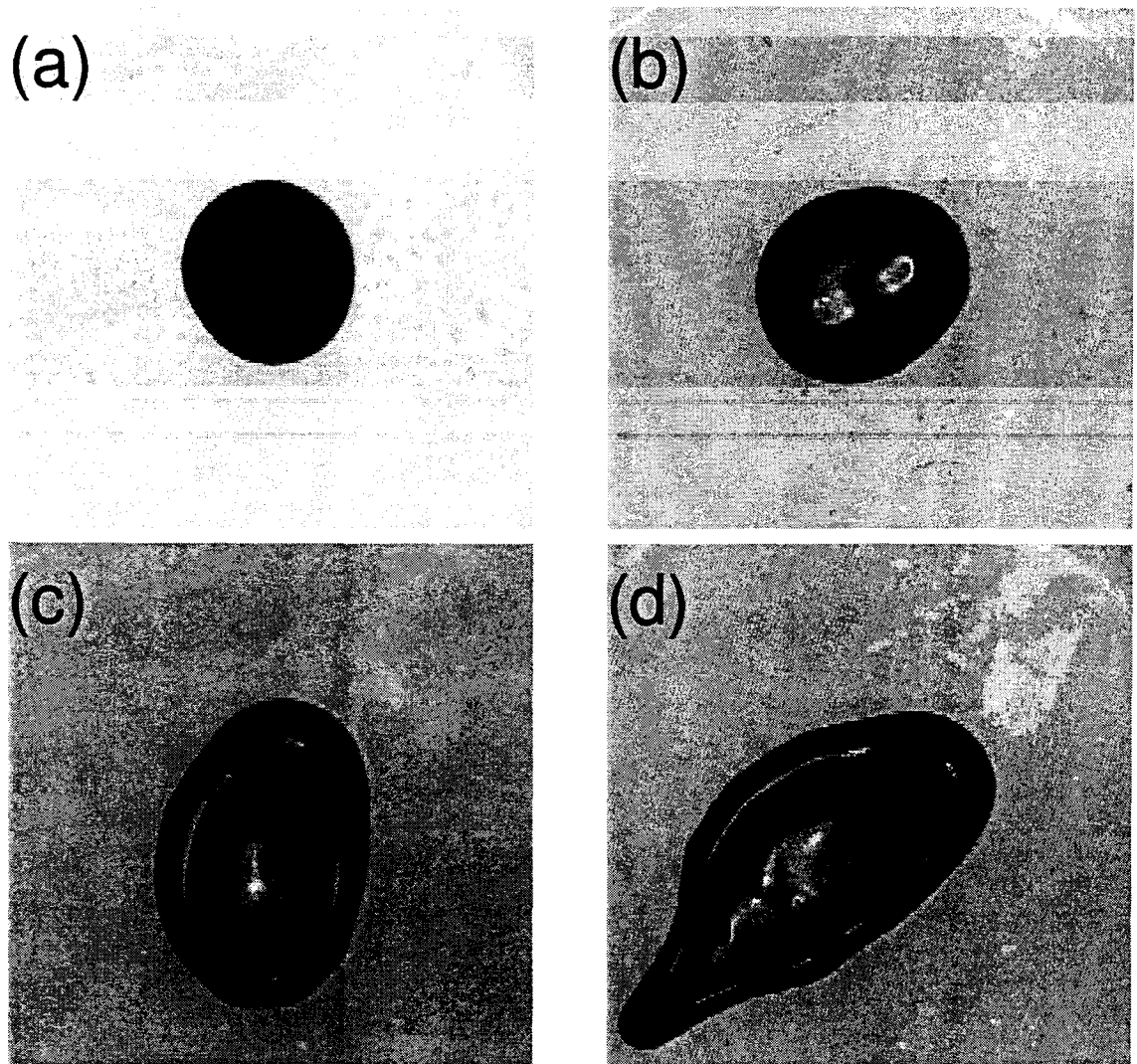


Figure 6.3: Images from a run with $c = 0.4\%$ showing the development of a finger as a function of time. For this run, $V = 0.5$ ml and $\omega = 47.3$ rad/s. Images were recorded at (a) 0.17 s, (b) 22.1 s, (c) 59.76 s, and (d) 77.34 s. The Carbopol drop appears dark, with light areas within the drop indicating variations in the drop's thickness. A ridge of fluid, indicated by a light region, can be seen close to the perimeter. The field of view is approximately 5.3 cm.

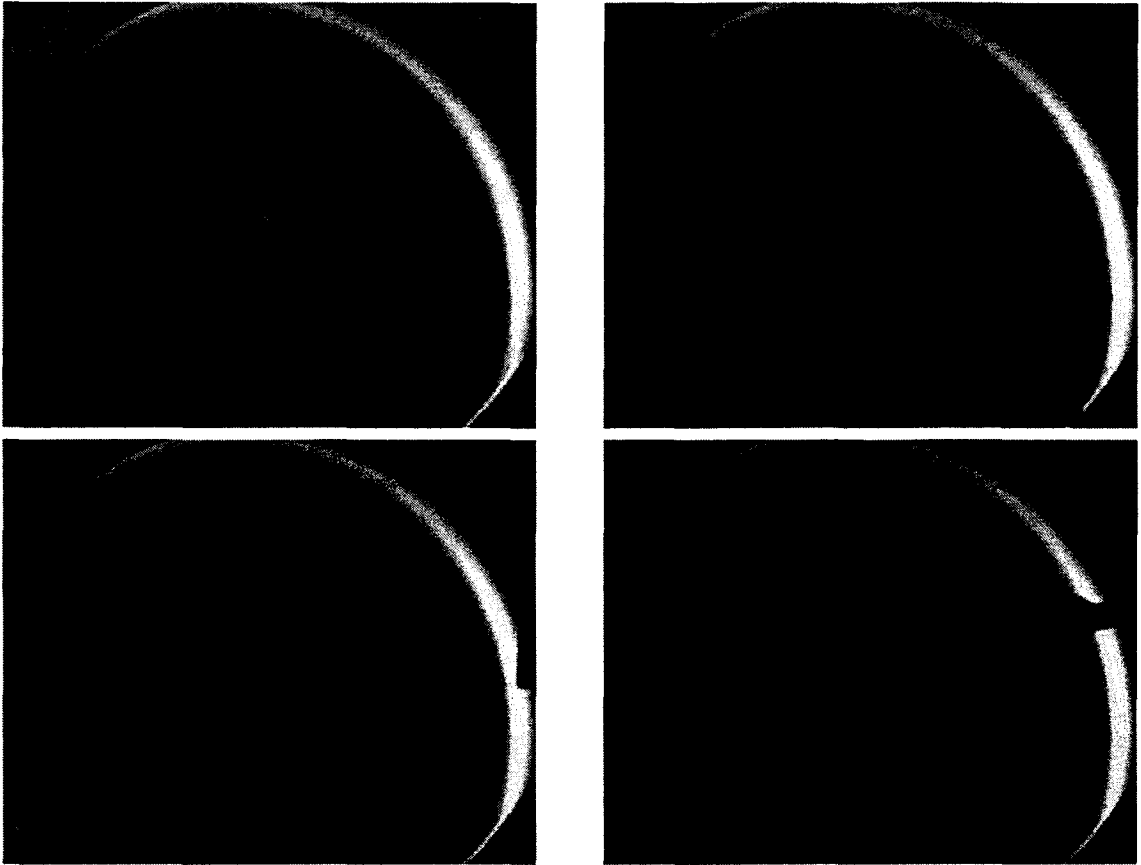


Figure 6.4: Images from a run with $c = 0.4\%$ showing the formation and growth of several fingers. Here $V = 1$ ml and $\omega = 63$ rad/s. Images were recorded at (a) 0.57 s, (b) 2.90 s, (c) 4.57 s, and (d) 11.23 s. The field of view is 8.2 cm.

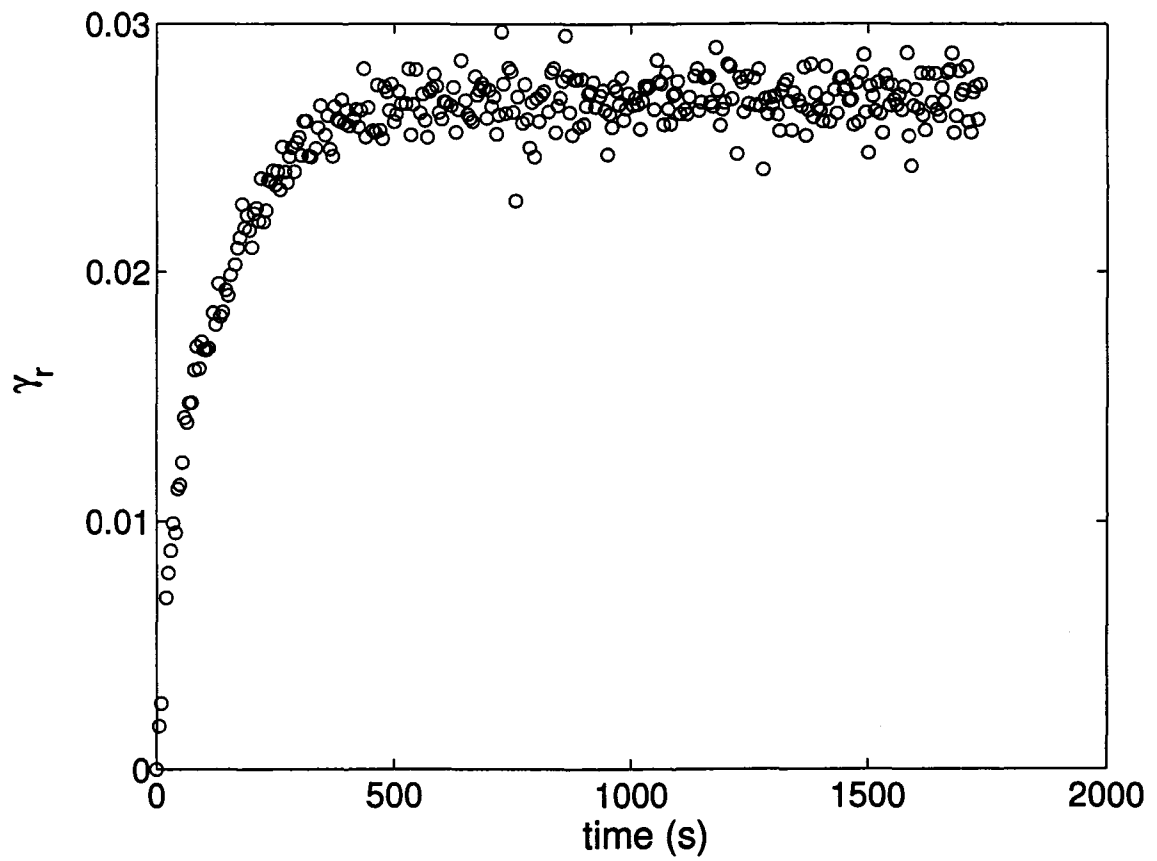


Figure 6.5: The radial strain γ_r plotted as a function of time for a Carbopol drop with $c = 0.4\%$ which was not observed to finger. Here $V = 0.5$ ml and $\omega = 21$ rad/s.

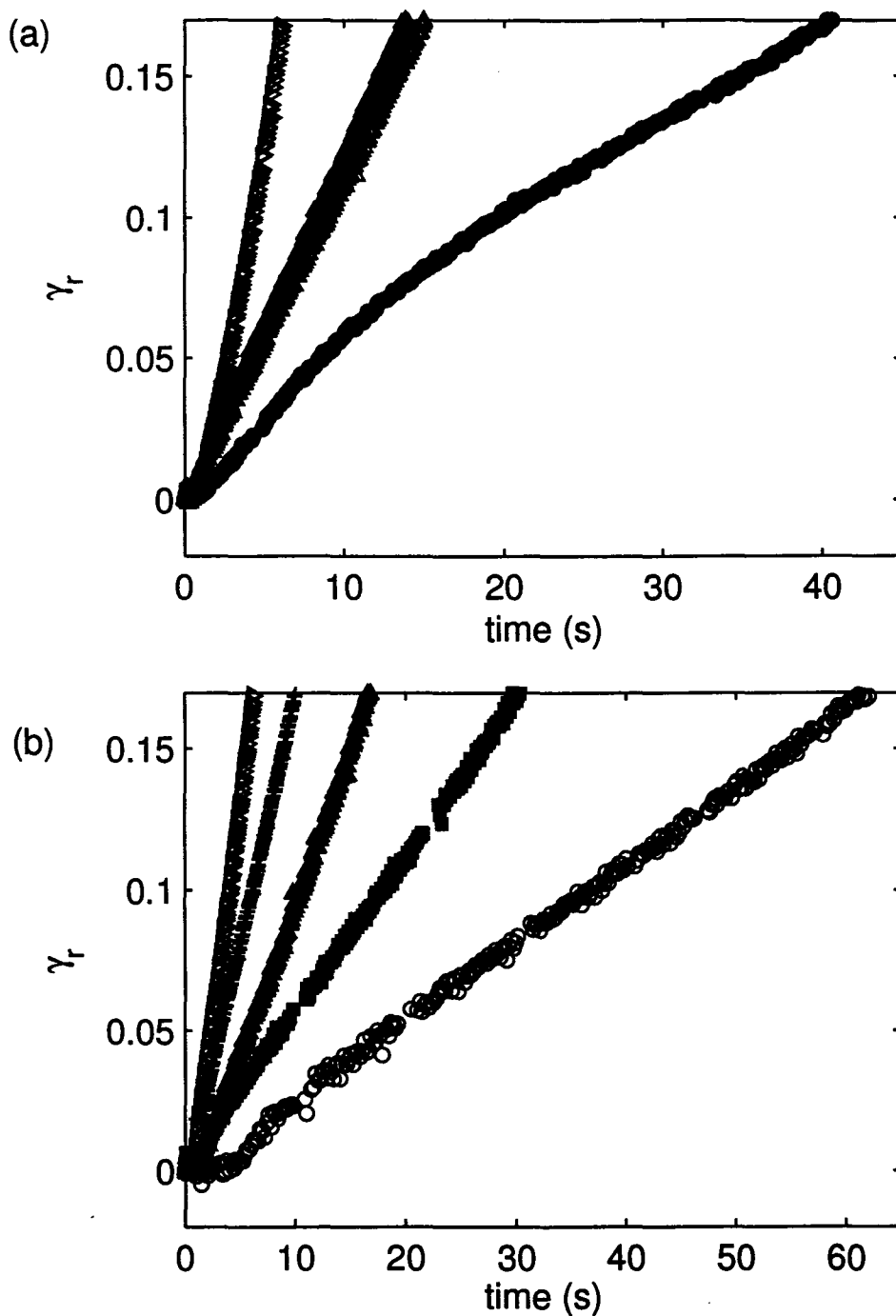


Figure 6.6: (a) The radial strain γ_r as a function of time for $V = 0.5$ ml. The different symbols represent runs with different ω . From top to bottom, $\omega = 63, 52.5, 57.8,$ and 42 rad/s. (b) γ_r as a function of time for $\omega = 52.5$ rad/s. The different symbols represent runs with different V . From top to bottom, $V = 0.75, 0.6, 0.4, 0.3,$ and 0.2 ml.

The image analysis described above also gives us r_{max} , the maximum distance from the center of the fitted circle to the drop edge. This is a measure of the length of the largest finger that forms. Fig. 6.7 is a plot of r_{max} as a function of time for one run. The slope of the plot increases with time, indicating that the finger tip grows faster with time. As r_{max} increases, the centrifugal force, and the stress at the finger tip, increase. The higher stress at the tip leads to a higher shear rate there, and so a decreased viscosity, allowing the fluid to flow more easily.

Fingers form only for high enough values of the angular speed and initial radius r_o , as shown for $c = 0.4\%$ in Fig. 6.8(a). The open circles indicate values of these parameters for which at least one finger was observed while the filled circles indicate conditions for which the fluid drop remained approximately circular. For $c = 0.2\%$ a similar boundary was obtained at lower values of ω and V .

6.5 Discussion

If a fluid does not possess a yield stress, drops of the fluid will flow for arbitrarily small ω when subjected to a centrifugal force. In our case, the Carbopol has a yield stress and so will not flow until the stress due to the centrifugal force exceeds the yield stress. In other words, when the applied strain on a yield-stress fluid is below a critical value of the strain, the fluid responds elastically to the applied stress. The maximum radial strain reached for the Carbopol drops which did not finger does not exceed 0.066 for $c = 0.2\%$ and 0.17 for $c = 0.4\%$. These strains are consistent with measured values of approximately 0.2 for the yield strain of other yield-stress fluids [35, 36]. The yield strain of our Carbopol samples can also be estimated from the rheological data presented in Figs. 6.1 and 6.2. Assuming the Carbopol is in the linear viscoelastic regime before it yields, the yield strain γ_o is found from the

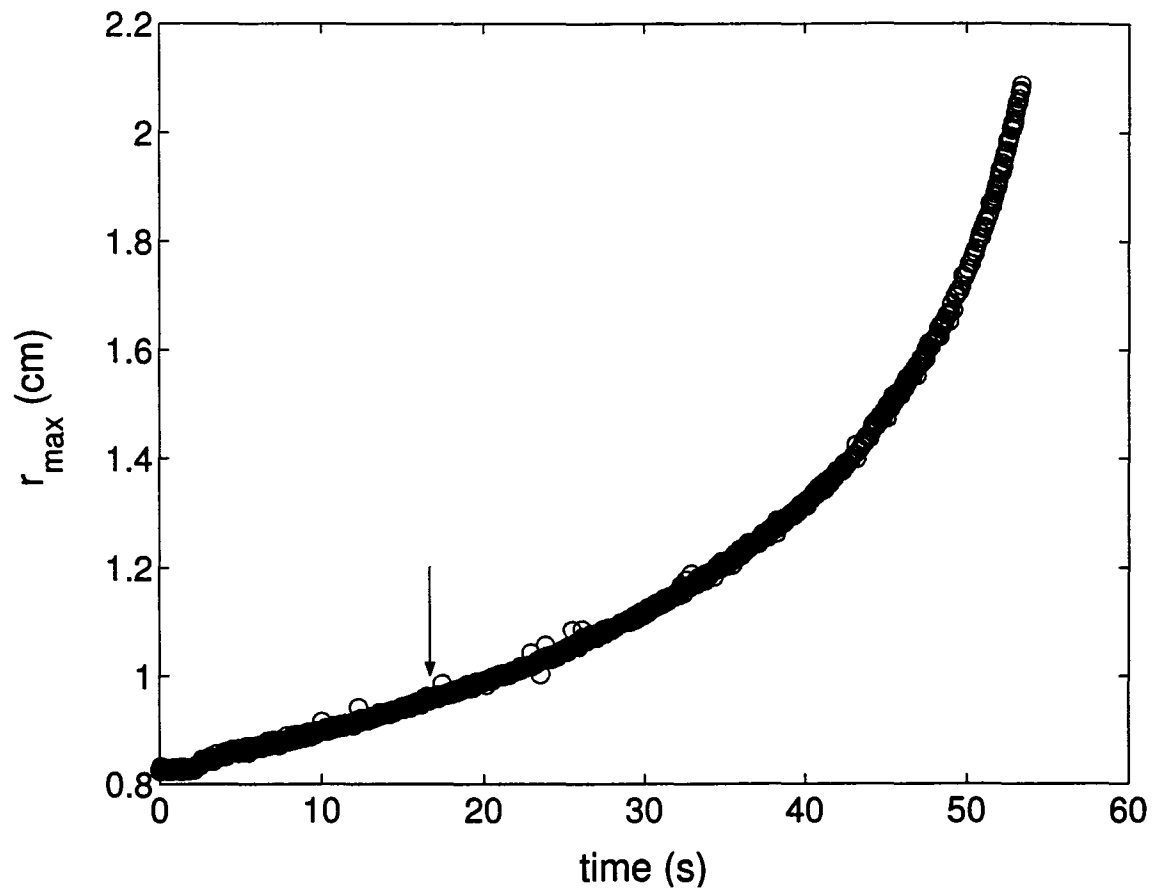


Figure 6.7: The maximum distance of the edge of the carbopol drop from the center of the fitted circle as a function of time for a run with $c = 0.4\%$, $V = 0.4$ ml, and $\omega = 52.5$ rad/s. The time at which the radial strain reaches 0.17 is indicated by the arrow.

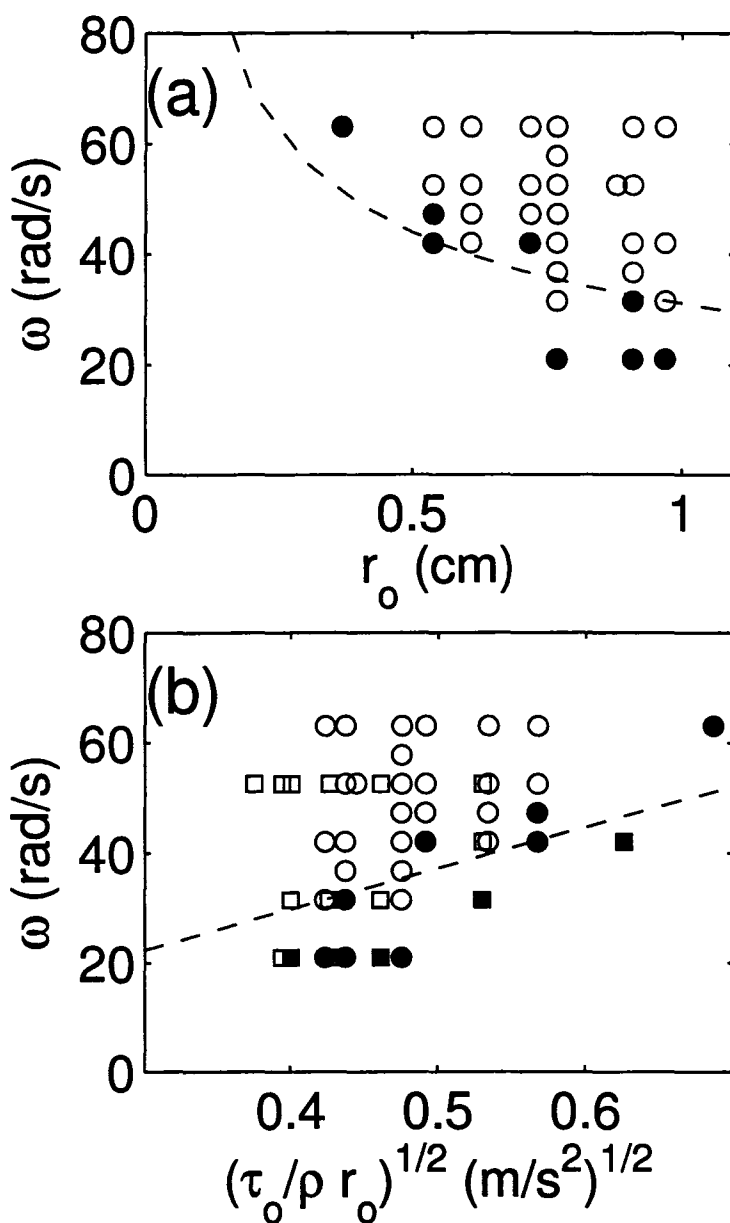


Figure 6.8: (a) Experimentally determined stability of $c = 0.4\%$. Open circles: fingers, closed circles: no fingers. The dashed line is the predicted stability boundary given by Eq. (6.2), multiplied by a factor of 2. (b) ω versus $\sqrt{\tau_o/\rho r_o}$ for $c = 0.2\%$ (squares) and 0.4% (circles). The open symbols correspond to parameters for which a finger(s) was seen while the solid symbols correspond to parameters for which a finger(s) was not seen. The dashed line shows the prediction of Eq. (6.2) with $h_o = 0.18$ mm.

relation $\tau_o = G'(0)\gamma_o$ [35], where τ_o is the yield stress and $G'(0)$ is the zero frequency elastic modulus. This gives $\gamma_o = 0.02$ for $c = 0.2\%$ and $\gamma_o = 0.024$ for $c = 0.4\%$, somewhat lower than the maximum strains observed for the non-fingering drops. The difference may be due to aging of the Carbopol during the time it sits on the plate before spinning (although aging is not expected to be important for Carbopol) or it may indicate that evaporation from the surface of the small droplets affects the material properties over the time scale of the experiments.

As the drop spreads, a ridge forms close to the edge of the drop. Although in previous experiments, fingering resulted from an instability of a similar ridge [3, 4, 19, 30], the fingering observed in the present case appears to be due to a different mechanism. For most of the experimental runs only a single finger formed. When more than one finger formed, the fingers did not form simultaneously, nor were they equally spaced around the perimeter of the drop. The growth of the finger tip increases with time, as shown in Fig. 6.7. In contrast, previous experiments with fluids without a yield stress [3, 4, 19] show an instability with a characteristic wavelength that occurs around the entire perimeter of the drop, leading to the formation of multiple fingers which initially grow exponentially. These differences suggest that fingering in our Carbopol drops is not the result of an instability, but rather is a localized effect.

A yield-stress fluid will only flow when the shear stress exceeds the yield stress. Tabuteau et al. [30] considered a cylindrical volume of yield-stress fluid with radius r_o and height $h_o \ll r_o$ on a rotating substrate. They found the critical angular velocity ω_c at which the material becomes fluidized to be

$$\omega_c = \sqrt{\frac{\tau_o}{\rho h_o r_o}}. \quad (6.2)$$

Since our drops are not cylindrical, we do not expect Eq. (6.2) to be completely

accurate for our experiments. r_o is determined from our experimental images. The height of the droplet h_o is harder to measure accurately, so we treat it as an adjustable parameter and use Eq. (6.2) to describe the stability boundary seen in Fig. 6.8(a). We obtain the curve shown as a dashed line in Fig. 6.8(a) with $h_o = 0.18$ mm, which seems to be a reasonable estimate of the height of the drop edge. There is reasonable agreement between our experimental stability boundary and the prediction of Eq. (6.2), suggesting that a finger forms only when the yield stress has been exceeded, that is, when the centrifugal force causes the stress at some point around the perimeter of the drop to become greater than the yield stress.

Figure 6.8(b) shows the stability diagram for both $c = 0.2\%$ (squares) and 0.4% (circles) plotted as ω versus $\sqrt{\tau_o/\rho r_o}$. When plotted in this manner, the stability boundaries for the two concentrations coincide. The dashed line is the prediction of Eq. (6.2) with $h_o = 0.18$ mm, which is again in reasonable agreement with the measured stability boundary.

Tabuteau et al. [30] performed spin coating experiments using much larger drop volumes. They observed an instability in which many equally-spaced fingers formed simultaneously, at an angular velocity well above the boundary given by Eq. (6.2). It seems probable that this is the same contact line fingering instability seen in Newtonian fluids [3, 4, 19]. Under our experimental conditions, however, local yielding preempts this instability.

6.6 Conclusion

We have studied spreading and fingering during spin coating for a yield stress fluid, Carbopol, for $c = 0.2\%$ and $c = 0.4\%$ and a range of rotation speeds and volumes. We found that non-fingering drops spread by only a small amount, after which the

spreading stopped. The rate at which spreading occurred for drops which fingered was found to increase with increasing V and increasing ω . We found that fingers form only for high enough drop volumes and rotation speeds. In contrast to what has been observed previously, fingers do not form collectively as the result of an instability of the contact line, but rather form individually when the stress due to the centrifugal force exceeds the yield stress locally.

Acknowledgements

This research has been supported by the National Sciences and Engineering Research of Canada.

Bibliography

- [1] TDK, <http://www.tdk.com/procommon/press/article.asp?site=prorecid=115>.
- [2] A. G. Emslie, F. T. Bonner and L. G. Peck, *J. App, Phys.* **29**, 858 (1957).
- [3] F. Melo, J. F. Joanny, and S. Fauve, *Phys. Rev. Lett.* **63**, 1958 (1989).
- [4] N. Fraysse and G. M. Homsy, *Phys. Fluids*, **6**, 1491 (1994).
- [5] S. M. Troian, E. Herbolzheimer, S. A. Safran and J. F. Joanny, *Europhys. Lett.* **10**, 25 (1989).
- [6] H. E. Huppert. *Nature (U.K.)*, **300**, 427 (1982).
- [7] L. W. Schwartz, *Phys. Fluids A*, **1**, 443 (1989).
- [8] J. R. de Bruyn, *Phys. Rev. A*, **46**, R4500 (1992).
- [9] J. M. Jerrett and J. R. de Bruyn, *Phys. Fluids A*, **4**, 234 (1992).
- [10] S. M. Troian, X. L. Wu, and S. A. Safran, *Phys. Rev. Lett.* **62**, 1496 (1989).
- [11] S. M. Troian, E. Herbolzheimer, and S. A. Safran, *Phys. Rev. Lett.* **65**, 333 (1990).
- [12] M. A. Spaid and G. M. Homsy, *Phys. Fluids*, **8**, 460 (1996).

- [13] S. K. Wilson, R. Hunt, and B. R. Duffy, *J. Fluid Mech.* **413**, 65 (2000).
- [14] I. S. McKinley, S. K. Wilson, and B. R. Duffy, *Phys. Fluids*, **11**, 30 (1999); I. S. McKinley and S. K. Wilson, *Phys. Fluids*, **13**, 872 (2001); *Phys. Fluids*, **14**, 133 (2002).
- [15] L. W. Schwartz and R. V. Roy, *Phys. Fluids*, **16**, 569 (2004).
- [16] M. A. Spaid and G. M. Homsy, *Phys. Fluids*, **4**, 823 (1997).
- [17] S. Togashi, T. Ohta, and H. Azuma, *J. Chem. Eng. Jpn.* **34**, 1402 (2001).
- [18] M.-W. Wang and F.-C. Chou, *J. Electrochem. Soc.* **148**, 283 (2001).
- [19] K. E. Holloway, P. Habdas, N. Semsarillar, K. Burfitt, and J. R. deBruyn, submitted to *Phys. Rev. E.* (2006).
- [20] E. Lemaire, P. Levitz, G. Daccord, and H. Van Damme, *Phys. Rev. Lett.* **67**, 2009 (1991).
- [21] H. Zhao and J. V. Maher, *Phys. Rev. E* **47**, 4278 (1993).
- [22] M. A. Spaid and G. M. Homsy, *J. Non-Newtonian Fluid Mech.* **55**, 249 (1994).
- [23] A. V. Borkar, J. A. Tsamopoulos, S. A. Gupta, and R. K. Gupta, *Phys. Fluids* **6**, 3539 (1994).
- [24] A. Acrivos, M. J. Shah, and E. E. Petersen, *J. App. Phys.* **31**, 963 (1960).
- [25] A. Lindner, P. Coussot, and D. Bonn, *Phys. Rev. Lett.* **85**, 314 (2000).
- [26] J. R. de Bruyn, P. Habdas, and S. Kim, *Phys. Rev. E*, **66**, 031504-1 (2002).
- [27] S. A. Jenekhe and S. B. Schuldt, *Chem. Eng. Commun.* **33**, 135 (1985).

- [28] S. L. Burgess and S. D. R. Wilson, *Phys. Fluids*, **8**, 2291 (1996).
- [29] J. A. Tsamopoulos, M. F. Chen, and A. V. Borkar, *Rheol. Acta.* **35**, 597 (1996).
- [30] H. Tabuteau, J. C. Baudez, and P. Coussot, to be published.
- [31] P. Coussot, *Mudflow Rheology and dynamics* (Balkema, Rotterdam, 1997).
- [32] Noveon technical data sheet #216 (2002);
<http://www.pharma.noveon.com/literature/tds/tds216.pdf>
- [33] J.O. Carnali and M.S. Naser, *Colloid Polym. Sci.*, **270**, 183-193 (1992).
- [34] I. Bicher, <http://www.mathworks.com/matlabcentral/fileexchange/loadFile.do?objectId=5>
(2004).
- [35] P. Coussot, H. Tabuteau, X. Chateau, L. Tocquer, and G. Ovarlez, to be published in *J. Rheol.* (2006).
- [36] H. Tabuteau, F. Oppong, J. R. de Bruyn, and P. Coussot, submitted to *Phys. Rev. Lett.* (2006).

Chapter 7

Summary

In this work, we have studied different fluid systems in which fingering occurs. We studied a variant of viscous fingering by injecting hot, less-viscous glycerine into colder, more-viscous glycerine in a Hele-Shaw cell. Fingering was observed at the boundary separating the hot and cold glycerine. We performed numerical simulations of this system using Fluent [1], a commercial fluid dynamics software program. We also studied spreading and fingering in spin coating using both a Newtonian and a non-Newtonian fluid. In both instances, fingering occurred at the contact line of the fluid.

7.1 Viscous fingering

We injected hot glycerine into colder glycerine within the narrow gap of a Hele-Shaw cell for different cell widths. The hot glycerine spreads radially outward, displacing the colder glycerine. When the injected glycerine reaches a critical radius r_c , the boundary between the hot and cold glycerine becomes unstable and fingers form. Our results indicate that this instability is similar to the fingering instability which occurs

between two miscible fluids. We found that λ increases as b increases, independent of cell temperature or inlet pressure. On average, we found $\lambda = (5.6 \pm 0.8)b$ for the two smallest cell widths, in agreement with previous miscible viscous fingering experiments [2, 3] and with the expectation that λ/b is a constant for high Peclet numbers [4, 5, 6, 7]. For the highest cell width used, λ/b decreased, perhaps due to increased three-dimensional flow within the cell. Fingering only occurred for high enough values of the inlet pressure and viscosity ratio, although the critical viscosity ratio observed in our experiments was higher than expected compared to previous experiments and theory [3, 8, 9].

As described in Chapters 3 and 4, we also performed numerical simulations of this system, but with some differences in the boundary conditions. The inlet velocity was specified in the simulations while the inlet pressure was specified in the experiments. The walls of the cell in the simulations were maintained at a constant temperature, while in the experiments the walls were kept cool by circulating coolant and so could heat up as the hot glycerine flowed through the cell.

The fingering pattern seen in the simulations was very similar to that seen in the experiments, although there were some quantitative differences. λ increased only slightly with b , but, as in the experiments, was independent of cell temperature and inlet velocity. λ/b is not a constant, contrary to expectations [4, 5, 6, 7]. The simulations show increased 3-D flow as b increases, which perhaps explains the decrease in λ/b for large b seen in the experiments. The growth rates of the fingers were higher in the simulations than in the experiments.

Fingering only occurred for high enough inlet velocities and viscosity ratios as in the experiments. The critical viscosity ratio found in the simulations agree with that from the experiments. Taking into account the cooling of the glycerine as it flows through the cell, the viscosity ratio at the location the instability was found to be

$M_c \approx 4$.

7.2 Spin coating

7.2.1 Newtonian fluid — silicone oil

We have studied the spin coating of a Newtonian fluid, silicone oil, for a range of rotation speeds and drop volumes. The drop is initially placed on a stationary substrate which is then rotated at a given angular speed. The drop initially spreads radially over the substrate. When the radius of the spreading drop exceeds a critical value r_c , the contact line becomes unstable and fingers of the silicone oil form. The pattern has a well-defined wavelength. We observed fingering for all the experimental parameters used in our experiments.

We studied the spreading of the drop prior to fingering and found that the radius of the drop scales as predicted by Emslie et al. [11], although the data are significantly shifted in scaled time from the prediction. The spreading approaches the predicted 1/4 power law at long times.

We found that the growth rate σ of the fingers increases with both the angular speed of the substrate and the drop volume. The scaled growth rate was found to be a constant, in good agreement with Troian's theory [12]. The number of fingers which form also agrees with the theoretical predictions [12, 13].

7.2.2 Non-Newtonian fluid — Carbopol

We have also studied spin coating using a yield-stress fluid, Carbopol. We found that fingers are only observed for high enough drop volumes and rotation speeds, in contrast to our experiments with silicone oil [15]. The mechanism leading to fingering

is different for Carbopol than for Newtonian fluids [12]. Fingering at the edge of the Carbopol drop appears to be a localized effect, instead of an instability which affects the entire contact line of the drop. In many of the experimental runs, we observe only a single finger; in the runs where we observed more than one finger, the fingers were not equally spaced around the perimeter of the drop.

The radius of the spreading drop prior to fingering is found not to follow the same scaling as Newtonian fluids, nor does the growth of the finger behave in the same manner. In contrast to silicone oil, for which we observed exponential growth of the fingers initially followed by slower growth at later times [15], we find that the Carbopol finger grows faster as time progresses.

We find that the boundary between fingering and no fingering in the ω - r_o diagram is well described by the theoretical expression for the critical angular velocity necessary for the start of flow in the lubrication regime obtained by Tabuteau et al. [16] This agreement implies that a finger forms at the edge of the advancing Carbopol drop when the stress at that point due to the centrifugal force exceeds the yield stress.

7.3 Future Work

The experiments and simulations on viscous fingering described in this thesis could be extended to other fluids with temperature-dependent viscosities.

Further study of the spin coating of Newtonian fluids could include using non-wetting fluids to investigate the $n = 1$ mode. Theoretically, this should be the most unstable mode for low values of the spin parameter $S = \rho\omega^2V/\gamma\theta^3$ [17, 18].

The spin coating of yield-stress fluids needs much further investigation. It would be informative to use different concentrations of Carbopol and also different yield-stress fluids to further study fingering. As well, a better theory is needed to describe

the onset of fingering for these fluids.

Bibliography

- [1] Fluent Inc. FLUENT Version 6.1.22 [computer program]. Fluent Inc., Lebanon, N.H. 2004.
- [2] L. Paterson, *Phys. Fluids* **28**, 26 (1985)
- [3] E. Lajeunesse, J. Martin, N. Rakotomalala, and D. Salin, *Phys. Rev. Lett.* **79**, 5254 (1997).
- [4] C.-W. Park, S. Gorell, and G. M. Homsy, *J. Fluid Mech.* **141**, 275 (1984).
- [5] T. Maxworthy, *Phys. Rev. A* **39**, 5863 (1989).
- [6] J. Fernandez, P. Kurowski, P. Petitjeans, and E. Meiburg, *J. Fluid Mech.* **451**, 239 (2002).
- [7] J. Fernandez, P. Kurowski, L. Limat, and P. Petitjeans, *Phys. Fluids* **13**, 3120 (2001).
- [8] E. Lajeunesse, J. Martin, N. Rakotomalala, D. Salin, and Y. C. Yortsos, *Phys. Fluids* **13**, 799 (2001).
- [9] D. Snyder and S. Tait, *J. Fluid Mech.* **369**, 1 (1998).
- [10] E. Lajeunesse, J. Martin, N. Rakotomalala, D. Salin, and Y. C. Yortsos, *J. Fluid Mech.* **398**, 299 (1999).

- [11] A. G. Emslie, F. T. Bonner and L. G. Peck, *J. App, Phys.* **29**, 858 (1957).
- [12] S. M. Troian, X. L. Wu, and S. A. Safran, *Phys. Rev. Lett.* **27**, 1496 (1989).
- [13] N. Fraysse and G. M. Homsy, *Phys. Fluids*, **6**, 1491 (1994).
- [14] F. Melo, J. F. Joanny, and S. Fauve, *Phys. Rev. Lett.* **63**, 1958 (1989).
- [15] K. E. Holloway, P. Habdas, N. Semsarillar, K. Burfitt, and J. R. de Bruyn, submitted to *Phys. Rev. E.* (2006).
- [16] H. Tabuteau, J. C. Baudez, and P. Coussot, to be published.
- [17] I. S. McKinley and S. K. Wilson, *Phys. Fluids*, **14**, 133 (2002).
- [18] L. W. Schwartz and R. V. Roy, *Phys. Fluids*, **16**, 569 (2004).

Appendix A

Thermoviscous Fingering

A.0.1 Introduction

Thermoviscous fingering is a fingering instability which may occur when a hot fluid with a temperature dependent viscosity enters a channel with cold walls. Although there are similarities, this instability is different from the viscous fingering instability described in Chapters 1, 3, and 4. Thermoviscous fingering requires the flow to be in a thermal steady state [6], while the system described in Chapters 3 and 4 is not. As well, the initial condition in our system is such that when the hot fluid is forced into the colder fluid, a Saffman-Taylor like fingering instability develops, precluding the growth of thermoviscous fingers. Thermoviscous fingering is believed to be important in magma flow [1]. As magma flows upwards through a crack in the Earth's crust, its flow is seen to become focused so that it emerges at the Earth's surface at isolated spots [1]. We devoted a significant amount of effort to experiments intended to study this instability, but, while suggestive, they were ultimately unsuccessful. Nonetheless, they will be described briefly in this Appendix.

A hot, less viscous fluid flowing between the cold walls of a channel loses heat to

the walls, causing the viscosity of the fluid to increase. Thermoviscous fingering then leads to the formation of fingers into which incoming glycerine is channeled since the fingers provide a path with lower resistance for the flow. This instability has been studied theoretically by Morris [2], Helfrich [3], and Wylie and Lister [4]. Helfrich [3] performed a two-dimensional linear stability analysis in which the relevant quantities were averaged in the cross-channel direction. He found that the existence of multiple flow rates for the along channel flow was necessary for instability. His results showed that for slow flows fingering was possible when the viscosity ratio $\beta_c = \mu_1(T_1)/\mu_2(T_2)$, where T_1 is the temperature of the walls of the channel, T_2 is the temperature of the fluid entering the cell, and $\mu_1(T_1)$ and $\mu_2(T_2)$ are the viscosities of the displaced and the displacing fluids, respectively, exceeded a critical value $\beta_c \approx 20$. He performed calculations for both constant pressure and constant flux inlet conditions.

Wylie and Lister [4] performed a three-dimensional linear stability analysis. They also found that multiple flow rates were necessary for fingering but found a critical viscosity ratio considerably higher than that found by Helfrich. The value of β_c was a function of the relationship used in the calculations. For a step function model where

$$\begin{aligned} \mu &= 1 & \text{for } T < \theta \\ \mu &= \beta & \text{for } T > \theta, \end{aligned} \tag{A.1}$$

β_c was found to be approximately 12. Here θ is a particular temperature. For an exponential viscosity model, $\beta_c \approx 120$.

Morris [2] also performed a three-dimensional stability analysis with results similar to Wylie and Lister — the necessity of multiple flow rates and a critical viscosity ratio. The critical viscosity ratio was higher than that found by Wylie and Lister. For an infinitely long channel Morris found $\beta_c = 324$. In addition, Morris showed that for

long channels the wavelength of the instability was comparable to the thermal entry length L_c , the distance traveled by the fluid in the along-channel direction in the time it takes heat to diffuse across the channel.

There have been rather few experimental studies of thermoviscous fingering. Wylie et al. [1] performed experiments by injecting heated Karo syrup into an empty Hele-Shaw cell similar to that described in the next section. They observed a fingering instability which over time evolved to a single finger. Whitehead and Helfrich [5] injected heated paraffin wax between the plates of a Hele-Shaw cell. In this case, fingering was observed well before the wax reached the edges of the cell and, again, by the end of the experiment, most of the flow was observed to be through only one finger.

A.0.2 Experiments

According to theory [2, 3, 4], the viscosity ratio required for thermoviscous fingering to occur is quite large. Glycerine was chosen as the experimental fluid because its viscosity increases dramatically with decreasing temperature, as described in Chapter 3.

A substantial amount of effort was spent in an attempt to observe and study this instability, but no unambiguous, reproducible results were obtained. Several versions of the apparatus were tried; the one that yielded the most promising results is shown in Fig. A.1. The apparatus consists of a Hele-Shaw cell, a constant flow rate pump, and a Pulnix ccd video camera interfaced to a computer used to capture images of the flow. The bottom plate of the Hele-Shaw cell is circular, made of aluminum, and is 45.7 cm in diameter and 1.27 cm thick. The upper plate is a plexiglas square 45.7 cm on a side and 1.27 cm thick. The plates are separated from each other by 12 spacers,

0.5 cm thick, and are clamped together to maintain the uniform spacing. The outer edge of the cell is open to the atmosphere except for the regions occupied by the spacers. The Hele-Shaw cell is placed on a platform which was carefully adjusted to be level. An insulated hose leads from the pump to a hole in the center of the top plate. A tube with an inside diameter of 0.64 cm is fitted into the hole. The pump injects fluid into the cell at a controllable constant flow rate. The video camera is mounted directly above the cell for some experiments. For others it is off to one side of the cell and aimed at an angle to the cell.

Below the aluminum bottom plate is another aluminum plate with channels machined into it. A MGW Lauda circulating bath circulates a water/antifreeze mixture through the channels to maintain the bottom plate at a cold temperature T_c . The entire cell was placed in a commercial household freezer to assist in cooling the bottom plate as well as to cool the top plate. The freezer temperature and the temperature of the water bath were maintained at approximately -20°C . Before entering the cell the glycerine is heated to a temperature T_h in the heating box shown in Fig. A.1. Within the box is a brass cylinder around which a copper tube is wound. A heated mixture of antifreeze and water circulates in the tube to heat the glycerine within the cylinder to T_h .

The hot glycerine initially enters an empty cell and spreads out radially. Once the glycerine reaches the edge of the cell it flows into a waste container. Food colouring is injected into the hot glycerine as it enters the cell at various times to aid in visualizing the flow. The dye is heated prior to injection by placing the dye-filled syringe in the heating box. During the initial filling stage the spreading air-glycerine interface should remain stable; fingering does not occur at the interface since a more-viscous fluid, glycerine, is displacing a less-viscous fluid, air [6].

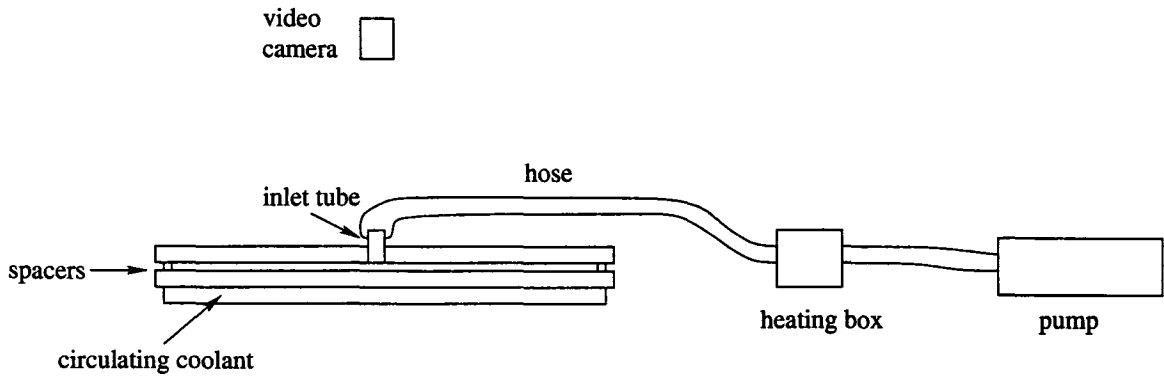


Figure A.1: A schematic illustration of the apparatus used to study thermoviscous fingering.

A.0.3 Results and discussion

Figure A.2 shows a sequence of images from a run of the experiment. The dye lines show at least one finger in the lower left hand corner that persists for the duration of the experiment. As Fig. A.2 (c) shows, eventually most of the injected glycerine flows through this finger with the glycerine in the remainder of the cell moving very little. Air bubbles are present in the glycerine for this run, for example, at the lower left hand corner of Fig. A.2 (c)), and may influence the beginning of such a finger.

Unfortunately repeating the run under the same conditions often did not result in a fingering instability. Other runs under slightly different conditions also show evidence of fingering, but in general we were unable to obtain results of sufficient quality to allow us to perform any quantitative measurements.

Figures A.3-A.5 show images from runs which also show some evidence of a fingering instability. A sequence of images from a run performed under the same conditions as that of Fig. A.2 is shown in Figure A.3. Fig. A.3 (a) shows a finger developing at what should be a stable interface. This suggests that perhaps solidification is occurring at the front, resulting in the majority of the interface moving more slowly as it solidifies. The dye lines in Figure A.3 (b) and (c) indicate three fingers present in

the flow. These three fingers suggest thermoviscous fingering and are different from the fingers seen at the interface in Fig. A.3 (a), although one finger is roughly at the same position. Figure A.4 is an image from a run for which fingering on a smaller magnitude is observed. The dye line on the right hand side of the image (delineated by the rectangle) is gently rippled, perhaps indicating thermoviscous fingering. Figure A.5 shows two fingers at the 3 and 6 o'clock positions. The edge of the glycerine at the 6 o'clock position is, however, closer to the edge of the cell than the glycerine elsewhere in the cell, again suggesting that perhaps solidification is retarding the flow elsewhere in the cell. These experimental images suggest the presence of a fingering instability, but the effect is not large.

For the runs discussed in the previous paragraphs, the viscosity ratio is on the order of 2500 – 11000, well above the critical viscosity ratio [2, 3, 4] predicted for fingering. A slow flow rate is also necessary for fingering. This can be seen by considering the dimensionless parameter P measuring the ratio of the thermal diffusion time $t_k = d^2/\kappa$, where d is half the distance between the plates of the cell and κ is the thermal diffusivity, to the time it takes for heat to be advected in the direction of the flow:

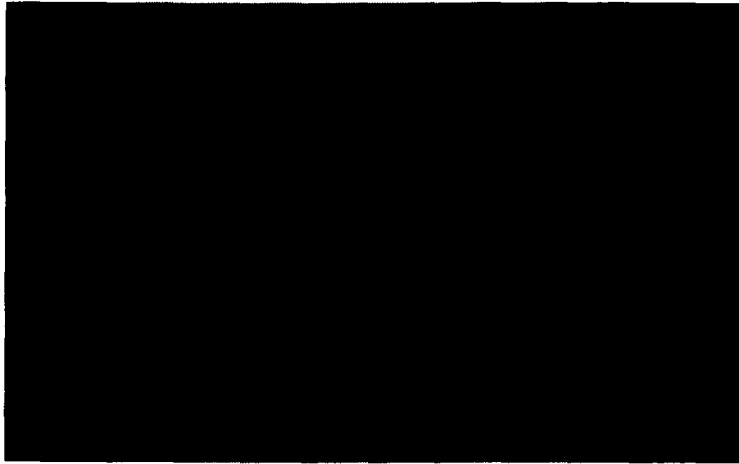
$$P = \frac{Ud^2}{R\kappa} \quad (\text{A.2})$$

where U is a typical velocity in the radial direction, and R is a typical length scale. significant heat loss to the walls of the cell is necessary for fingering, so P should be much less than 1 if fingering is to occur [6]. For the parameters of our system ($d = 0.25$ cm, $L \approx 20$ cm, and $\kappa \approx 9 \times 10^{-8}$ m²/s), this means that U must be much less than 0.3 cm/s for fingering to occur. Given a time of 20 minutes to initially fill the cell, U is on the order of 0.01 cm/s well below the speed calculated above. Often it takes even longer than 20 minutes to fill the cell, resulting in an even lower U , so

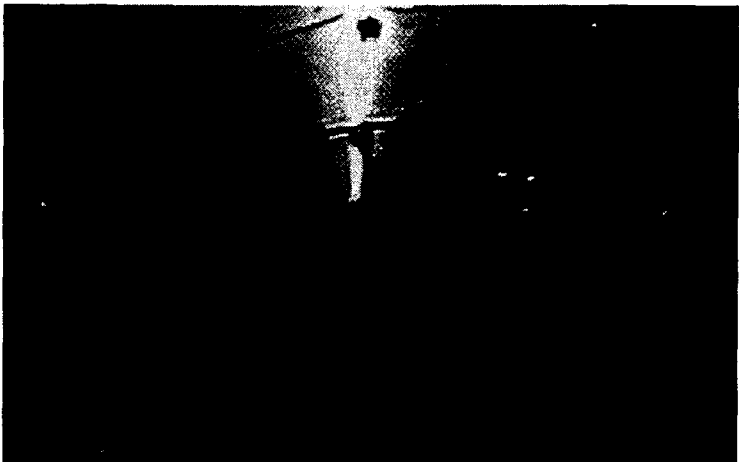
we should be in the regime where thermoviscous fingering is possible.

A possible explanation for the lack of definitive evidence for thermoviscous fingering in our experiments is that our inlet condition was one of constant flow rate as opposed to constant pressure [6]. A prerequisite for fingering according to the theory of Wylie et al. [4] is that the solution to the governing equations give multiple flow rates, a condition which is possible using an inlet condition of constant pressure. The experiments performed by Wylie et al. [1] were done using a constant gravitational pressure head to drive the flow, although experiments done with an inlet condition of constant flow rate also showed fingering but over a smaller range of parameters [6]. Helfrich [3] showed that while fingering is possible for both inlet conditions, fingering occurred for a wider range of parameters for the constant pressure inlet condition. It was also shown that the condition of fixed flow rate lead to both large and small wavenumber cutoffs of the instability while for constant pressure only a short wavenumber cutoff was present. As well, Helfrich [3] showed that higher growth rates occur when constant pressure is the inlet condition. In our experiments, we used a constant flow rate inlet condition, although, in retrospect, we may have been able to produce more conclusive results using a constant pressure inlet condition.

(a)



(b)



(c)



Figure A.2: A sequence of images from a run with $b = 0.5$ cm, T_c set at -20°C , and $T_h = 90^\circ\text{C}$. A finger is seen in the lower left hand corner and by (c) most of the glycerine is flowing through this finger.

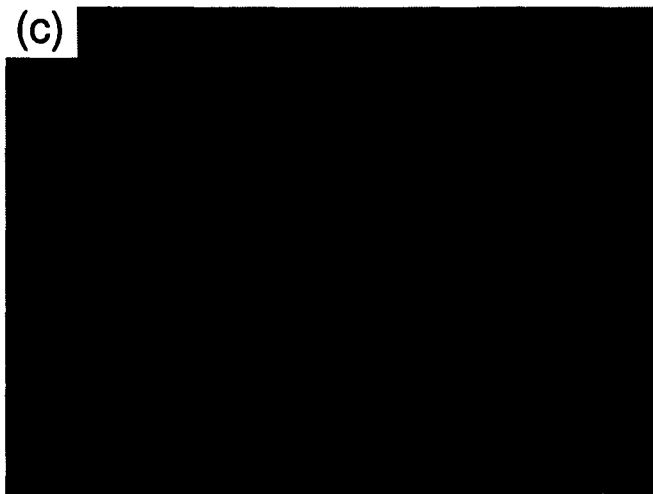
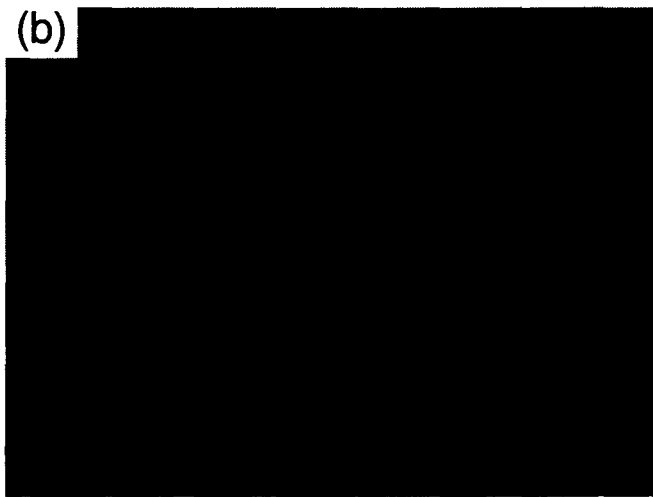
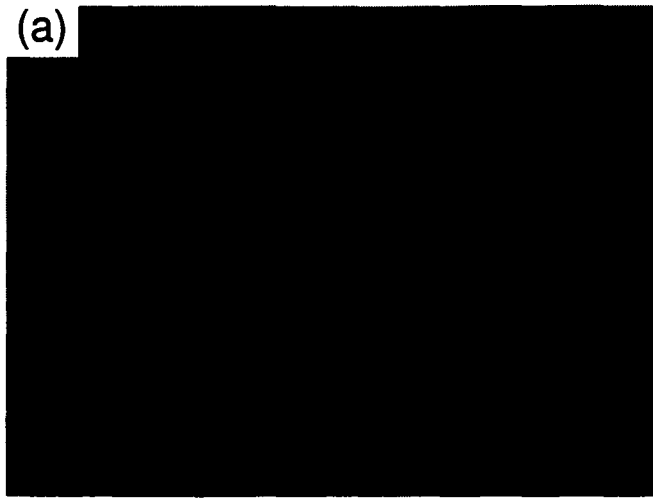


Figure A.3: A sequence of images from a run with the same conditions as the run in Fig. A.2. In (a) a finger is seen to develop at the glycerine-air interface. In (b) and (c) dye lines show three fingers.



Figure A.4: Dye lines show small ripple-like protrusions. The black rectangle is used to define the position of the ripples. Here $b = 0.5$ cm, $T_c = -30^\circ\text{C}$ and $T_h = 90^\circ$.

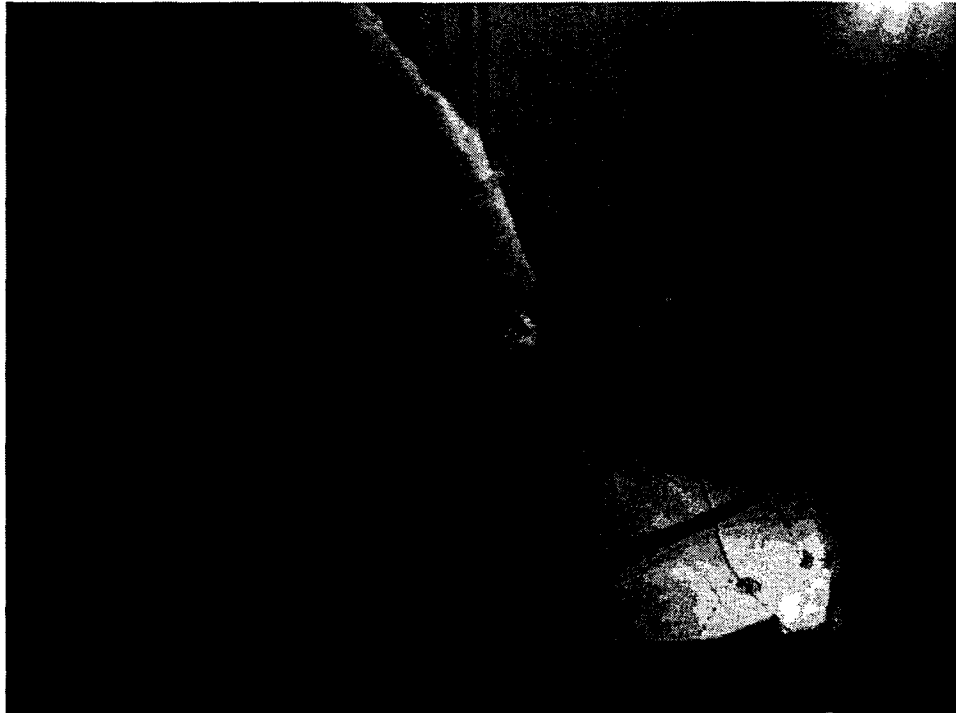


Figure A.5: Dye lines show two fingers; one on the right hand side and the other on the lower left hand side. Here $b = 0.5$ cm, T_c is set at -20°C and $T_h = 90^\circ\text{C}$.

Bibliography

- [1] J. J. Wylie, K. R. Helfrich, B. Dade, J. R. Lister, and J. F. Salzig, *Bull. Volcanol.* **60**, 432 (1999).
- [2] S. J. S. Morris, *J. Fluid Mech.* **308**, 111 (1996).
- [3] K. R. Helfrich, *J. Fluid Mech.* **305**, 219 (1995).
- [4] J. J. Wylie and J. R. Lister, *J. Fluid Mech.* **305**, 239 (1995).
- [5] J. A. Whitehead and K. R. Helfrich, *J. Geophys. Res.* **96B**, 4145 (1991).
- [6] J. J. Wylie, private communication.

Appendix B

Fluent Equations

Fluent [1] is a commercial software which in general solves the equations for conservation of mass and momentum (Eqs. (B.1) and (B.2) respectively) in the following forms (see the Fluent User's Guide [1] for details):

$$\frac{\partial \rho}{\partial t} + \nabla \cdot (\rho \vec{v}) = S_m \quad (\text{B.1})$$

$$\frac{\partial}{\partial t}(\rho \vec{v}) + \nabla \cdot (\rho \vec{v} \vec{v}) = -\nabla p + \nabla \cdot (\bar{\tau}) + \rho \vec{g} + \vec{F}. \quad (\text{B.2})$$

Here ρ is the density, \vec{v} is the velocity, S_m is a source term, p is the pressure, \vec{g} is the acceleration due to gravity and \vec{F} represents external body forces. $\bar{\tau}$ is the stress tensor and is given by

$$\bar{\tau} = \mu[(\nabla \vec{v} + \nabla \vec{v}^T) - \frac{2}{3} \nabla \cdot \vec{v} I] \quad (\text{B.3})$$

where I is the unit matrix.

The equation for conservation of energy is solved in the following form:

$$\frac{\partial}{\partial t}(\rho E) + \nabla \cdot (\vec{v}(\rho E + p)) = \nabla \cdot (\kappa_{eff} \nabla T - \sum_j h_j \vec{J}_j + (\bar{\tau}_{eff} \cdot \vec{v})) + S_h \quad (\text{B.4})$$

where E is the energy, κ_{eff} is the effective conductivity, T is the temperature, h is the enthalpy, \vec{J}_j is the diffusion flux of species j , and S_h is a source term.

These general equations simplify considerably for our case. There are no source terms and the fluid is incompressible so Eq. (B.1) becomes

$$\nabla \cdot \vec{v} = 0 \quad (\text{B.5})$$

In our system there are no external body forces, so the last term in Eq. (B.2) is absent. $\nabla \cdot \vec{v} = 0$, so Eq. (B.2) simplifies to the Navier-Stokes equation,

$$\rho \frac{\partial}{\partial t}(\vec{v}) + (\vec{v} \cdot \nabla) \vec{v} = -\nabla p + \rho \vec{g} + \mu \nabla^2 \vec{v}. \quad (\text{B.6})$$

Eq. (B.4) also simplifies considerably. The terms $\nabla \cdot \sum_j h_j \vec{J}_j$ and $\nabla \cdot (\tau_{eff} \cdot v)$ are heat transport due to species diffusion and viscous dissipation respectively. Our model includes neither of these. The equation reduces to

$$\frac{\partial}{\partial t}(\rho E) + \nabla \cdot (v(\rho E + p)) = \nabla \cdot \kappa_{eff} \nabla T. \quad (\text{B.7})$$

Bibliography

- [1] Fluent Inc. FLUENT Version 6.1.22 [computer program]. Fluent Inc., Lebanon, N.H. 2004.

